Phase transitions in two-dimensional itinerant electron systems

by

Matthew James Trott

University of
St Andrews

This thesis is submitted in partial fulfilment for the degree of
Doctor of Philosophy (PhD)
at the University of St Andrews

August 2020

Declaration

Candidate's declaration

I, Matthew James Trott, do hereby certify that this thesis, submitted for the degree of PhD, which is approximately 22,000 words in length, has been written by me, and that it is the record of work carried out by me, or principally by myself in collaboration with others as acknowledged, and that it has not been submitted in any previous application for any degree.

I was admitted as a research student at the University of St Andrews in August 2016.

I received funding from an organisation or institution and have acknowledged the funder(s) in the full text of my thesis.

Date: 28/09/2020 Signature of candidate:

Supervisor's declaration

I hereby certify that the candidate has fulfilled the conditions of the Resolution and Regulations appropriate for the degree of PhD in the University of St Andrews and that the candidate is qualified to submit this thesis in application for that degree.

Date: 28/09/2020 Signature of supervisor:

Permission for publication

In submitting this thesis to the University of St Andrews we understand that we are giving permission for it to be made available for use in accordance with the regulations of the University Library for the time being in force, subject to any copyright vested in the work not being affected thereby. We also understand, unless exempt by an award of an embargo as requested below, that the title and the abstract will be published, and that a copy of the work may be made and supplied to any bona fide library or research worker, that this thesis will be electronically accessible for personal or research use and that the library has the right to migrate this thesis into new electronic forms as required to ensure continued access to the thesis.

I, Matthew James Trott, confirm that my thesis does not contain any third-party material that requires copyright clearance.

The following is an agreed request by candidate and supervisor regarding the publication of this thesis:

Printed copy

No embargo on print copy.

Electronic copy

No embargo on electronic copy.

Date: 28/09/2020 Signature of candidate:

Date: 28/09/2020 Signature of supervisor:

Underpinning Research Data or Digital Outputs

Candidate's declaration

I, Matthew James Trott, hereby certify that no requirements to deposit original research data or digital outputs apply to this thesis and that, where appropriate, secondary data used have been referenced in the full text of my thesis.

Date: 28/09/2020 Signature of candidate:

Abstract

Phase transitions in two-dimensional itinerant electron systems

Matthew James Trott

The aim of this thesis it to contribute to three open problems in the theory of itinerant electron systems in two spatial dimensions. Firstly, the mechanism for charge density wave formation in the transition metal dichalcogenides is a debated subject. In this thesis it is shown that charge density wave formation is possible via a purely electronic mechanism in monolayer vanadium diselenide. The competition of superconductivity and density wave formation is taken into account using the renormalisation group. As the Fermi surface is tuned to perfect nesting, a charge density wave phase emerges when the Heisenberg exchange interaction is of the order of the contact Coulomb repulsion. Secondly, the search for materials which exhibit topological superconductivity is ongoing. Possible candidates are strongly spin-orbit-coupled metals. In this thesis a square-lattice Hubbard model with strong Rashba spin-orbit coupling and one of the Fermi surfaces close to a Lifshitz transition is examined. The metal is shown to be generically unstable to the formation of mixed-parity superconductivity with a helical triplet component via a renormalisation group analysis. Thirdly, the breakdown of Fermi liquid theory close to a quantum critical point is still not well understood. In this thesis a functional renormalisation group analysis is presented using a soft frequency cutoff, investigating a general class of Pomeranchuk instabilities with N_b flavours of boson. At small N_b the theory is characterised by weakly non-Fermi-liquid behaviour of the electrons and $z \approx 2$ dynamics for the order parameter fluctuations. For large N_b, the theory crosses over to $z \approx 1$ scaling and non-Fermi-liquid behaviour.

Acknowledgements

I would like to thank my supervisor Chris Hooley for his help and guidance through the PhD process. I would also like to thank my friends for the good memories and their willingness to listen to me moan about trivial nonsense. Finally I would like to thank my parents for there constant support and encouragement, without which I would not be the person I am today. The work in this thesis was supported by the Engineering and Physical Sciences Research Council (UK) Centre for Doctoral Training in Condensed Matter Physics [grant number EP/L015110/1].

Contents

List of Figures

Chapter 1

Outline of thesis

In the prolegomena I shall discuss the notion of emergence and the formation of quasi-particles and collective excitations in condensed matter systems. I will then discuss the breakdown of this picture. I will further discuss materials relevant to the results chapters of the thesis.

In chapter 3, "Fermi liquid instabilities and the renormalisation group" I shall first discuss instabilities of the Fermi liquid: conventional and unconventional superconductivity, density wave formation, and Pomeranchuk instabilities. I shall then discuss various renormalisation techniques that allow for an unbiased approach to the study of ordering in a non-relativistic fermionic system, and to examine order parameter fluctuations and their interaction with gapless fermionic excitations close to a quantum phase transition.

In chapter 4, "Charge density wave formation in the transition metal dichalcogenides" I will investigate the formation of charge density waves and superconductivity in the monolayer transition metal dichalcogenide vanadium diselenide. I shall show that density waves can form purely by an electronic mechanism when the Fermi surface is sufficiently nested and components of the bare interaction are attractive.

In chapter 5, "Mixed-parity superconductivity near Lifshitz transitions in strongly spin-orbit-coupled metals" I will investigate the formation of unconventional superconductivity in a square lattice Hubbard model with strong Rashba spin orbit coupling. I

shall examine the system close to a van Hove singularity where the susceptibilities of the system are enhanced. I shall show that superconductivity with mixed parity is formed.

In chapter 6, "Non-Fermi liquid fixed points and anomalous Landau damping in a quantum critical metal" I will investigate the feedback of order-parameter fluctuations on the Fermi liquid in quantum phase transitions. I utilise a modern functional renormalisation group method with a soft frequency cutoff to better capture the role of particle-hole fluctuations, suppressed in previous Wilsonian schemes. I shall show that a non-Fermi liquid fixed point with Landau-damped order parameter is formed with characteristics dependent on N_b, the number of bosonic flavours of the order parameter, and $N = k_F/k_{\mathrm{UV}}$, the non-universal ratio between the Fermi momentum k_F and the high energy limit of the Fermi liquid approximation k_{UV}.

The original work in this thesis is contained in chapters 4, 5, and 6. The publications related to these chapters are [Trott2020b, Trott2020a, Trott2018]:

- *Can Fermi surface nesting alone drive the charge-density-wave transition in monolayer vanadium diselenide?*, Matthew J. Trott and Chris A. Hooley, arXiv:2004.06665. [Trott2020b]

- *Mixed-parity superconductivity near Lifshitz transitions in strongly spin-orbit-coupled metals*, Matthew J. Trott and Chris A. Hooley, Phys. Rev. Research **2**, 013106 (2020). [Trott2020a]

- *Non-Fermi-liquid fixed points and anomalous Landau damping in a quantum critical metal*, Matthew J. Trott and Chris A. Hooley, Phys. Rev. B **98**, 201113(R) (2018). [Trott2018]

Chapter 2

Prolegomena

"The ability to reduce everything to simple fundamental laws does not imply the ability to start from those laws and reconstruct the universe."
Philip W. Anderson (1923 - 2020), Science **177**, 393 (1972).

2.1 Introduction

How can we understand the world around us? It is widely accepted that all life and everything on a length scale beneath and above, from the quark to the red giant, is governed by an underlying set of fundamental laws. We have a functional understanding of these natural laws in all but a handful of extreme, although admittedly crucial, scenarios. However difficulties arise when we wish to reconstruct the world we experience from these laws. The reason lies in the fascinating role of complexity and emergence; unimaginably large numbers of particles interacting in a multitude of ways to provide a plethora of phenomena of which we cannot practically predict from elementary laws with current theoretical methods and computational capacity, and of which we are constantly learning. Phases appear via the binding or repulsion of particles, or seemingly from nowhere without prior warning. Condensed matter physics lies so close to the fundamental underpinnings of nature but on the precipice of complexity where we can no longer consider only the set of laws gained from elementary particle physics to govern

all that we see [Anderson1972].

The length scale of condensed matter physics is already an intermediate length scale. The atoms in the molecules and crystal lattices are formed of protons and neutrons bound in atomic nuclei, orbited by electrons. The protons and neutrons themselves composite particles formed as bound states of quarks and described by elementary nuclear and particle physics. Venturing away from the microscopic scale of the crystal lattice, approaching intermediate mesoscopic and macroscopic length scales, the formation of composite objects governs the physics. Such composite objects are quasiparticles and collective excitations, corresponding to fermionic and bosonic emergent phenomena respectively. These composite objects are formed via cooperative and/or competitive phenomena of an uncountable number of particles. With number of electrons on the order of $10^{18} - 10^{24}$ and the nuclei of similar order, all interacting non-locally via Coulomb's law, the degrees of freedom, in addition dependent on the spatial dimension, become inordinately large. It quickly becomes impossible to keep track of all particles in the system.

However, conveniently for us, nature does not require us to retain all this information to predict the physics of longer length scales. Phenomenological models can be written down for the macroscopic physics with the aid of experimental data but can also be derived from the underlying microscopic model. There exists an "averaging" procedure which allows us to "coarse grain" the system and remove degrees of freedom, examining the system at different length scales. The physics of the system evolves between these length scales and this evolution can be understood via the renormalisation group [Wilson1974]. The renormalisation group is a computational tool that allows us to perform the coarse graining procedure mathematically and at least qualitatively, sometimes quantitatively. It thus allows us to predict changes in the macroscopic physics from changes at the microscopic scale without retaining all the initial information. The renormalisation group is intrinsic to our quantum field theoretic understanding of nature and is fundamentally linked with the idea of critical phenomena and broken symmetry.

2.2 Quasiparticles

The quintessential example of quasiparticles in condensed matter physics are the excitations above the ground state in Landau's Fermi liquid theory [Landau1957].

In a non-interacting Fermi gas consisting of fermionic particles such as electrons, the state of each electron can be described by the quantum numbers $(\mathbf{k}, s)$ with $\mathbf{k}$ the wavevector and s the $\hat{\mathbf{z}}$ projection of the spin. Setting $\hbar = 1$, $\mathbf{k}$ is also the momentum. Due to the Pauli exclusion principle no two fermions can occupy the same state. Therefore each momentum state $\mathbf{k}$ can only be occupied by an up spin and a down spin electron. When a large number of electrons occupy a system the momentum states quickly become filled and there exists a Fermi surface manifold in momentum space at zero temperature below which all states are occupied by electrons and above which the states are empty. The geometry of the Fermi surface, i.e. the momentum dependent structure, is dependent on the underlying crystal lattice and symmetries of the material considered. For a free electron system in two spatial dimensions the electron dispersion is $\varepsilon^0_{\mathbf{k}} = \mathbf{k}^2/2m_e$. The Fermi surface is circular at finite density, with radius k_F, and the chemical potential is $\mu = \varepsilon_F = k_F^2/2m$ with ε_F the Fermi energy and k_F the Fermi momentum.

Landau observed that by gradually switching on interactions in the Fermi gas, so that the non-interacting system adiabatically evolved into the interacting one, the system could be described by the same parameters as the Fermi gas modified only quantitatively for the interacting system [Landau1957]. In the interacting systems the electron is replaced with a virtual quasiparticle formed via cooperative phenomena between electrons that itself behaves as an electron would, with the same spin and charge but with modified properties to the Fermi gas. The mass of the electron is modified to an effective mass $m_e \to m^*$ and there is an additional term due to the presence of interactions

$$\varepsilon_{\mathbf{k}} = \varepsilon^0_{\mathbf{k}}\big|_{m_e \to m^*} + \sum_{\mathbf{k}'} f(\mathbf{k}, \mathbf{k}')\delta n_{\mathbf{k}}. \tag{2.1}$$

The Landau function $f(\mathbf{k}, \mathbf{k}')$ can be expanded in spherical harmonics to obtain the

infinite number of Landau parameters that describe the Fermi liquid theory in terms of the relative angle between momenta $\mathbf{k}$ and $\mathbf{k}'$. $\delta n_{\mathbf{k}}$ is the change in the quasiparticle distribution function from its equilibrium value.

2.3 Criticality and collective excitations

The formation of order in materials occurs when the cooperative interactions of electrons or other fluctuations in the material form collective excitations that propagate through the materials as bosonic particles. For example, in the case of the the paramagnet-ferromagnet transition, magnetic fluctuations in the disordered paramagnetic phase propagate through the system as paramagnons. As the temperature is lowered, the fluctuations build up in the system to cause the ferromagnetic transition. In the ordered ferromagnetic phase, fluctuations of the spins around the ordered state propagate through the system as magnons. Both paramagnons and magnons are the quantum mechanical equivalent of spin waves but the paramagnons can only propagate for short distances as patches of aligned spins form locally in the disordered phase. The distance the paramagnons can propagate is increased closer to the phase transition until long range order is reached and the ferromagnetic phase is formed. The magnons in the ordered phase propagate over long distances.

Fluctuations in the system can cause the system to undergo first or second order phase transitions. The phase transition and formation of a collective excitation can be described by an order parameter φ that is zero in the disordered phase and takes a finite value in the ordered phase. φ could be a scalar quantity, such as the magnetisation in a Ising ferromagnet, a vector quantity like the vector magnetisation in the Heisenberg ferromagnet, or even a tensor object. The ordered phase has a lower symmetry and thus spontaneous symmetry breaking occurs at the transition. Although the free energy of the system F should be a complicated object in general, Landau observed that in the vicinity of a second order transition the free energy could be expanded in powers of the characteristic order parameter of the system as an analytic function with the expansion

obeying the symmetries of the underlying Hamiltonian [Landau1937]

$$F = F_0 + a\varphi^2 + b\varphi^4 + \cdots . \tag{2.2}$$

The symmetry $\varphi \to -\varphi$ has already been assumed for the underlying Hamiltonian, hence there are no odd powers of φ. The parameters a and b of the theory are dependent on the temperature and F_0 contains terms independent of φ. Assuming b is constant near the phase transition, a changes sign so that $a \approx a_0(T - T_c)$ with T_c the critical temperature of the phase transition. At the phase transition, the correlation length ξ diverges and the system becomes scale invariant. Observables of the system become power-law divergent and are described by critical exponents that classify the universality class of the phase transition. The correlation length of the system diverges with the power law $\xi \sim (T - T_c)^{-\nu}$, defining the critical exponent ν. The specific heat C diverges with the power law $C \sim (T - T_c)^{-\alpha}$, defining the critical exponent α. On the ordered side of the transition, the order parameter is finite and goes to zero at the transition, vanishing with the power $\varphi \sim |T - T_c|^{\beta}$ with the critical exponent β. The power law behaviour occurs due to scaling arguments that preserve the physics when the system becomes scale invariant at the phase transition. There are cases where the divergence is not a power law, for example the logarithmic divergence in the two-dimensional Ising model. However, in real systems, second order phase transitions in general exhibit power law divergences.

As the temperature in the system approaches absolute zero, the entropy also goes to zero and thermal fluctuations die away; no thermal phase transition can occur. However, quantum fluctuations remain in the system due to Heisenberg's uncertainty principle. The quantum fluctuations can be strong enough that they can destroy the ordered state, or conversely cause the system to order [Green2018]. The corresponding quantum phase transitions give rise to a whole new array of quantum phenomena and effects. The quantum phase transition introduces an additional critical exponent z, the dynamical exponent that describes the divergence of the characteristic time of the system $\tau_c \sim \xi^z$

at the phase transition and leads to an anisotropy between space and time if $z \neq 1$.

2.4 Breakdown of the quasiparticle picture

The presence of a quantum phase transition in the phase diagram of materials also exhibits effects that extend to finite temperature. Fermi liquid theory appears to break down close to the quantum critical point and a non-Fermi liquid state is formed that can no longer be described by Landau quasiparticles.

The non-Fermi-liquid states arises due to the interaction of the electronic excitations of the Fermi liquid with the bosonic fluctuations of the order parameter as it approaches long-range order. The electron-electron interactions are mediated by the bosonic modes in this regime causing corrections to the Fermi liquid behaviour. The effect of the bosonic modes can be such that the Fermi liquid breaks down and the quasiparticle excitations are no longer well defined objects.

The original approach to the problem involved integrating out fermionic modes from the mixed fermion-boson theory to obtain an effective order-parameter theory of the quantum critical metal [Hertz1976, Millis1993]. The bosonic propagator develops a Landau-damping term of the form proportional to $\Omega/|\mathbf{q}|$ which, due to the anisotropy in scaling with the $|\mathbf{q}|^2$ term in the propagator, gives the dynamical exponent $z = 3$. The Landau damping term leads to a decay of the order parameter into particle-hole excitations. However, the procedure of integrating out the Fermi liquid gapless modes close to the Fermi surface causes non-analytic and singular corrections to the order parameter propagator and interaction vertices [Belitz1997, Abanov2004, Thier2011].

2.5 Relevant materials to thesis

The materials relevant to this thesis can be divided into three classes: the transition metal dichalcogenides, relevant to chapter 4; Materials with antisymmetric spin-orbit coupling, relevant to chapter 5; and materials with quantum critical regimes, relevant to chapter 6.

2.5.1 Transition metal dichalcogenides

An extremely important two-dimensional material which preceded the transition metal dichalcogenides is graphene. Graphene was first isolated in 2004 [Novoselov2004]; this kick-started a huge wave of research into two-dimensional materials [Das2015]. Graphene has the interesting property of Dirac cones in the conduction band such that the electrons dynamics can be described by relativistic massless quasiparticles. Although graphene is extremely interesting due to its two-dimensional nature and Dirac cones, there has been limited success in utilising graphene for device applications so far due to difficulties in large scale manufacturing and the additional fine-tuning needed to obtain the precise material properties required. Therefore a wider search for two dimensional materials and van der Waals heterostructure techniques has been brought about by graphene research in order to obtain new material properties for device physics [Geim2013]. However, renewed interest in graphene has recently emerged due to superconductivity and Mott insulating behaviour found in twisted bilayer graphene [Cao2018].

The transition metal dichalcogenides MX_2 (M = Ti, V, Nb, Mo, Ta, W; X = S, Se, Te) allow for a much larger variation in properties due to the large class of elements available to design materials with, while still retaining the hexagonal lattice structure of graphene and can be engineered to be two dimensional [Manzeli2017]. The transition metal dichalcogenides display a wide range of behaviours, including Mott insulating, semi-metallic, charge density wave, excitonic, and superconducting phases. Beyond the wide variety of properties available, two or more different transition metal dichalogenides can be combined in van der Waals heterostructures to vary the material properties even more in the search for strongly correlated materials [Geim2013].

Many transition metal dichalcogenides have charge density wave transitions with high critical temperatures. The critical temperature also tends to be enhanced in the monolayer limit [Yang2014]. Charge density waves can form via an electronic mechanism when the Fermi surface is nested. When sections of the Fermi surface become parallel, the particle-hole susceptibility at a finite wavevector $\mathbf{Q}$ can be enhanced and a density wave forms [Johannes2008, Chen2016, Sykora2018, Halbinger2019]. However, charge den-

sity waves may also form in the transition metal dichalcogenides via the softening of phonon modes [Hajiyev2013], via the Rice-Scott saddle band mechanism [Rice1975], or via a mechanism with a transition to an exciton insulator [Rossnagel2011]. The electronic mechanism for charge density wave formation due to Fermi surface nesting is the mechanism of interest in chapter 4 of this thesis.

2.5.2 Topological superconductivity from spin-orbit coupling

Topological superconductivity is important in realising topological quantum computation via localized Majorana zero modes and is thus currently widely investigated in materials physics [Das Sarma2015]. Topological superconductivity is superconductivity with non-trivial topology that arises when the superconductivity has an unconventional form factor, with spin-triplet Cooper pairs carrying non-zero angular momentum [Sato2017]. This form of unconventional superconductivity is thought to arise from spin-fluctuation-mediated pairing instead of the conventional phonon-mediated pairing prevalent in most superconducting materials [Kohn1965]. Another possible route to topological superconductivity is via spin-orbit coupling in materials, which alters the symmetries of the system and causes a mixing of spin-singlet and spin-triplet superconducting states. The work performed in chapter 5 of this thesis combines both spin-orbit coupling due to breaking of inversion symmetry and the Kohn-Luttinger mechanism to investigate topological superconductivity in lattice systems.

There are different types of spin-orbit coupling in materials: symmetry independent coupling due to spin-orbit interaction in atomic orbits, and symmetry dependent coupling that arises in systems without inversion symmetry such as non-centrosymmetric crystal structures and at interfaces. The symmetry dependent type is of greater interest because it alters the properties of the material in way that may lead to topological superconductivity.

A class of materials of great interest in the search for materials that have the required topological characteristics are those with non-centrosymmetric or non-symmorphic crystal structures [Sigrist2009, Bauer2012]. The broken inversion symmetry of the non-

centrosymmetric materials allows for antisymmetric spin-orbit coupling [Smidman2017]. This leads to a mixing of spin-singlet and spin-triplet Cooper pairs [Gorkov2001]. The non-centrosymmetric material $CePt_3Si$ is a candidate for an $(s+p)$-wave superconducting state [Bauer2004, Samokhin2004]. It is also believed that Li_2Pt_3B exhibits spin-triplet superconductivity [Nishiyama2007].

Additionally, cuprate thin films grown on a substrate are possible spin-triplet candidates. The films have an induced Rashba spin-orbit interaction which leads to a $(d+p)$-wave pairing state [Yoshida2016, Takasan2017]. Unconventional superconductivity is also thought to arise at oxide interfaces [Scheurer2015].

2.5.3 Quantum critical points in metals

Quantum critical points occur in several classes of materials including: heavy fermion compounds [Gegenwart2008], the ruthenates [Rost2011], the cuprates [Sachdev2010], and the iron-based superconductors [Shibauchi2013].

The cuprates are primarily known as high temperature superconductors with superconductivity with a critical temperature of $35K$ first discovered in in 1986 [Bednorz1986]. The superconductivity is also of of an unconventional d-wave form not mediated by phonons [Scalapino1995, Tsuei2000]. The cuprates exhibit a spin density wave quantum critical point, above which a "fan" non-Fermi liquid behaviour occurs where the temperature dependence of the thermodynamic observables is altered from the expected Fermi liquid form [Sachdev2010]. The quantum critical point is shrouded in a dome of the high temperature superconductivity. The cuprates also exhibit other interesting phenomena such as pseudogap regime in the phase diagram [Valla2006, Armitage2010].

The iron pnictides also have a similar phase diagram to the cuprates, with high temperature superconductivity first observed in 2008 [Kamihara2008], and a non-Fermi liquid regime above a spin density wave quantum critical point [Shibauchi2013]. However, the Fermi surface structure is multi-band and far more complicated that in the case of the cuprates which have a single band Fermi surface. The pnictides also have a nematic region in the phase diagram with the Fermi surface undergoing a Pomeranchuk

instability [Fernandes2014]. Another similar compound, the iron chalcogenide FeSe, is of even greater interest due to its simplified chemical structure and Fermi surface. FeSe also exhibits non-Fermi liquid physics; however, the quantum critical point is purely nematic, with no magnetic fluctuations in the material [Kuo2016, Hosoi2016].

Chapter 3

Fermi liquid instabilities and the renormalisation group

"Nobody ever promised you a rose garden."

Joseph Polchinski (1954 - 2018), arXiv:hep-th/9210046.

3.1 Fermi liquid instabilities

Fermi liquid theory has been inordinately successful in describing the behaviour of metallic systems. The Fermi liquid regime in most metals extends over large regions of the phase diagram at low to intermediate temperatures. However, the Fermi liquid fixed point is unstable to several particle-particle and particle-hole processes [Anderson2002].

The interacting Hamiltonian of fermionic quasiparticles with spin $s \in \{\uparrow, \downarrow\}$ and dispersion $\xi_{\mathbf{k}}$ is given by

$$H = \sum_{\mathbf{k},s} \xi_{\mathbf{k}} c^\dagger_{\mathbf{k}s} c_{\mathbf{k}s} + \frac{1}{N} \sum_{ss'} \sum_{\mathbf{k}_1\mathbf{k}_2\mathbf{k}_3\mathbf{k}_4} V(\mathbf{k}_1, \mathbf{k}_2, \mathbf{k}_3, \mathbf{k}_4) \delta_{\mathbf{k}_1+\mathbf{k}_2-\mathbf{k}_3-\mathbf{k}_4+\mathbf{G}} c^\dagger_{\mathbf{k}_4 s} c^\dagger_{\mathbf{k}_3 s'} c_{\mathbf{k}_2 s'} c_{\mathbf{k}_1 s}. \tag{3.1}$$

The delta function imposes momentum conservation between ingoing and outgoing particles. Due to the presence of the lattice, the momentum is conserved modulo a reciprocal lattice vector $\mathbf{G} = l\mathbf{b}_1 + m\mathbf{b}_2 + n\mathbf{b}_3$, $l, m, n \in \mathbb{Z}$. The interaction term represents two-

particle scattering processes and is spin and frequency independent for the following discussion. The interaction term can be rewritten

$$V_{\text{int}} = \frac{1}{N}\sum_{ss'}\sum_{\mathbf{k}\mathbf{k}'\mathbf{q}'} V(\mathbf{k},\mathbf{k}',\mathbf{q}')c^{\dagger}_{\mathbf{q}'s}c^{\dagger}_{\mathbf{k}+\mathbf{k}'-\mathbf{q}'s'}c_{\mathbf{k}'s'}c_{\mathbf{k}s}. \tag{3.2}$$

The interaction vertex is depicted in Fig. 3.1. The bare interaction term allows for several instabilities via effective interactions that develop due to the scattering processes that occur. To investigate these instabilities it is a good first approximation to calculate the corrections to the bare interaction due to scattering processes at one-loop in perturbation theory. The corrections are given by the three contributions:

$$\tau_{\text{pp}} = \int_q V(\mathbf{k},\mathbf{k}',\mathbf{q})G(q)G(k+k'-q)V(\mathbf{q},\mathbf{k}+\mathbf{k}'-\mathbf{q},\mathbf{q}'), \tag{3.3}$$

$$\tau^{\text{cr}}_{\text{ph}} = \int_q V(\mathbf{k},\mathbf{q}+\mathbf{k}'-\mathbf{q}')G(q)G(q+k'-q')V(\mathbf{q},\mathbf{q}+\mathbf{k}'-\mathbf{q}',\mathbf{q}'), \tag{3.4}$$

$$\begin{aligned}\tau^{\text{d}}_{\text{ph}} = &\int_q -2V(\mathbf{k},\mathbf{q},\mathbf{q}')G(q)G(q+k-q')V(\mathbf{q}+\mathbf{k}-\mathbf{q}',\mathbf{k}',\mathbf{q})\\ &+\int_q V(\mathbf{k},\mathbf{q},\mathbf{q}+\mathbf{k}-\mathbf{q}')G(q)G(q+k-q')V(\mathbf{q}+\mathbf{k}-\mathbf{q}',\mathbf{k}',\mathbf{q})\\ &+\int_q V(\mathbf{k},\mathbf{q},\mathbf{q}')G(q)G(q+k-q')V(\mathbf{k}',\mathbf{q}+\mathbf{k}-\mathbf{q}',\mathbf{q}),\end{aligned} \tag{3.5}$$

where the abbreviations $k = (\omega_n, \mathbf{k})$ and $q = (\Omega_n, \mathbf{q})$ denotes Matsubara frequencies and momenta. The integral sign denotes

$$\int_q = T\sum_n \int \frac{d^d\mathbf{q}}{(2\pi)^d} \xrightarrow[T\to 0]{} \int \frac{d\Omega d^d\mathbf{q}}{(2\pi)^{d+1}}. \tag{3.6}$$

The contributions correspond to the particle-particle, crossed particle-hole and three direct particle-hole diagrams depicted in Fig. 3.1. The Green's functions are $G(k) = (i\omega_n - \xi_{\mathbf{k}})^{-1}$.

Investigating a specific case, the Hubbard interaction representing pure contact

Coulomb repulsion is given by

$$V_{\text{int}} = \frac{U}{N} \sum_{ss'} \sum_{\mathbf{k}\mathbf{k}'\mathbf{q}'} c^{\dagger}_{\mathbf{q}'s} c^{\dagger}_{\mathbf{k}+\mathbf{k}'-\mathbf{q}'s'} c_{\mathbf{k}'s'} c_{\mathbf{k}s}. \tag{3.7}$$

The three direct particle-hole diagrams cancel and only the particle-particle and crossed particle-hole diagrams remain. Integrating over the Matsubara frequencies the diagrams are $\tau_{\text{pp}} = U^2 \Pi_{\text{pp}}^{\mathbf{k}+\mathbf{k}'}(\omega)$ and $\tau_{\text{ph}}^{\text{cr}} = -U^2 \Pi_{\text{ph}}^{\mathbf{k}'-\mathbf{q}'}(\omega)$ with the particle-particle and particle-hole susceptibilities defined as

$$\Pi_{\text{pp}}^{\mathbf{Q}}(\omega) = \int_k G(k) G(-k+Q) = \int \frac{d^d\mathbf{k}}{(2\pi)^d} \frac{1 - n_{\text{F}}(\xi_{\mathbf{k}}) - n_{\text{F}}(\xi_{-\mathbf{k}+\mathbf{Q}})}{-i\omega + \xi_{\mathbf{q}} + \xi_{-\mathbf{q}+\mathbf{Q}}}, \tag{3.8}$$

$$\Pi_{\text{ph}}^{\mathbf{Q}}(\omega) = -\int_k G(k) G(k+Q) = -\int \frac{d^d\mathbf{k}}{(2\pi)^d} \frac{n_{\text{F}}(\xi_{\mathbf{k}}) - n_{\text{F}}(\xi_{\mathbf{k}+\mathbf{Q}})}{i\omega + \xi_{\mathbf{k}} - \xi_{\mathbf{k}+\mathbf{Q}}}, \tag{3.9}$$

with $n_{\text{F}}(\varepsilon) = (e^{\varepsilon/k_{\text{B}}T} + 1)^{-1}$ the Fermi-Dirac distribution. The additional minus sign is included in the definition of $\Pi_{\text{ph}}^{\mathbf{Q}}(\omega)$ so that all the susceptibilities stated in Chapters 4 and 5 diverge the same way to positive infinity. Due to this definition care must be taken when considering the sign of diagrammatic contributions from $\tau_{\text{ph}}^{\text{cr}}$ and $\tau_{\text{ph}}^{\text{d}}$. Evaluating the integrals at zero temperature, the Fermi-Dirac distribution becomes a step function.

The particle-particle susceptibility develops a logarithmic divergence when $\xi_{-\mathbf{q}+\mathbf{Q}} = \xi_{\mathbf{q}}$ which occurs most often when $\mathbf{Q} = 0$. The particle-hole susceptibility develops a logarithmic divergence when $\xi_{-\mathbf{q}+\mathbf{Q}} = -\xi_{\mathbf{q}}$, satisfied when the Fermi surface is nested. The logarithmic divergence of the particle-hole channel is specific to two spatial dimensions. The divergence of the susceptibility is reduced as the spatial dimensionality is increased due to the reduced area of nested regions in higher dimensions.

Evaluating the integrals at zero temperature, the integrals are approximately

$$\Pi_{\text{ph}}^{\mathbf{Q}}(\omega) \approx \Pi_{\text{pp}}^{\mathbf{0}}(\omega) \approx \nu_0 \log\left(\frac{W}{\omega}\right) \tag{3.10}$$

so that $\tau_{\text{pp}} \approx -\tau_{\text{ph}}^{\text{cr}}$. The external frequency ω acts as an infrared cutoff and the bandwidth W is an ultraviolet cutoff. ν_0 is the density of states at the Fermi surface.

Due to the nature of the perturbative expansion, numerous sets of diagrams with different topology contribute to the renormalisation of the effective interaction, with diagrams with new topologies arising at each new loop-order in the expansion. Therefore, approximations must be made in order to obtain a solution. A simple first approximation to consider is the ladder approximation, where only the topology of diagram found at one-loop is included and the sets of diagrams are resummed in separate channels. The effective interactions in the zero momentum particle-particle and momentum $\mathbf{Q}$ particle-hole channels are

$$U_{\mathrm{pp}}^{\mathrm{Ladder}} = \frac{U}{1 + U\nu_0 \log\left(\frac{W}{\omega}\right)}, \qquad U_{\mathrm{ph}}^{\mathrm{Ladder}} = \frac{U}{1 - U\nu_0 \log\left(\frac{W}{\omega}\right)}. \tag{3.11}$$

The interactions diverge when $1 \pm U\nu_0 \log\left(\frac{W}{\omega}\right) = 0$. This divergence can be interpreted as the emergence of a new degree of freedom such as Cooper pair formation in the case of superconductivity and signals the possibility of spontaneous symmetry breaking and order. In the ladder approximation an instability can only occur in the particle-particle channel if the bare interaction U is attractive. In the particle-hole channel the logarithmic divergence occurs for repulsive bare interaction U but requires the nesting condition stated above, $\xi_{-\mathbf{q}+\mathbf{Q}} = -\xi_{\mathbf{q}}$, to be satisfied and is thus Fermi surface dependent.

3.1.1 Superconductivity

The formation of superconductivity occurs when a component of the effective interaction becomes attractive so that bound states of electrons can form. Given that the superconducting instability forms at $\mathbf{Q} = \mathbf{k} + \mathbf{k}' = \mathbf{0}$ the Cooper pairs form between incoming particles with opposite momenta $\mathbf{k}' = -\mathbf{k}$. The superconducting order parameter is given by

$$\Delta_{ss'}(\mathbf{k}') = \sum_{\mathbf{k}} V^{\mathrm{eff}}_{\mathbf{k},\mathbf{k}'} \langle c^{\dagger}_{\mathbf{k}s} c^{\dagger}_{-\mathbf{k}s'} \rangle. \tag{3.12}$$

The properties of the measurable superconducting gap function, the square modulus of the order parameter, are dependent on the symmetries of the material and the pairing mechanism that overcomes the Coulomb repulsion between electrons encoded

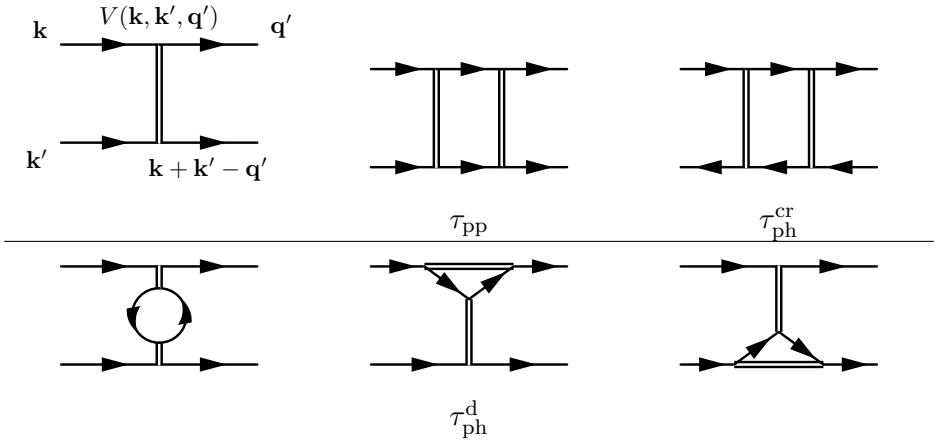

Figure 3.1: Top left: Two-particle interaction vertex with momentum conservation labelled and definition of $V(\mathbf{k},\mathbf{k}',\mathbf{q}')$ momentum indices. Others: Particle-particle τ_{pp}, crossed particle-hole $\tau_{\mathrm{ph}}^{\mathrm{cr}}$, and three direct particle-hole diagrams $\tau_{\mathrm{ph}}^{\mathrm{d}}$ that contribute at one-loop as corrections to the two-particle vertex.

in the effective interaction $V_{\mathbf{k},\mathbf{k}'}^{\mathrm{eff}}$. In the conventional theory of superconductivity, Bardeen–Cooper–Schrieffer (BCS) theory [Bardeen1957], lattice phonons mediate the attractive interaction between electrons. This leads to an isotropic "s-wave" and spin singlet pairing instability. However, superconductivity also occurs in strongly correlated systems where the electron-phonon coupling is too weak to overcome the Coulomb repulsion. This occurs due to a coupling between the particle-hole and particle-particle channels in the Kohn-Luttinger mechanism [Kohn1965]. Divergent contributions from the particle-hole channel to the particle-particle channel drive the pairing instability, typically in a different angular momentum channel to the s-wave case due to different momentum and spin structure of the effective interaction [Sigrist1991]. Additionally, unconventional pairing can occur at $\mathbf{Q} \neq 0$ as Fulde–Ferrell–Larkin–Ovchinnikov (FFLO) superconductivity [Fulde1964, Larkin1965].

3.1.2 Density waves

Particle-hole instabilities can take the form of either a charge $\rho_{\mathbf{Q}}$ or spin $\mathbf{m}_{\mathbf{Q}}$ instability. The spin and charge order parameters are

$$\rho_{\mathbf{Q}} = \langle n_{\mathbf{Q}} \rangle = \sum_{s} \sum_{\mathbf{k}} \langle c^{\dagger}_{\mathbf{k}s} c_{\mathbf{k}+\mathbf{Q}s} \rangle, \qquad \mathbf{m}_{\mathbf{Q}} = \langle \mathbf{S}_{\mathbf{Q}} \rangle = \frac{1}{2} \sum_{ss'} \langle \sum_{\mathbf{k}} c^{\dagger}_{\mathbf{k}s} \boldsymbol{\sigma}_{ss'} c_{\mathbf{k}+\mathbf{Q}s'} \rangle \tag{3.13}$$

with the charge order parameter the expectation value of the number operator $n_{\mathbf{Q}}$ and the spin order parameter the expectation value of the spin operator $\mathbf{S}_{\mathbf{Q}}$. $\boldsymbol{\sigma} = (\sigma_x, \sigma_y, \sigma_z)^{\mathrm{T}}$ denotes the vector of Pauli matrices. The two-particle interaction (3.2) can be decomposed into these spin and charge channels due to the $SU(2)$ nature of the interaction and the completeness relation $\boldsymbol{\sigma}_{\alpha\beta} \cdot \boldsymbol{\sigma}_{\gamma\delta} = 2\delta_{\alpha\delta}\delta_{\beta\gamma} - \delta_{\alpha\beta}\delta_{\gamma\delta}$. The instability occurs when the transfer momentum $\mathbf{Q}$ fulfils the nesting condition and causes a divergence in the effective charge or spin interaction. Due to the finite value of $\mathbf{Q}$ the order forms as a periodic structure in real space $\rho_i \sim e^{i\mathbf{Q}\cdot\mathbf{r}_i}$ or $\mathbf{m}_i \sim e^{i\mathbf{Q}\cdot\mathbf{r}_i}$ corresponding to a spin or charge density wave [Gruner1994].

3.1.3 Pomeranchuk instabilities

The Fermi liquid is also unstable to Fermi surface deformations, or Pomeranchuk instabilities [**?**]. The Fermi liquid two-particle interaction can be expanded into separate angular momentum channels; instabilities in these channels can drive a deformation in the Fermi surface and can lead to breakdown in Fermi liquid theory [Metzner2003, DellAnna2006]. The angular momentum channel $l = 0$ corresponds to a ferromagnetic instability. The $l = 2$ case corresponds to the electron nematic [Fradkin2010]. Considering the nematic instability, the two-particle interaction can be rewritten in the d-wave charge channel as [Metzner2003]

$$V_{\mathrm{int}} = \frac{1}{N} \sum_{ss'} \sum_{\mathbf{k}\mathbf{k}'\mathbf{q}'} U(\mathbf{q}') d_{\mathbf{k}} d_{\mathbf{k}'} c^{\dagger}_{\mathbf{k}+\mathbf{q}'/2,s} c^{\dagger}_{\mathbf{k}'-\mathbf{q}'/2,s'} c_{\mathbf{k}'+\mathbf{q}'/2,s'} c_{\mathbf{k}-\mathbf{q}'/2,s} \tag{3.14}$$

where the momenta have been relabelled and the interaction term decomposed in a separable form. The "d-wave" form factor is $d_{\mathbf{k}} = \cos k_x - \cos k_y$. The resultant nematic order parameter is [Maslov2010]

$$\rho_{\mathbf{Q}} = \sum_s \sum_k d_{\mathbf{k}} \langle c^\dagger_{\mathbf{k}+\mathbf{Q}/2,s} c_{\mathbf{k}-\mathbf{Q}/2,s} \rangle. \tag{3.15}$$

The momentum dependence of $d_{\mathbf{k}}$ leads to deformation the Fermi surface so that it is anisotropic in momentum space.

3.1.4 Topological Fermi surface transitions and van Hove singularities.

Additionally, there exist Fermi surface transitions that cause a breakdown in Fermi liquid theory. In lattice systems there exist saddle points in the non-interacting band structure where the gradient of the dispersion vanishes

$$\nabla_{\mathbf{k}} \xi_{\mathbf{k}} = \mathbf{0}. \tag{3.16}$$

Raising or lowering the chemical potential via electron or hole doping of the material through the saddle point, a Lifshitz transition occurs. At a Lifshitz transition the Fermi surface transitions between an open and closed Fermi surface, or two or more Fermi surface pockets connect [Lifshitz1960, Volovik2017]. Further, the density of states is enhanced and becomes divergent, a van Hove singularity. If two Fermi surface regions connect at the van Hove singularity, the density of states becomes logarithmically divergent at the saddle point location on the Fermi surface. If the van Hove singularity is formed by the connection of three or more Fermi surface pockets it becomes a higher order van Hove singularity and power law divergences can occur [Shtyk2017, Efremov2019, Yuan2019, Isobe2019].

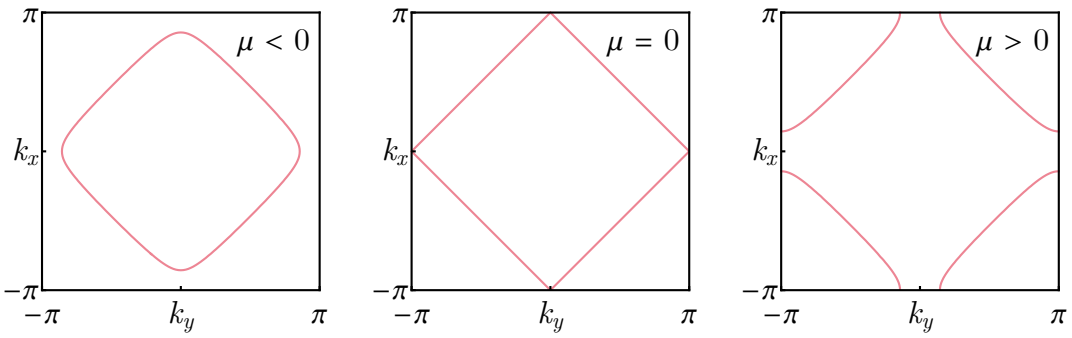

Figure 3.2: Schematic of Lifshitz transition in the nearest-neighbour square lattice Hubbard model. The chemical potential of the van Hove singularity $\mu_{\text{vHS}} = 0$. The saddle points lie at $(\pm\pi, 0)$ and $(0, \pm\pi)$ at the edge of the Brillouin zone. The system transitions from a closed Fermi surface at $\mu < \mu_{\text{vHS}}$ through a van Hove singularity to and open Fermi surface at $\mu > \mu_{\text{vHS}}$

3.1.5 Landau-Ginsburg-Wilson theory

In the vicinity of a phase transition, additional methodologies beyond conventional Fermi liquid theory are required to classify the transition and take into account fluctuations of the order parameter. The corresponding Landau-Ginzburg-Wilson theory to describe systems close to a phase transition is given by the action [Wilson1974]

$$S_{\text{LGW}} = \int d^{d+1}x \left[\frac{1}{2} \partial_\mu \varphi \partial^\mu \varphi + \tilde{\delta}\varphi^2 + \tilde{\lambda}\varphi^4. \right] \tag{3.17}$$

The field φ is the order parameter for the theory. The parameters of the theory are dependent on external factors of the system under consideration. The action and parameters can be derived from the quantum field theory defined microscopically via performing a Hubbard-Stratonovich transformation and integrating out the fermions or phenomenologically from symmetry as is done in Landau theory. The action S_{LGW} is thus a more formal development of Landau's theory of phase transitions (2.2) allowing for the full consideration of the underlying quantum field theory. Due to universality, the general form of the action remains the same and only the exact values of the parameters change between different models and materials.

The fluctuations of the order parameter are important when considering the phase transition. Order parameter fluctuations tend to reduce the ordering probability of the system and can even remove the possibility of order completely [Mermin1966]. To obtain the full set of universal critical exponents of the system a renormalisation group analysis is required to go beyond a simple minimisation of the order parameter action, which does not capture the fluctuations.

For a quantum critical metal the effective order-parameter theory can be describe on the simplest level by Hertz-Millis theory [Hertz1976, Millis1993]. The scaling of the order parameter is altered, characterised by the dynamical exponent z, altering the critical dimension of the field theory. However, the bosonic modes couple to gapless modes on the Fermi surface causing non-analytic and singular corrections to the propagator of the effective order parameter [Belitz1997, Abanov2004, Thier2011]. Therefore it is necessary to retain both the fermionic and order parameter degrees of freedom to describe the quantum critical metal. The order parameter is again Landau-damped and the fermion self energy is modified by the bosonic fluctuations to a non-Fermi liquid form.

The analysis performed in chapter 6 investigates the role of Fermi liquid-order parameter interactions in the breakdown of a Fermi liquid close to a quantum critical point.

3.2 The renormalisation group

The renormalisation group allows us to examine changes to the physical system we are interested in at different energy scales. The renormalisation group originated in the study of quantum field theories to address infinities in quantum electrodynamics [Stueckelberg1953, Gell-Mann1954]. Improvements in renormalisation group methodologies culminated in the more general, and conceptually most profound, approach of Kenneth Wilson [Wilson1974].

Wilson's original implementation of the renormalisation group was to separate the high- and low-momentum Fourier modes of a field, and then integrate over the high

momentum modes to remove them from the theory. An effective theory for the interactions within the system at decreasing energy / longer wavelength is obtained as the high energy fluctuations are integrated out of the theory. The partition function for a Euclidean scalar field is given by

$$Z = \int \mathcal{D}\varphi \, e^{-S[\varphi, \tilde{\mathbf{g}}]}. \tag{3.18}$$

Here $S[\varphi, \mathbf{g}]$ denotes the bare action for the field φ at some characteristic high energy scale W. The entries in the vector $\tilde{\mathbf{g}}$ are coupling constants for the interactions within the system. The ultraviolet bandwidth cutoff W has been imposed so that only frequencies and momenta below this scale appear within the original theory and no ultraviolet divergences occur.

The field φ can be divided into high- and low-momentum modes, comprising of the ultraviolet ($\varphi_>$) and infrared ($\varphi_<$) components of the field. $\varphi = \varphi_> + \varphi_<$ is split into its constituent Fourier components, $\varphi_<$ contains momentum modes $|q| \leq \Lambda_{\mathrm{UV}}$ and $\varphi_>$ contains the momentum modes $\Lambda_{\mathrm{UV}} < |q| \leq W$ with $\Lambda_{\mathrm{UV}} < W$ the new energy scale of interest. The partition function is

$$Z = \int \mathcal{D}\varphi_> \mathcal{D}\varphi_< \, e^{-S[\varphi_< + \varphi_>, \tilde{\mathbf{g}}]}. \tag{3.19}$$

By performing an integration over the ultraviolet modes of the theory the Wilsonian effective action

$$e^{-S[\varphi_<, \tilde{\mathbf{g}}(\Lambda_{\mathrm{UV}}), \Lambda_{\mathrm{UV}}]} = \int \mathcal{D}\varphi_> \, e^{-S[\varphi_> + \varphi_<, \tilde{\mathbf{g}}]} \tag{3.20}$$

is obtained. The new partition function reads

$$Z = \int \mathcal{D}\varphi_< \, e^{-S[\varphi_<, \tilde{\mathbf{g}}(\Lambda_{\mathrm{UV}}), \Lambda_{\mathrm{UV}}]}. \tag{3.21}$$

The couplings $\tilde{\mathbf{g}}$ defined at W evolve to a set with new parameters $\tilde{\mathbf{g}}(\Lambda_{\mathrm{UV}})$ at energy scale Λ_{UV}. This procedure is performed iteratively to obtain the values of coupling constants at different energy scales. The parameter Λ_{UV} is thus a renormalisation group

flow parameter for which the couplings of the system evolve as the parameter is lowered.

The effective action can be expanded in terms of all local operators that obey the symmetries of the action

$$S[\varphi_<, \tilde{\mathbf{g}}(\Lambda_{\mathrm{UV}}), \Lambda_{\mathrm{UV}}] = \int d^{d+1}x \sum_i \tilde{g}^i \mathcal{O}_i[\varphi_<]. \tag{3.22}$$

The action is dimensionless and thus if the operators $\mathcal{O}_i$ has scaling dimensions in terms of energy $[\mathcal{O}_i] = D_i$ then the couplings $\tilde{g}_i$ have the scaling dimensions $[\tilde{g}^i] = d + 1 - D_i$ with d the spatial dimension of the system. Defining the dimensionless couplings $g_i = \Lambda_{\mathrm{UV}}^{D_i - d - 1} \tilde{g}_i$ the couplings g_i should be of order one as Λ_{UV} is the characteristic energy scale of the system [Polchinski1992]. If a process occurs at an infrared energy scale Λ then the operator is of the order $\int d^{d+1}x \mathcal{O}_i \sim \Lambda^{D_i - d - 1}$ and the term in the action is of order $g_i(\Lambda/\Lambda_{\mathrm{UV}})^{D_i - d - 1}$. If $D_i > d+1$ then the term will become smaller at low energies as $\Lambda \to 0$ and is therefore irrelevant. If $D_i < d + 1$ then the term will become large at low energies and is therefore relevant. If $D_i = d + 1$ then the term is marginal and does not change as the energy is lowered.

3.2.1 Shankar renormalisation group

The fermionic formulation of the Wilsonian renormalisation group differs in nature from the bosonic one. Due to the presence of the Fermi surface, low-energy electrons lie close to a d-dimensional manifold in momentum space instead of close to zero momentum in the case of the boson. Therefore, the scaling procedure for finite density Fermi systems requires rescaling towards the Fermi surface manifold. This introduces additional complications into the theory and gives rise to an entirely new set of physics [Shankar1991, Polchinski1992, Shankar1994].

The Hamiltonian (3.1) with the dispersion

$$\xi_{\mathbf{k}} = \frac{\mathbf{k}^2}{2m} - \mu = \frac{\mathbf{k}^2 - k_F^2}{2m} \tag{3.23}$$

describes a Fermi liquid with a circular Fermi surface. The dispersion can be linearised

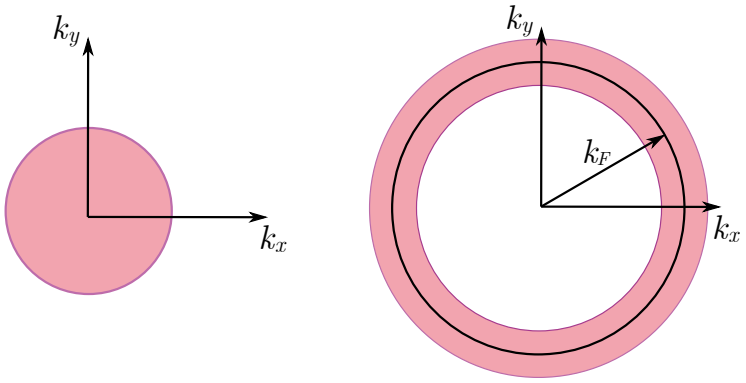

Figure 3.3: Momentum space picture of high and low energy degrees of freedom for bosonic (left) and fermionic (right) particles. Pink region denotes low energy states with the white region outside the high energy states.

close to the Fermi surface. The linearised dispersion is $\xi_{\mathbf{k}} \approx v_F \ell$ with v_F the Fermi velocity, set to one for the rest of the thesis, and $\ell = |\mathbf{k}| - k_F$. The linearisation procedure is valid below an absolute momentum $|\ell| \leq k_{\mathrm{UV}}$ dependent on non-universal properties of the material considered [Kopietz1997]. The Fermi surface can then be parametrised by the momentum ℓ, which scales under the renormalisation group, and the angle θ around the Fermi surface, which does not scale.

The interaction term in the Hamiltonian can be expanded in general powers of momenta,

$$V(\mathbf{k}_1, \mathbf{k}_2, \mathbf{k}_3, \mathbf{k}_4) = U + V_1 \ell + V_2 \ell^2 + \dots \tag{3.24}$$

Due to the scaling dimension of the fermionic fields all momentum-dependent terms are irrelevant and the momentum-independent term is marginal. However, the momentum-independent term is still dependent on the angles of the incoming and outgoing particles around the Fermi surface

$$U = U(\theta_1, \theta_2, \theta_3, \theta_4). \tag{3.25}$$

The angular dependence can be simplified by considering the possible momenta of incoming and outgoing particles in the two-particle interaction.

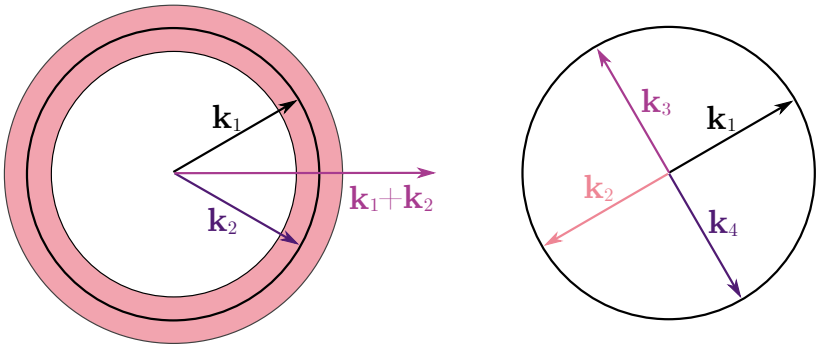

Figure 3.4: Left: Outgoing momenta must remain in the low energy annulus around the Fermi surface so outgoing momenta are restricted to be equal to the the incoming momenta up to a permutation in the infrared [Shankar1994]. Right: In the superconducting channel the incoming and outgoing total momentum is zero and therefore the outgoing particles can take any angle as long as they are opposite each other.

It turns out there are two possible cases: In the first case, outgoing momenta are restricted to remain in the low energy annulus around the Fermi surface and therefore $\mathbf{k}_3$ and $\mathbf{k}_4$ must be equal to the incoming momenta $\mathbf{k}_1$ and $\mathbf{k}_2$ or $\mathbf{k}_2$ and $\mathbf{k}_1$ respectively in the infrared. The two-particle interaction can then parametrised by the difference between the two angles $U = U(\theta_1, \theta_2)$. This result reproduces Landau's theory of the Fermi liquid where the system is described by a function $f(\mathbf{k}_1, \mathbf{k}_2) = U(\theta_1, \theta_2)$ and the Fermi liquid is described by an infinite number of couplings or Landau parameters dependent on the angle between the momenta $\mathbf{k}_1$ and $\mathbf{k}_2$ [Landau1957].

In the particle-particle channel the incoming total momentum is zero and $\theta_2 = -\theta_1$. Therefore $\mathbf{k}_3$ and $\mathbf{k}_4$ can take any angle around the Fermi surface as long as $\theta_4 = -\theta_3$. The coupling is then parametrised by the difference between the two angles $U = U(\theta_1, \theta_3)$. This result is in addition to Landau's original theory. When performing a one-loop renormalisation group study this coupling causes an instability to superconductivity when one of the initial couplings $U(\theta_1, \theta_3)$ is even infinitesimally attractive [Shankar1991, Polchinski1992, Shankar1994].

The significance of Shankar's renormalisation group analysis is the emergence of the

Fermi liquid as a fixed point of the renormalisation group flow. All interactions in the theory are irrelevant, except for a low-temperature instability to superconductivity [Polchinski1992, Shankar1994].

3.2.2 Parquet renormalisation group

Shankar's renormalisation group allows us to understand how the Fermi liquid arises in an interacting electron system. However, in real materials the Fermi surface is a more complicated structure and the phase diagrams much richer, with additional phases not restricted to just superconductivity. Therefore, additional methodologies are required to investigate systems with multiple instabilities.

The analysis presented in section 3.1, considering resummed ladder diagrams in order to predict divergences in the effective interaction of a certain channel, is one method to investigate the onset of order in an interacting electronic system. However, the analysis is incomplete. The first indication is that the Kohn-Luttinger mechanism, required for unconventional superconductivity, is completely absent. The mutual feedback between particle-particle, crossed particle-hole, and direct particle-hole channels should be included in order to investigate the competition, cooperation and coexistence of ordering phenomena. A possible technique to investigate this mutual feedback is the parquet renormalisation group, employed in chapters 4 and 5 of this thesis.

The parquet renormalisation group is a perturbative weak-coupling approach to study the development of fluctuations in a system as the energy is lowered, beginning away from criticality [Maiti2013]. The parquet renormalisation group allows fluctuations to develops in both the particle-particle and particle-hole channels and allows for the treatment of orders and their competition on an equal footing.

For a Fermi system with nesting, divergences of susceptibilities develop in both the particle-particle and particle-hole channels. The particle-particle channel diverges logarithmically $\Pi^{\mathbf{0}}_{\mathrm{pp}} \sim \log(W/\omega)$, thus it is convenient to define the alternate renormalisation group flow parameter $y = \log(W/\omega)$, proportional to the divergence of the particle-particle susceptibility, to track the build up of fluctuations when lowering the energy of

the system. In the particle-hole channel the divergence of the susceptibility is suppressed away from perfect nesting, with the logarithmic divergence cut by a nesting parameter ϵ that goes to zero at perfect nesting, $\Pi_{\mathrm{ph}}^{\mathbf{Q}} \sim \log\left(W/\sqrt{\omega^2+\epsilon^2}\right)$ [Maiti2013]. If the particle-hole channel is too far from the nesting condition, fluctuations will only develop in the particle-particle channel. However, even away from perfect nesting, particle-hole fluctuations can still drive order. The crossover between behaviours can be examined by tuning the nesting of the Fermi surface, as is performed in chapter 4.

In the case of a system doped to a van Hove singularity, the particle-particle susceptibility exhibits a higher order divergence $\Pi_{\mathrm{pp}}^{\mathbf{0}} \sim \log^2(W/\omega)$. Thus, a more convenient renormalisation group flow parameter is $y = \log^2(W/\omega)$ with the particle-hole divergence also becoming log squared at perfect nesting.

For both flow parameters, W is the ultraviolet cutoff on the order of the bandwidth and ω the flowing infrared energy scale. The onset of order occurs when a set of interaction couplings diverge at a scale y_c. y_c is finite as an artefact of the one-loop calculations but $y_c \to \infty$ when all fluctuations are included.

The caveat of parquet approach is that it does not take into account the fermion self-energy corrections at one-loop order and so cannot predict a departure from Fermi liquid theory. Additionally it does not take into account the fluctuations of the order parameter as the phase transition is approached.

3.2.3 Functional renormalisation group

The functional renormalisation group is a modern reformulation of Wilson's idea of renormalisation [Polchinski1984, Wetterich1993, Metzner2012, Delamotte2012]. The formulation utilises a universal and exact flow equation for the effective action and thus is not restricted by perturbation theory. A caveat is that the renormalisation group flow can become uncontrolled as there is no longer a small parameter in terms of which to expand the theory. The functional renormalisation group can be used to study universal and non-universal critical behaviour in the vicinity of continuous classical or quantum phase transitions. Additionally, the functional renormalisation group can be applied in

any dimension and has been shown to give reasonably accurate results even at low-order truncations.

The functional renormalisation group of Wetterich [Wetterich1993] is formulated in terms of a scale dependent effective action, which is the generating functional of one-particle-irreducible (1PI) correlation functions. To obtain all information about the system the Schwinger functional $W[J]$, the logarithm of the partition function $Z[J]$, can be utilised

$$W[J] = \log Z_\Lambda[J] = \log \int \mathcal{D}\varphi e^{-S[\varphi]+\int J\varphi}. \tag{3.26}$$

$J\varphi$ is a source term which allow for the generation of all correlation functions of the system

$$\langle \varphi(q_1)\varphi(q_2)\dots\varphi(q_n)\rangle = \frac{\delta^n}{\delta J(q_1)\delta J(q_2)\dots\delta J(q_n)} W[J]\Big|_{J\to 0}, \tag{3.27}$$

where $\frac{\delta}{\delta J}$ is a functional derivative. However, the Schwinger functional contains reducible correlation functions, additional information about the system not required as only one-particle-irreducible diagrams contribute to the renormalisation group equations. The effective action can be obtained via a Legendre transform of the Schwinger functional

$$\Gamma[\phi] = \sup_J \left(\int J\phi - W[J] \right). \tag{3.28}$$

The full quantum effective action $\Gamma[\phi]$ contains all information about the system as the functional integral still must be performed to obtain it. However, performing the functional integral is impossible in all but a few cases. To obtain information about the long wavelength physics contained within the effective action, a scale dependence is introduced $\Gamma \to \Gamma_\Lambda$ so that the effective average action $\Gamma_\Lambda[\phi]$ can interpolate from the bare action in the ultraviolet $\Gamma_{\Lambda\to\Lambda_{\mathrm{UV}}} = S$ to the full quantum effective action in the infrared $\Gamma_{\Lambda\to 0} = \Gamma$.

The scale dependence is introduced via a regulator function R_Λ dependent on the renormalisation group scale Λ, modifying the bare action $S[\varphi] \to S_\Lambda[\varphi] = S[\varphi] + \Delta S_\Lambda[\varphi]$

and Schwinger functional $W[J] \to W_\Lambda[J] = \log \int \mathcal{D}\varphi e^{-S[\varphi]-\Delta S_\Lambda[\varphi]+\int J\varphi}$, with

$$\Delta S_\Lambda[\phi] = \frac{1}{2}\int_q \varphi_q R_\Lambda(q^2)\varphi_{-q}. \tag{3.29}$$

The scale dependent effective average action is found via a modified Legendre transform of the Schwinger functional

$$\Gamma_\Lambda[\phi] = \sup_J \left(\int J\phi - W_\Lambda[J] \right) - \Delta S_\Lambda[\phi]. \tag{3.30}$$

The flow parameter Λ in the effective average action formalism is an infrared cutoff of the theory and not an ultraviolet cutoff Λ_{UV} as in the original Wilsonian formulation above. As the infrared cutoff is lowered, degrees of freedom are integrated in to the effective action until all fluctuations have been taken into account and the quantum effective action is reached. The additive function $R_\Lambda(q^2)$ must obey $R_\Lambda(q^2) > 0$ for $q^2/\Lambda^2 \to 0$, ensuring that no infrared divergences occur as $q^2 \to 0$. It also requires $R_\Lambda(q^2) \to 0$ for $q^2/\Lambda^2 \to \infty$ so that for $q^2 > \Lambda^2$ the regulator function vanishes and the high momentum modes are also cut off. The function must also diverge to infinity for $\Lambda \to \Lambda_{\mathrm{UV}}$ with Λ_{UV} a ultraviolet cutoff of the theory. An example regulator function is plotted in Fig. 3.5.

Taking a derivative with respect to the scale $\partial_\Lambda = \frac{d}{d\Lambda}$ of the effective average action yields the functional renormalisation equation [Wetterich1993, Metzner2012]

$$\partial_\Lambda \Gamma_\Lambda = \frac{1}{2}\,\mathrm{STr}\left[\Gamma_\Lambda^{(2)} + R_\Lambda\right]^{-1} \partial_\Lambda R_\Lambda. \tag{3.31}$$

The supertrace is defined $\mathrm{STr}\, A = \mathrm{Tr}\, A_b - \mathrm{Tr}\, A_f$ with A_b and A_f the bosonic and fermionic sectors of the matrix A. The trace integrates over momenta and frequencies and sums over all internal variables. $\Gamma_\Lambda^{(2)}$ denotes the second functional derivative of the effective action with respect to the fields and forms a Hessian matrix. The Hessian is defined

$$\Gamma_\Lambda^{(2)} = \frac{\overrightarrow{\delta}}{\delta\bar{\phi}}\Gamma_\Lambda\frac{\overleftarrow{\delta}}{\delta\phi} \tag{3.32}$$

The field ϕ can in general be a vector superfield formed of both bosonic and fermionic

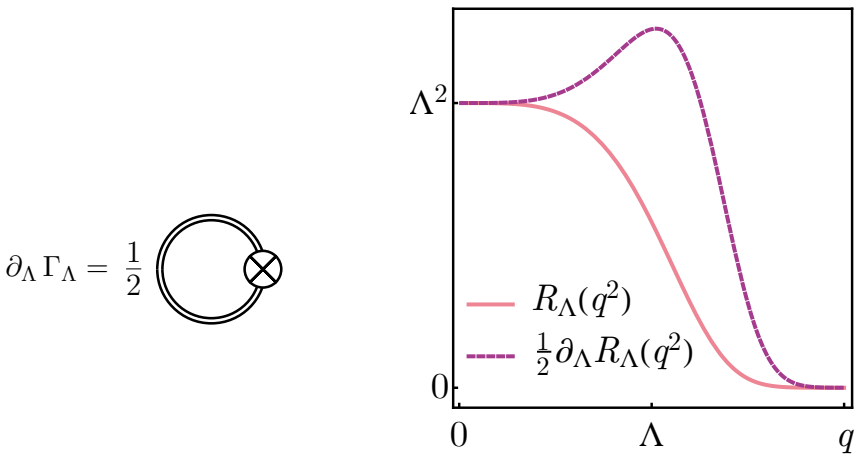

Figure 3.5: Diagrammatic representation of the functional renormalisation group (3.31). The equation is exact due to the presence of the full system propagator $\left[\Gamma^{(2)}_\Lambda + R_\Lambda\right]^{-1}$ represented by the double solid line. The regulator derivative $\partial_\Lambda R_\Lambda$ is represented by a crossed circle. Right: Example exponential regulator function $R_\Lambda(q^2) = \frac{q^2(q^2/\Lambda^2)}{e^{(q^2/\Lambda^2)^n}-1}$ and its scale derivative with $n = 2$ [Pawlowski2017]. The regulator function suppresses slow modes because $R_\Lambda(q^2) \geq \Lambda^2$ for $|q| < \Lambda$ regulating the infrared degrees of freedom. The scale derivative of the regulator $\partial_\Lambda R_\Lambda$ controls the integration over momentum/energy shells.

fields and thus the supertrace is required as additional minus signs arise in the fermionic sector due to the one-loop structure of the flow equation. The one-loop structure can be seen in the diagrammatic depiction of the functional renormalisation group equation, shown in Fig. 3.5. The equation is exact due to the presence of the full system propagator $\left[\Gamma^{(2)}_\Lambda + R_\Lambda\right]^{-1}$ with the additional insertion of the regulator derivative $\partial_\Lambda R_\Lambda$. However, due to the exact nature of the flow equation, the propagator still retains all information about the one-particle-irreducible vertices. Thus, suitable truncations of the effective average action are required in order to solve the flow equation (3.31).

The renormalisation group flow will be independent of R_Λ if the flow equation is solved exactly. However, when the effective action is truncated in order to find a solution, a scheme dependence on the regulator function R_Λ is introduced which must be taken into account. Optimised cutoffs have been found for Lorentz invariant systems [Litim2000, Litim2001].

In the non-relativistic case the problem is more complicated. Often there is an anisotropy in scaling between space and time dimensions and between individual spacial dimensions in effective field theories. This is evident in the Schrodinger equation and in Hertz-Millis theory. For non-relativistic finite density theories, soft modes are vital to the understanding of the underlying physics as gapless excitations dominate at low energies. Non-relativistic momentum type cutoffs have been found to suppress the fermionic soft modes and thus remove vital effects that are essential to the low-energy physics [Husemann2009]. In addition, the Fermi surface must be kept fixed in order to facilitate the scaling procedure towards the Fermi surface. Further complications also arise when there exist additional bosonic degrees of freedom which scale differently under the renormalisation group. In order to deal with these issues the "Ω scheme" frequency cutoff was introduced [Salmhofer2007]. The proposed frequency cutoff is advantageous as: space-time anisotropy does not affect the scaling as only the frequency component is regularised, soft frequency modes are not artificially suppressed, and the Fermi surface can dynamically adjust during the flow as no constraints are enforced upon the shape under scaling.

In order to facilitate calculation of the flow equation (3.31) it is useful to define the regulator derivative

$$\partial_\Lambda^{\mathrm{R}} = \sum_i \partial_\Lambda R_i \frac{\delta_i}{\delta R_i}. \tag{3.33}$$

The flow equation can then be rewritten

$$\partial_\Lambda \Gamma_\Lambda = \frac{1}{2} \operatorname{STr} \partial_\Lambda^{\mathrm{R}} \ln \left[\Gamma_\Lambda^{(2)} + \mathbf{R}_\Lambda \right]. \tag{3.34}$$

This allows for the flow equation to be expanded using the identity $\ln(1+x) = \sum_n (-1)^n x^n / n$

$$\partial_\Lambda \Gamma_\Lambda = \frac{1}{2} \partial_\Lambda^{\mathrm{R}} \operatorname{STr} \ln(\Gamma_{\Lambda,0}^{(2)} + \mathbf{R}_\Lambda) + \frac{1}{2} \partial_\Lambda^{\mathrm{R}} \operatorname{STr} \sum_{n=1}^{\infty} \frac{(-1)^{n+1}}{n} \left(\frac{\Delta \Gamma_\Lambda^{(2)}}{\Gamma_{\Lambda,0}^{(2)} + \mathbf{R}_\Lambda} \right)^n. \tag{3.35}$$

The Hessian matrix has been divided into two parts: $\Gamma^{(2)}_{\Lambda,0}$ denoting field independent propagator terms, and $\Delta\Gamma^{(2)}_{\Lambda}$ denoting the field dependent fluctuation terms. This form of the flow equation allows for the calculation of the truncated flow equations for all scale dependent components of the effective action via computer algebra methods [Gies2002].

3.2.4 Beta functions and the stability matrix.

Beta functions encode the scale dependence of the coupling constants and mass. The beta function is defined [Delamotte2012]

$$\Lambda\,\partial_\Lambda\,\mathbf{g} = \vec{\beta}(\mathbf{g}). \tag{3.36}$$

This equation gives the evolution of the coupling constant over energy scales. At a fixed point $\vec{\beta}(\mathbf{g}_*) = 0$. Small deviations of the couplings away from this fixed point are defined as $\delta\mathbf{g} = \mathbf{g} - \mathbf{g}_*$

$$\Lambda\,\partial_\Lambda\,\mathbf{g} - \Lambda\,\partial_\Lambda\,\mathbf{g}_* = \vec{\beta}(\mathbf{g}) - \vec{\beta}(\mathbf{g}_*) = \frac{d\vec{\beta}}{d\mathbf{g}}|_{\mathbf{g}_*} \cdot \delta\mathbf{g} + \mathcal{O}[\delta\mathbf{g}^2]. \tag{3.37}$$

The stability matrix is defined as

$$\mathcal{M}_{ij} = \left.\frac{d\beta_i}{dg_j}\right|_{\mathbf{g}=\mathbf{g}_*}. \tag{3.38}$$

Close to a fixed point the stability matrix obeys the equation

$$\Lambda\,\partial_\Lambda\,\delta\mathbf{g} = \mathcal{M}\delta\mathbf{g}. \tag{3.39}$$

Reformulated in terms of an eigenvalue equation, $\vec{v}_i$ represent the eigenvectors such that $\delta\mathbf{g} = \sum_i \vec{v}_i$ and θ_i the corresponding eigenvalues.

$$\mathcal{M}\vec{v}_i = -\theta_i\vec{v}_i \tag{3.40}$$

Around a fixed point the renormalisation group flow behaves as a power law along its eigenvectors. The behaviour is encoded in the eigenvalue θ_i. If $\theta_i > 0$ then the RG flow runs away from the fixed point along the eigenvector $\vec{v}_i$. This corresponds to a relevant direction. If $\theta_i < 0$ then the RG flow moves into the fixed point. This is called an irrelevant direction and an irrelevant coupling. If $\theta_i = 0$ then the coupling is marginal and higher order in the expansion of $\delta\mathbf{g}$ are required to ascertain the nature of the coupling.

Chapter 4

Charge density wave formation in the transition metal dichalcogenides

4.1 Introduction

To describe a possible mechanism for the charge density wave transition in the transition metal dichalcogenides (TMDs) I will formulate a model of the 1T structural isomer of vanadium diselenide, VSe_2, in the monolayer limit. Monolayer Vanadium diselenide is seen to have large nested sections of the Fermi surface. However, experimental studies of the material's low-temperature Fermi surface do not agree. Some studies predict column-like Fermi surface pockets protruding from the edge of the Brillouin zone [Zhang2017, Esters2017, Duvjir2018, Chen2018] while others show large triangular Fermi surface pockets around the K and K$'$ points of the Brillouin zone with a second small Fermi surface pocket at the Γ point of the zone [Umemoto2018, Feng2018]. The precise Fermi surface found is dependent on small variations of the chemical potential within the vicinity of a van Hove singularity in the band structure [Feng2018]. In similar hexagonal Brillouin zone problems doped to a van Hove singularity an enhancement in the superconducting

susceptibility is expected [Nandkishore2012, Chen2015].

The variation in the predicted Fermi surface leads to a disagreement over the predicted density wave **Q**-vector and therefore the reconstructed unit cell. A set of studies propose a **Q**-vector perpendicular to the Brillouin zone edge [Mcmillan1975, Umemoto2018, Sugawara2019], in the k_y direction. Another set of studies propose nesting vectors parallel to the Brillouin zone edges [Duvjir2018, Jang2019]. However both sets of studies agree on a renormalisation to flat Fermi surface sections in the low-temperature and low-dimensional limit.

The model of monolayer 1T-VSe_2 I will investigate consists of column-like Fermi surfaces extending from the edge of the Brillouin zone [Duvjir2018, Jang2019]. The patch scheme should also be applicable in the case of the triangular Fermi surface case after a modification to the intra- and inter-pocket scattering and the definitions of the superconducting symmetries. I perform a one-loop renormalisation group (RG) analysis of the problem using a Parquet approach that retains the particle-particle and particle-hole channels. This is required to capture the effect of Fermi surface nesting on the interplay and competition of superconductivity and density-wave fluctuations [Furukawa1998b, Whitsitt2014].

4.2 Model and methods

The low-energy model investigated is a single-band extended Hubbard model for monolayer vanadium diselenide. The single metallic band $\xi_{\mathbf{k}}$ utilised in the Hamiltonian is phenomenologically derived from experimental data for monolayer 1T-VSe_2 [Duvjir2018, Jang2019]. The non-interacting Fermi surface used in the model is shown in Fig. 4.1. The interacting momentum space Hamiltonian is

$$H = \sum_{s=\uparrow,\downarrow} \sum_{\mathbf{k}} (\xi_{\mathbf{k}} - \mu) c^{\dagger}_{\mathbf{k}s} c_{\mathbf{k}s} + \sum_{ss'} \sum_{\mathbf{k}_1,\mathbf{k}_2,\mathbf{k}_3,\mathbf{k}_4} V_0(\mathbf{k}_1,\mathbf{k}_2,\mathbf{k}_3) \delta_{\mathbf{k}_1+\mathbf{k}_2-\mathbf{k}_3-\mathbf{k}_4} \overline{\psi}_{\mathbf{k}_4 s} \overline{\psi}_{\mathbf{k}_3 s'} \psi_{\mathbf{k}_2 s'} \psi_{\mathbf{k}_1 s}. \tag{4.1}$$

The creation operator $c^{\dagger}_{\mathbf{k}s}$ creates an electron with momentum $\mathbf{k}$ and spin s. The bare interaction vertex in momentum space is

$$\begin{aligned} V_0(\mathbf{k}_1,\mathbf{k}_2,\mathbf{k}_3) =& U - \frac{J}{2}\left(\cos\left(k_x^{13}\right) + \cos\left(\frac{1}{2}k_x^{13} + \frac{\sqrt{3}}{2}k_y^{13}\right) + \cos\left(\frac{1}{2}k_x^{13} - \frac{\sqrt{3}}{2}k_y^{13}\right)\right) \\ &+ (V - \frac{J}{4})\left(\cos\left(k_x^{23}\right) + \cos\left(\frac{1}{2}k_x^{23} + \frac{\sqrt{3}}{2}k_y^{23}\right) + \cos\left(\frac{1}{2}k_x^{23} - \frac{\sqrt{3}}{2}k_y^{23}\right)\right) \end{aligned} \tag{4.2}$$

with $\mathbf{k}^{13} = \mathbf{k_1} - \mathbf{k}_3$ and $\mathbf{k}^{23} = \mathbf{k_2} - \mathbf{k}_3$ and $\mathbf{k}^{13} = (k_x^{23}, k_y^{23})$. The identity $\boldsymbol{\sigma}_{\alpha\beta} \cdot \boldsymbol{\sigma}_{\gamma\delta} = 2\delta_{\alpha\delta}\delta_{\beta\gamma} - \delta_{\alpha\beta}\delta_{\gamma\delta}$ has also been employed to expand the spin operators. U and V are the strengths of the effective contact and long-range Coulomb repulsion. J is an effective Heisenberg exchange coupling which denotes the strength of spin flips in the model. The long-range Coulomb repulsion and Heisenberg exchange interaction terms are assumed to be generated in the flow of the renormalisation group from the microscopic model to the current low-energy model utilised. The momentum dependence attached to the V and J is generated from nearest-neighbour hopping on the triangular lattice and obey the symmetries of the underlying microscopic model.

The phenomenological low-energy model is not directly derived from an underlying microscopic model. Therefore, the interactions U, V, and J are already intermediate couplings renormalised from the bare values. They cannot be directly linked to the contact Coulomb repulsion, long-range Coulomb repulsion, and Heisenberg exchange coupling measured in experiment or the bare values calculated at the microscopic level due to the phenomenological nature of the derivation of the Fermi surface and patch scheme. However, I utilise the parameters so that I can fine tune the initial conditions of the running interactions of the model. Subsets of the interactions can then begin as either repulsive or attractive interactions. The resultant phase diagram of the model in Fig 4.6 then qualitatively describes the physics in regions where subsets of the couplings change sign. The signs of the initial conditions for the couplings are defined in Fig. 4.5.

Considering the additional effect of phonons on the interactions, the Coulomb repul-

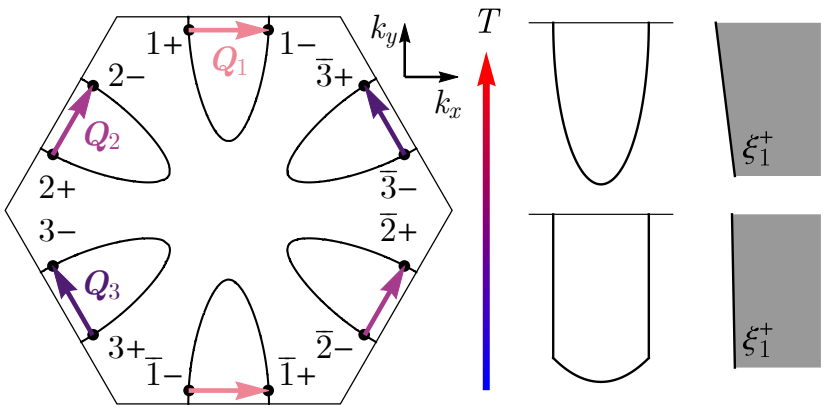

Figure 4.1: Left: A schematic of the Fermi surface of monolayer 1T-VSe_2 in the non-nested limit. At low-temperatures sections of the Fermi surface become nested. The notation of Jang *et al.* [Jang2019] is used to label the patch scheme and nesting vectors between patches. Right: Schematic diagram showing the transition of a section of the Brillouin zone of monolayer 1T-VSe_2 from an oval Fermi surface pocket to a column-like nested pocket as the temperature T is lowered. Far right: Schematic of the linearised approximation to the left-hand side of the pocket.

sion is screened by the phonons [Morel1962]. The phonons can be integrated out of the system to give an effective interaction of the form [Berger1995]

$$U^{\text{eff}}(\omega) = U - \frac{2g_{\text{ph}}^2\omega_{\text{ph}}}{\omega_{\text{ph}}^2 - \omega^2} \tag{4.3}$$

with ω_{ph} the frequency of the phonon mode and g_{ph} the electron-phonon interaction strength. At energy scales below the phonon energy, the effective attractive interaction causes by electron-phonon interactions either reduces the magnitude of the Coulomb repulsion or, for large enough electron-phonon coupling, overcomes the Coulomb repulsion to create attractive interactions between electrons. The competition of Coulomb repulsion and electron-phonon interaction using an effective interaction of the form (4.3) has been investigated in the fellow monolayer transition metal dichalcogenide NbS_2 [van Loon2018].

The patch scheme of Jang *et al.* is used to describe the twelve patches that lie on nested sections of the Fermi surface [Jang2019], as shown in Fig. 4.1. The absolute

wavevector of the centre of patch 1+ is defined as $\mathbf{K}_{1+}$ with similar definitions for the other patches. In the low energy limit the non-interacting dispersion relation is only required close to the Fermi energy. As the nested sections dominate the susceptibilities at low energies, the linearised form of the dispersion relation can be used to approximate the full dispersion of the nested regions.

The linearised dispersions close to the 1 and $\overline{1}$ patches are $\xi_1^{\pm} = \pm\delta k_x + \varepsilon\delta k_y$ and $\xi_{\overline{1}}^{\pm} = -\xi_1^{\pm}$ where $\hbar$ and the Fermi velocity v_F have been set to 1. The momenta $\delta\mathbf{k}$ are measured with respect to the centre of the corresponding patch such that the single-electron energies $\xi_n^{\pm}$ are measured with respect to the Fermi energy. The parameter ε controls the nesting of the Fermi surface. The limit $\varepsilon \to 0$ corresponds to perfect nesting.

For the second and third pockets $n = 2, 3$ the co-ordinate system is rotated so that the linearisation is correct relative to the nested surface of the pocket. The dispersion relations are $\xi_n^{\pm} \equiv \xi^{\pm}(\delta k_x^{(n)}, \delta k_y^{(n)}) = \pm\delta k_x^{(n)} + \varepsilon\delta k_y^{(n)}$ with $\delta\mathbf{k}^{(n)}$ again measured from the centre of the relative patch. The rotation of momenta relative to the co-ordinate system for patch 1 is:

$$\begin{pmatrix} k_x^{(n)} \\ k_y^{(n)} \end{pmatrix} = \begin{pmatrix} \cos(n-1)\frac{\pi}{3} & \sin(n-1)\frac{\pi}{3} \\ -\sin(n-1)\frac{\pi}{3} & \cos(n-1)\frac{\pi}{3} \end{pmatrix} \begin{pmatrix} k_x \\ k_y \end{pmatrix}. \tag{4.4}$$

The relation $\xi_{\overline{n}}^{\pm} = -\xi_n^{\pm}$ also holds for patches 2 and 3.

The dispersions can then be used to calculate the particle-particle and particle-hole susceptibilities for all possible nesting vectors between patches. The regions of integration are $\omega \in (-\infty, \infty)$ and $k_x, k_y \in (-k_c, k_c)$, where k_c is an ultraviolet momentum cutoff [Whitsitt2014]. Integration is performed over regions of singularly occupied momenta (see Fig. 4.2).

The complete particle-hole susceptibility at wavevector $\mathbf{Q}_1 = \mathbf{K}_{1+} - \mathbf{K}_{1-}$ is

$$\Pi_{\mathrm{ph}}^{\mathbf{Q}_1}(\omega) = \frac{k_c}{2\pi^2} + \frac{k_c}{4\pi^2}\log\left(\frac{\omega^2 + 4k_c^2}{\omega^2 + 4\varepsilon^2 k_c^2}\right) - \frac{\omega}{4\pi^2\varepsilon}\arctan\left(\frac{2k_c\varepsilon}{\omega}\right). \tag{4.5}$$

The Fermi surface nesting parameter ε cuts off the logarithmic divergence of $\Pi_{\mathrm{ph}}^{\mathbf{Q}_1}(\omega)$

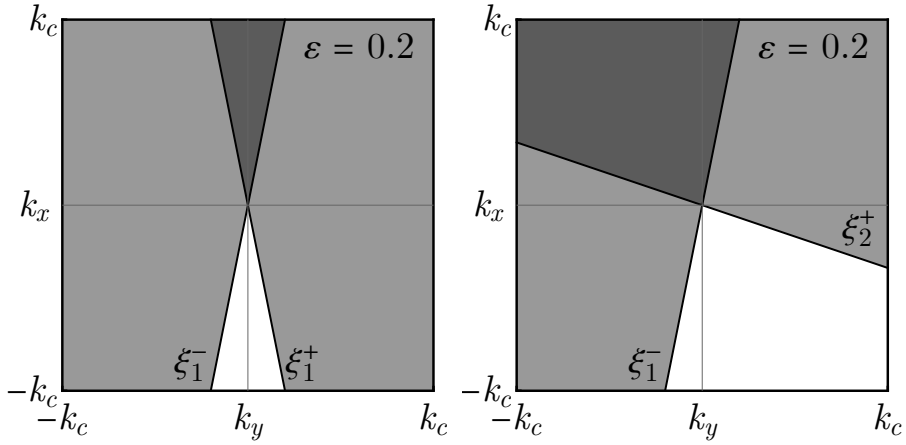

Figure 4.2: Occupied momenta for $\mathbf{q} = \mathbf{Q}_1 = \mathbf{K}_{1+} - \mathbf{K}_{1-}$ and $\mathbf{q} = \mathbf{K}_{2+} - \mathbf{K}_{1-}$ with $\varepsilon = 1/5$. Light grey region denotes singly occupied momenta, dark grey region denotes doubly occupied momenta.

in the limit $\omega \to 0$ i.e. the height of the $\omega = 0$ peak in the susceptibility is reduced as ε is increased [Maiti2013]. The zero-momentum particle-particle susceptibility has the expected logarithmic dependence in the low-energy limit, independent of ε, $\Pi_{\mathrm{pp}}^{\mathbf{0}}(\omega) \approx \frac{k_c}{2\pi^2} \log\left(\frac{k_c}{\omega}\right)$. The contributions from non-divergent arctan terms have been discarded as they are negligible when $\Pi_{\mathrm{pp}}^{0}(\omega)$ becomes large at low energies.

The particle-particle susceptibility $\Pi_{\mathrm{pp}}^{\mathbf{q}_1}(\omega)$ with $\mathbf{q}_1 = \mathbf{K}_{1+} + \mathbf{K}_{1-}$ is logarithmically divergent and dependent on the nesting parameter ε. Therefore the susceptibility can be expressed in terms of the $\mathbf{Q}_1$ particle-hole susceptibility $\Pi_{\mathrm{pp}}^{\mathbf{q}_1}(\omega) = \gamma \Pi_{\mathrm{ph}}^{\mathbf{Q}_1}(\omega)$. γ is a control parameter that has been introduced by hand to distinguish between diagrammatic contributions and to artificially suppress $\mathbf{q}_1$ nesting if desired. The particle-hole susceptibility $\Pi_{\mathrm{ph}}^{2\mathbf{K}_{1+}}(\omega)$ is always perfectly nested for the case of linear dispersion. However the Fermi surface of VSe_2 has finite length nested sections and therefore there will be curvature corrections to the dispersion which will cut off the divergence of the integral. I therefore introduce an additional parameter β with $0 \leqslant \beta \leqslant 1$ to reduce the magnitude of this susceptibility and correct for the effect of finite-length nested sections: $\Pi_{\mathrm{ph}}^{2\mathbf{K}_{1+}}(\omega) = \beta \Pi_{\mathrm{pp}}^{0}(\omega)$.

The particle-particle and particle-hole susceptibilities with nesting vectors between

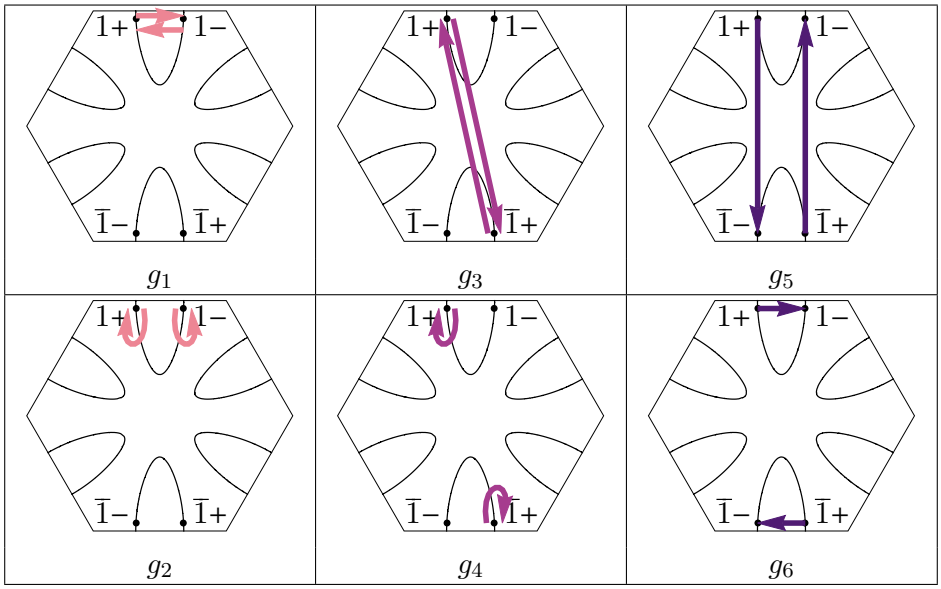

Figure 4.3: The six relevant two-particle interactions in the low-energy theory of monolayer 1T-VSe_2 constructed on the four patches of pocket '1′. g_1 and g_2 are exchange and density-density interactions between patches separated by the wavevector $\mathbf{Q}_1$, g_3 and g_4 are exchange and density-density interactions between patches with opposite momenta, and g_5 and g_6 are the two possible exchange interactions that involve all four patches.

Fermi surface patches on different pockets are non-divergent. This is because there are no non-zero $\mathbf{q}$ particle-particle bubbles between pockets and the rotation in co-ordinate systems between the separate pockets means there is no particle-hole nesting between the corresponding patches. The absence of divergent contributions from interactions between pockets allows for a further simplification of the low-energy model. It is sufficient to retain only one of the Fermi surface pockets and reduce the number of patches to four. This causes the number of possible interaction terms in the effective Lagrangian to be greatly reduced and therefore much more manageable. The caveat of this is that information is lost about the relative phase of the superconducting order parameter between different Fermi surface pockets. Additionally no information can be obtained about the competition of particle-hole nesting vectors, therefore I assume one to be dominant.

Constructing the imaginary-time effective Lagrangian, the four divergent susceptibilities cause a running of six of the nine possible interaction terms as the theory is

renormalised. Retaining only the relevant terms in the effective Lagrangian:

$$\begin{aligned}\mathcal{L} = &\sum_{s=\uparrow,\downarrow}\sum_{a=1,\bar{1}}\sum_{\nu=\pm}\overline{\psi}_{a\nu s}(\partial_\tau - \xi_a^\nu(-i\partial_x,-i\partial_y))\psi_{a\nu s}\\ &-\sum_{ss'}\sum_{a}\left[g_1\overline{\psi}_{a+s}\overline{\psi}_{a-s'}\psi_{a+s'}\psi_{a-s} + g_2\overline{\psi}_{a+s}\overline{\psi}_{a-s'}\psi_{a-s'}\psi_{a+s}\right]\\ &-\sum_{ss'}\sum_{a}\sum_{\nu}\left[\frac{g_3}{2}\overline{\psi}_{a\nu s}\overline{\psi}_{\bar{a}\nu s'}\psi_{a\nu s'}\psi_{\bar{a}\nu s} + \frac{g_4}{2}\overline{\psi}_{a\nu s}\overline{\psi}_{\bar{a}\nu s'}\psi_{\bar{a}\nu s'}\psi_{a\nu s}\right]\\ &-\sum_{ss'}\sum_{a}\left[\frac{g_5}{2}\overline{\psi}_{a+s}\overline{\psi}_{\bar{a}+s'}\psi_{a-s'}\psi_{\bar{a}-s} + \frac{g_6}{2}\overline{\psi}_{a+s}\overline{\psi}_{\bar{a}+s'}\psi_{\bar{a}-s'}\psi_{a-s} + \text{H.c.}\right], \end{aligned} \tag{4.6}$$

where $\bar{a}$ denotes the patch with opposite momentum to a. The two-particle scattering processes described by the interaction terms in the Lagrangian are depicted in Fig. 4.3.

4.3 Results.

I perform a one-loop renormalisation group analysis including all terms that are divergent or become divergent as perfect nesting is approached at low energies [Furukawa1998b, Whitsitt2014]. I introduce the renormalisation group flow parameter $y = \log\left(\frac{k_c}{\omega}\right)$ which diverges to infinity as $\omega \to 0$ and introduce the rescaled interactions parameters $g_i \to \frac{k_c}{2\pi^2} g_i$. The resulting flow equations are:

$$\dot{g}_1 = 2d^\varepsilon(y)\left(-g_1^2 + (1-\gamma)g_1g_2 + g_5g_6 - g_6^2\right), \tag{4.7}$$

$$\dot{g}_2 = d^\varepsilon(y)\left(-\gamma g_1^2 + (1-\gamma)g_2^2\right), \tag{4.8}$$

$$\dot{g}_3 = -2\beta g_3^2 - 2(1-\beta)g_3g_4 - 2g_5g_6, \tag{4.9}$$

$$\dot{g}_4 = -(1-\beta)g_4^2 - g_5^2 - g_6^2, \tag{4.10}$$

$$\dot{g}_5 = -g_3g_6 - g_4g_5 + 2d^\varepsilon(y)g_2g_5, \tag{4.11}$$

$$\dot{g}_6 = -g_3g_5 - g_4g_6 + 2d^\varepsilon(y)(g_1g_5 + g_2g_6 - 2g_1g_6). \tag{4.12}$$

$\dot{g}_i$ again denotes the derivative $\frac{dg_i}{dy}$. The y-dependence of the couplings g_i is also suppressed. The function $d^\varepsilon(y)$ describes the ratio of the $\mathbf{Q}_1$ particle-hole susceptibility and

the zero momentum particle-particle susceptibility in terms of the flow parameter y and the nesting parameter ε. For the remainder of he chapter $\gamma = 1$.

As y is increased in the solution of the differential equations the couplings diverge at a critical value of y. To allow for a precise numerical solution the flow is stopped when the largest of the couplings g_i becomes equal to one. This sets a critical value $y = y_c$ for which the interactions becomes strong coupling and the weak-coupling approximation breaks down. At this point a subset of the couplings have become several orders of magnitude larger than their initial values. This signals the breakdown of the weak-coupling perturbation theory and the onset of an ordered phase. The finite critical value y_c is an artefact of the one-loop RG. When higher-loop corrections are included they should shift the divergence to $y_c \to \infty$. I consider no phase transition to have occurred if no couplings have reached the value of one by the time $y = 1/U$.

In the limit $y \to 0$ with ε small, $d^\varepsilon \approx 1 - \frac{\varepsilon^2}{3\log 2}$. In the large-$y$ limit $d^\varepsilon(y)$ takes the form $d^\varepsilon(y \to y_c) = ((1-\varepsilon^2)e^y)/((1+e^y)(1+\varepsilon^2 e^y))$. The function $d^\varepsilon(y)$ is therefore approximated as:

$$d^\varepsilon(y) = \frac{d\Pi_{\text{ph}}^{\mathbf{Q}_1}}{d\Pi_{\text{pp}}^{0}} \approx \frac{1 - \frac{\varepsilon^2}{3\log 2}}{1 + \varepsilon^2 e^y}, \tag{4.13}$$

which interpolates between the $y \to 0$ and $y \to y_c$ limits. The function $d^\varepsilon(y)$ is plotted in Fig. 4.4.

The initial conditions for the couplings are approximated by evaluating $V_0(\mathbf{k}_1, \mathbf{k}_2, \mathbf{k}_3)$, defined in equation (4.2), at the Fermi surface patches for the different interaction momentum transfers. The couplings are then further simplified so that only two possible initial coupling strengths

$$V_1 \approx U + V - \frac{7}{4}J, \qquad \text{and} \qquad V_2 \approx U + 3V - \frac{5}{4}J \tag{4.14}$$

are available. The initial conditions at $y = 0$ for the couplings are $g_1^0 \approx g_3^0 \approx g_6^0 \approx V_1$ and $g_2^0 \approx g_4^0 \approx g_5^0 \approx V_2$. The effect of this approximation is to split the solutions into three regions: (i) $V_1, V_2 > 0$, all couplings repulsive in the ultraviolet; (ii) $V_2 > 0, V_1 < 0$; and (iii) $V_1, V_2 < 0$, i.e. all couplings attractive. The second simplification allows

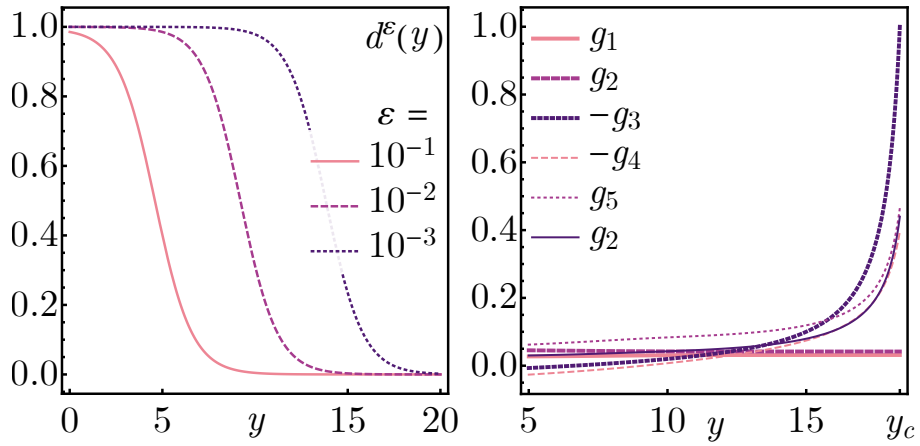

Figure 4.4: Left: Plot of $d^\varepsilon(y)$ for $\varepsilon = 10^{-1}, 10^{-2}, 10^{-3}$. Right: Plot of divergence of couplings g_i under the renormalisation group flow as a function of y with $\varepsilon = 10^{-2}$, $\gamma = 1$, $\beta = 1/2$, $U = 0.04$, $V = 0.2U$, and $J = 0.3U$.

for a two dimensional theory space to visualise the role of attractive versus repulsive components of the interactions; however, using a more general microscopic model with the full $V_0(\mathbf{k}_1, \mathbf{k}_2, \mathbf{k}_3)$ the initial conditions of the couplings g_i^0 would be independent. The mapping between the effective initial couplings of the intermediate Hamiltonian J and V and the renormalisation group couplings V_1 and V_2 is shown in Fig. 4.5.

Again considering the effect of phonons, the contact and long-range Coulomb repulsions will be screened by the phonons and reduced in magnitude. Assuming that no phase transition has occurred above the characteristic Debye energy of the phonon, the couplings V_1 and V_2 can be modified during the flow with the substitution $U \to U_{\text{eff}}$ with $U_{\text{eff}} \approx U - \frac{2g_{\text{ph}}^2}{\omega_{\text{ph}}}$ and the magnitude of the long-range Coulomb repulsion similarly reduced; $V \to V_{\text{eff}}$. This will greatly enlarge the area of the phase diagram for which V_1 and V_2 are attractive. However, I have not directly implemented this procedure in the calculations as there is no prior theory showing that phonons can be included via an effective interaction in a controlled way within the Parquet renormalisation group.

To find which orders are possible I introduce test vertices for all two-particle corre-

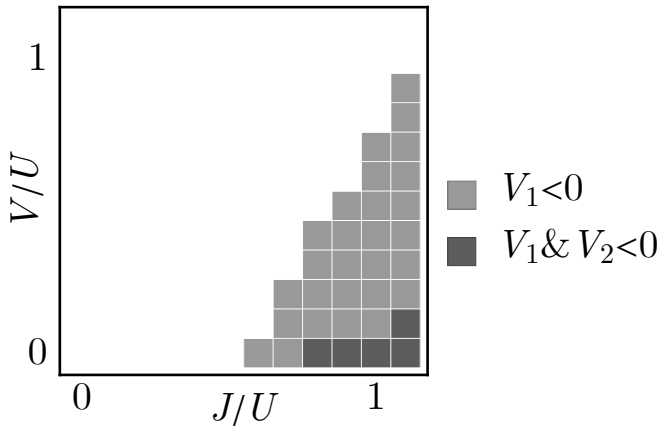

Figure 4.5: A plot of the mapping between the effective nearest-neighbour Coulomb repulsion V and Heisenberg exchange interaction J and the coupling constants V_1 and V_2, defined in (4.14). The couplings correspond to the initial conditions $g_1^0 \approx g_3^0 \approx g_6^0 \approx V_1$ and $g_2^0 \approx g_4^0 \approx g_5^0 \approx V_2$ in the model.

lators allowed in the model and calculate the corresponding one-loop vertex corrections.

$$\delta\mathcal{L} = \frac{1}{2}\sum_{a=1,\bar{1}}\sum_{\nu=\pm}\left[\Delta_{a\nu\bar{a}\nu}\overline{\psi}_{a\nu\uparrow}\overline{\psi}_{\bar{a}\nu\downarrow} + \text{H.c.}\right] + \sum_{a}\sum_{\nu}\sum_{\sigma}\phi_{a\nu\bar{a}\nu}\overline{\psi}_{a\nu}\psi_{\bar{a}\nu} \tag{4.15}$$

This gives the susceptibilities of the possible order parameters. In the particle-particle channel the interactions can be rewritten in the form

$$\frac{d}{dy}\begin{pmatrix}\Delta_{1+\bar{1}+}\\ \Delta_{1-\bar{1}-}\\ \Delta_{\bar{1}+1+}\\ \Delta_{\bar{1}-1-}\end{pmatrix} = -2\begin{pmatrix} g_4 & g_8 & g_3 & g_7\\ g_8 & g_4 & g_7 & g_3\\ g_3 & g_7 & g_4 & g_8\\ g_7 & g_3 & g_8 & g_4\end{pmatrix}\begin{pmatrix}\Delta_{1+\bar{1}+}\\ \Delta_{1-\bar{1}-}\\ \Delta_{\bar{1}+1+}\\ \Delta_{\bar{1}-1-}\end{pmatrix}. \tag{4.16}$$

The eigenvectors of the matrix are:

$$\Delta_s = \frac{\Delta}{2}\begin{pmatrix}1\\1\\1\\1\end{pmatrix}, \quad \Delta_d = \frac{\Delta}{2}\begin{pmatrix}-1\\1\\-1\\1\end{pmatrix}, \quad \Delta_p = \frac{\Delta}{2}\begin{pmatrix}-1\\-1\\1\\1\end{pmatrix}, \quad \Delta_f = \frac{\Delta}{2}\begin{pmatrix}1\\-1\\-1\\1\end{pmatrix}. \tag{4.17}$$

These eigenvectors define the pairing symmetry. The corresponding eigenvalues are:

$$\lambda_s = -g_3 - g_4 - g_5 - g_6, \qquad \lambda_d = -g_3 - g_4 + g_5 + g_6,$$
$$\lambda_p = g_3 - g_4 + g_5 - g_6, \qquad \lambda_f = g_3 - g_4 - g_5 + g_6. \tag{4.18}$$

The Δ_j obey the flow equation $\frac{d}{dy}\Delta_j = -2\lambda_j\Delta_j$.

The SDW and CDW susceptibilities are calculated via $\chi^{\mathbf{q}}_{\mathrm{SDW}} = \chi^{\mathbf{q},\mathrm{ph}}_{\uparrow\uparrow} - \chi^{\mathbf{q},\mathrm{ph}}_{\downarrow\downarrow}$, $\chi^{\mathbf{q}}_{\mathrm{CDW}} = \chi^{\mathbf{q},\mathrm{ph}}_{\uparrow\uparrow} + \chi^{\mathbf{q},\mathrm{ph}}_{\downarrow\downarrow}$ [Whitsitt2014].

The possible superconducting symmetries are defined in analogy to their continuum analogues, despite the system being on a lattice. The superconducting symmetry is further contained by the discrete set of patches. The reason for the naming convention chosen is: the s-wave eigenvector predicts an isotropic gap, while the d-wave eigenvector leads to four nodes on each Fermi surface pocket. The p-wave and f-wave eigenvectors each give two nodes per pocket; however, the p-wave order parameter naively changes sign twice as a function of angle in the Brillouin zone, whereas the f-wave order parameter changes sign six times.

Due to only retaining one of the pockets in the patch approximation the relative phases of the superconducting order parameter between pockets cannot be predicted. Additionally which of the possible charge density wave vectors $\mathbf{Q}_i$ is chosen when the ordered phase is reached cannot be predicted. To calculate which ordering vector is chosen a multi-component order parameter theory is required [Jang2019].

As the couplings g_i diverge at some critical value y_c during the flow of the renormalisation group equations it is helpful to introduce the asymptotic form

$$g_i = \frac{G_i}{y_c - y}. \tag{4.19}$$

As $y \to y_c$ the divergences of the order parameter susceptibilities can be expressed in a power-law form $\chi_j(y) = (y_c - y)^{\alpha_j}$, with $\alpha_j \in \{\alpha^s_{\mathrm{SC}}, \alpha^d_{\mathrm{SC}}, \alpha^p_{\mathrm{SC}}, \alpha^f_{\mathrm{SC}}, \alpha^{\mathbf{Q}_1}_{\mathrm{SDW}}, \alpha^{\mathbf{Q}_1}_{\mathrm{CDW}},$

$\alpha_{\mathrm{SDW}}^{2\mathbf{K}_{1+}}$, $\alpha_{\mathrm{CDW}}^{2\mathbf{K}_{1+}}\}$. The exponents are given by:

$$\alpha_{\mathrm{SC}}^{s} = 2(G_3 + G_4 + G_5 + G_6), \tag{4.20}$$

$$\alpha_{\mathrm{SC}}^{d} = 2(G_3 + G_4 - G_5 - G_6), \tag{4.21}$$

$$\alpha_{\mathrm{SC}}^{p} = 2(-G_3 + G_4 - G_5 + G_6), \tag{4.22}$$

$$\alpha_{\mathrm{SC}}^{f} = 2(-G_3 + G_4 + G_5 - G_6), \tag{4.23}$$

$$\alpha_{\mathrm{SDW}}^{\mathbf{Q}_1} = -2d^{\varepsilon}(y_c)\,(G_2 + G_5)\,, \tag{4.24}$$

$$\alpha_{\mathrm{CDW}}^{\mathbf{Q}_1} = 2d^{\varepsilon}(y_c)\,(2G_1 - G_2 - G_5 + 2G_6)\,, \tag{4.25}$$

$$\alpha_{\mathrm{SDW}}^{2\mathbf{K}_{1+}} = -2\beta G_4, \tag{4.26}$$

$$\alpha_{\mathrm{CDW}}^{2\mathbf{K}_{1+}} = -2\beta\,(G_4 - 2G_3)\,. \tag{4.27}$$

It is important to note that ferromagnetic instabilities are suppressed within the patch scheme approximation made. Ferromagnetism requires the full Fermi surface to see the full divergences in the zero momentum particle-hole susceptibility. Ferromagnetic phases have been observed experimentally in monolayer VSe_2 [Bonilla2018]. However, additional studies have shown a suppression of ferromagnetism close to the charge density wave phase as Fermi surface nesting dominates the physics [Fumega2019].

In the alternative triangular Fermi surface case discussed in the introduction the definitions of intra- vs. inter-pocket scattering have to be altered to correctly describe the physics. The charge density wave nesting vectors are not changed but the f-wave superconductivity phase would be replaced by an $s_{\pm}$ order parameter.

To investigate the phase diagram I solve equations (4.7–4.12) numerically with the initial conditions $g_i(y = 0) = g_i^0$. One instance of the solution to these equations is plotted in Fig. 4.4. When $V = J = 0$ there is purely on-site Coulomb repulsion and all interactions g_i have the same initial conditions. In this case only two instabilities are predicted: s-wave superconductivity for when the interactions are initially attractive and d-wave superconductivity when the interactions are initially repulsive. When V and J are non-zero additional phases arise due to some of the initial interactions changing

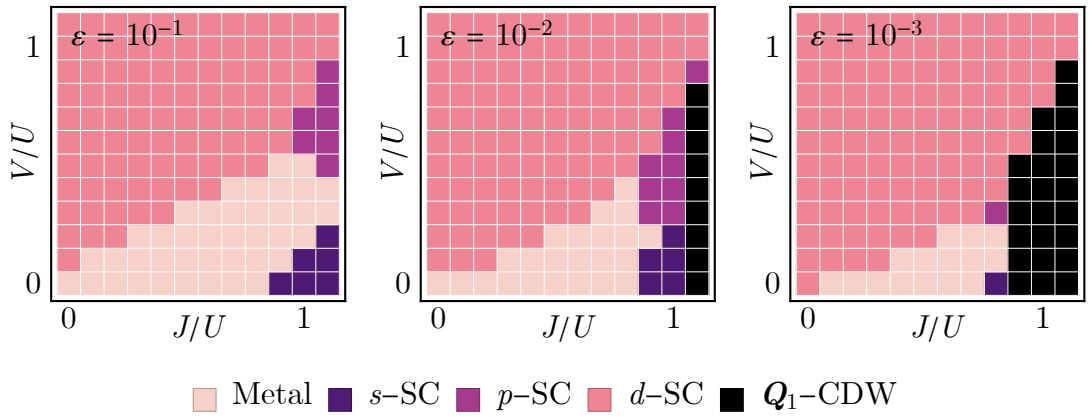

Figure 4.6: Phase diagrams for model of monolayer 1T-VSe_2 calculated from renormalisation group flows. The degree of Fermi surface nesting is increased from left to right ($\varepsilon = 10^{-1}, 10^{-2}, 10^{-3}$). The parameter $\beta = 1/2$ emulates the curvature corrections caused by the finite length of the nested sections of the Fermi surface and $\gamma = 1$.

sign. The phase diagrams for the nesting strengths ($\varepsilon = 10^{-1}, 10^{-2}, 10^{-3}$) are plotted in Fig. 4.6. When all interactions begin repulsive the model behaves as before and the leading instability is to d-wave superconductivity. When some of the initial interactions become attractive, regions of both s-wave and p-wave superconductivity arise. As the nesting strength is increased sections of the s-wave and p-wave superconducting regions are replaced by a charge density wave phase where the Heisenberg exchange interaction is on the order of the bare contact Coulomb repulsion.

4.4 Summary and discussion

I have performed a renormalisation group analysis on an extended Hubbard model of monolayer VSe_2 in order to analyse the effect of Fermi surface nesting on charge density wave formation in the transition metal dichalcogenides. I retain both particle-particle and particle-hole channels in a parquet approach to capture the interplay and competition of superconducting and density wave instabilities. The phase diagram exhibits d-wave superconductivity for purely repulsive interactions with regions of s-wave and p-wave superconductivity when components of the initial interactions become attractive.

As the nesting of the Fermi surface is increased, a charge density wave region emerges.

The requirement for charge density wave formation in the model is both that components of the initial interactions are attractive and that the Fermi surface has sufficiently nested regions. The region of attractive interactions is achieved in the purely electronic model via a strong effective Heisenberg exchange coupling. For a purely electronic calculation all interactions begin repulsive unless the Heisenberg exchange interaction is of the order of the bare contact Coulomb repulsion. Other mechanisms may also be involved that can complement or replace the exchange interaction in providing the required attractive interactions needed for charge density wave formation. One possible mechanism is via electron-phonon interactions screening the Coulomb repulsion and increasing the region of attractive interactions in the model.

The formation of a charge density wave at strong Heisenberg exchange coupling is naively a surprising result, as usually magnetic ordering would be expected. However, the exchange interaction is still on the order of the Coulomb repulsion and the charge density wave formed is incommensurate. Ordering in the model is due to the feedback between different channels as the temperature is lowered and not due to the mean-field ground state of the J interaction term, which would favour a commensurate spin density wave. This is not possible in the above scheme due to the location of the patches. The likelihood of such strong exchange interaction occurring as a bare interaction in real materials is unlikely with J rarely exceeding $0.5U$. However, the exchange coupling included in the low-energy model is already effective and so could occur if the exchange coupling was renormalised from the microscopic model for example in the vicinity of a magnetic phase or via other unforeseen effects. The high value of J along with the enhancement of the attractive region of the phase diagram by electron-phonon interactions suggests that both electronic and phonon effects may be vital in reaching the charge density wave phase in the transition metal dichalcogenides.

It is important to note that the Fermi surface nesting is a control parameter which is tuned in the analysis and is not renormalised by self energy corrections within this scheme. However, taking into account the corrections to the dispersions on the patches

via an effective fermion + order parameter theory, a flow to perfect nesting is predicted [Jang2019, Metlitski2010b, Sur2015]. However, this is not always the case; other studies show a Fermi surface with power-law curvature at the hot spots which does not become perfectly nested [Sur2016, Halbinger2019]. As a flow to perfect nesting is predicted by Jang *et al.* [Jang2019], the analysis performed above is complementary to their work, predicting charge density wave formation without any a priori mean-field assumption. In addition it takes into account the role of superconducting fluctuations and their competition with possible density wave orders in the system.

The charge density wave forms along the $\mathbf{Q}_1$ wavevector. Even if the curvature corrections are ignored and perfect nesting is assumed along the $\mathbf{q}_1$ wavevector this nesting vector is not favoured. This result also agrees with Jang *et al.* [Jang2019] and gives a viable prediction for a nesting mechanism in at least a subset of the monolayer transition metal dichalcogenides.

Chapter 5

Mixed-parity superconductivity near Lifshitz transitions in strongly spin-orbit-coupled metals

5.1 Introduction

In this chapter I will investigate the effects of strong spin-orbit coupling on superconductivity and density wave formation in two-dimensional lattice systems. Symmetry dependent spin-orbit coupling arises in systems without inversion symmetry such as non-centrosymmetric crystal structures and at interfaces.

To investigate spin-orbit coupling in materials I consider the non-interacting Hamiltonian in momentum space

$$H_0 = \sum_{\mathbf{k},s=\uparrow,\downarrow} \xi_{\mathbf{k}} c^\dagger_{\mathbf{k}s} c_{\mathbf{k}s} + \sum_{\mathbf{k},ss'} \mathbf{g}_{\mathbf{k}} \cdot c^\dagger_{\mathbf{k}s} \boldsymbol{\sigma} c_{\mathbf{k}s'}. \tag{5.1}$$

$\boldsymbol{\sigma} = (\sigma_x, \sigma_y, \sigma_z)^{\mathrm{T}}$ is the vector of Pauli matrices and $\mathbf{g}_{\mathbf{k}}$ is a spin-orbit coupling term with a general momentum dependence. Under the time reversal operation the momenta and spin are inverted, $\mathbf{k} \to -\mathbf{k}$ and $\mathbf{S} \to -\mathbf{S}$. Under an inversion operation only the

momenta are inverted $\mathbf{k} \to -\mathbf{k}$. In the case of time reversal symmetry this requires

$$\xi_{\mathbf{k}} = \xi_{-\mathbf{k}} \qquad \text{and} \qquad \mathbf{g}_{\mathbf{k}} = -\mathbf{g}_{-\mathbf{k}} \tag{5.2}$$

for the Hamiltonian to be invariant. For invariance under inversion

$$\xi_{\mathbf{k}} = \xi_{-\mathbf{k}} \qquad \text{and} \qquad \mathbf{g}_{\mathbf{k}} = \mathbf{g}_{-\mathbf{k}}. \tag{5.3}$$

If both symmetries are preserved it follows that $\mathbf{g}_{\mathbf{k}}$ must be zero. In the presence of a uniform magnetic field h, time-reversal symmetry is broken and $\mathbf{g}_{\mathbf{k}}$ takes the momentum independent form $\mathbf{g}_{\mathbf{k}} = hs\hat{\mathbf{z}}$. This causes a modification of the Hamiltonian to $H_0 = \sum_{\mathbf{k},s}(\xi_{\mathbf{k}} + hs)c^{\dagger}_{\mathbf{k}s}c_{\mathbf{k}s}$ such that the Fermi surface is split into two and spin degeneracy is lost.

The term $\mathbf{g}_{\mathbf{k}}$ can also be momentum dependent such as in systems with broken inversion symmetry. Inversion symmetry is broken in lattices lacking an inversion centre; the material is not invariant under the transformation $\hat{\mathbf{z}} \to -\hat{\mathbf{z}}$. Crystals lacking an inversion centre, non-centrosymmetric materials, are common with a large number of possible non-centrosymmetric crystallographic space groups [Bauer2012]. Considering such a material with inversion symmetry broken along the $\hat{\mathbf{z}}$ axis, or equally a thin film with a transverse electric field, relativistic effects generate a spin-orbit coupling term [Sigrist2009]

$$-\frac{e}{2m_e c^2}(\nabla V(\mathbf{r}) \times \mathbf{v}) \cdot \mathbf{S}. \tag{5.4}$$

Replacing the gradient of the internal potential $V(\mathbf{r})$ with a uniform electric field $\mathbf{E} = -\nabla V(\mathbf{r})$ in the $\hat{\mathbf{z}}$ direction and performing a small $\mathbf{k}$ expansion leads to Rashba spin-orbit coupling term $\mathbf{g}_{\mathbf{k}}$ of the form

$$\mathbf{g}_{\mathbf{k}} = \upsilon(\hat{\mathbf{z}} \times \mathbf{k}) \tag{5.5}$$

with all constant prefactors from (5.4), and additional prefactors generated in the algebraic manipulation to the form (5.5), contained within the constant υ. The mixing of spin and momentum means these quantities are no longer good quantum numbers. Perform-

ing a unitary transformation to the helicity basis the Hamiltonian is $H_0 = \sum_{k,\alpha} \xi_k^\alpha c_{k\alpha}^\dagger c_{k\alpha}$, with the two helicities denoted by Greek indices $\alpha \in \{+, -\}$. The modified electronic dipersions become

$$\xi_{\mathbf{k}}^{\pm} = \xi_{\mathbf{k}} \pm |\mathbf{g}_{\mathbf{k}}| \tag{5.6}$$

with the eigenvectors

$$|\eta_{\pm}(\mathbf{k})\rangle = \frac{1}{\sqrt{2|\mathbf{g}_{\mathbf{k}}|(|\mathbf{g}_{\mathbf{k}}| \pm \mathrm{g}_{\mathbf{k}}^z)}} \begin{pmatrix} |\mathbf{g}_{\mathbf{k}}| \pm \mathrm{g}_{\mathbf{k}}^z \\ \pm(\mathrm{g}_{\mathbf{k}}^x + i\mathrm{g}_{\mathbf{k}}^y) \end{pmatrix}. \tag{5.7}$$

The presence of antisymmetric spin-orbit coupling mixes the spin and momentum degrees of freedom and induces spin flips during electron scattering processes. This alters how the superconductivity is formed such that the superconductivity can no longer be thought of in terms as purely even-parity or odd-parity. This mixing of the superconducting parities intrinsically gives an enhancement of the triplet component of the superconducting order parameter, important for topological superconductivity [Yokoyama2007].

5.2 Model and methods

The model I shall investigate is the square-lattice Hubbard model with an additional Rashba spin-orbit coupling term, denoted the Rashba-Hubbard model in the literature. The model captures the spin-orbit interaction effects on the lattice, splitting the bare tight-binding band into two bands with non-trivial spin textures also dependent on the tight-binding parameters. It also captures the effect of electron-electron repulsion via on-site Coulomb repulsion.

Early analysis carried out on the extended Rashba-Hubbard model using the random phase approximation (RPA) suggested mixed-parity superconductivity [Yokoyama2007, Shigeta2013], whereas later studies found only even- or odd-parity regions, with d-wave or f-wave superconductivity dominant [Greco2018, Ghadimi2019]. Additionally dynamical mean-field-theory studies found mixed-parity superconductivity with $(d + p)$-wave symmetry [Lu2018].

To simplify the calculation I shall focus on a particular characteristic of the two-dimensional Hubbard model, the presence of saddle points in the non-interacting band dispersion. As the chemical potential is raised with electron doping through the saddle point a Lifshitz transition occurs whereby the Fermi surface transitions between an open and closed Fermi surface, or two or more Fermi surface pockets connect [Lifshitz1960, Volovik2017]. The saddle-point in the band structure causes a van Hove singularity where the density of states in the region of the saddle-point becomes divergent. If two Fermi surface regions connect at the van Hove singularity, the density of states diverges logarithmically at the saddle point location on the Fermi surface. Due to the logarithmic divergences at the van Hove saddle points of the Fermi surface, a patch approximation can be constructed which greatly simplifies the calculation and removes a large number of irrelevant interaction terms [Schulz1987, Lederer1987, Furukawa1998a]. I will use this simplification to examine the possible Fermi surface instabilities of the system.

In the Rashba-Hubbard system there are two possible chemical potentials that exhibit a van Hove singularity. At each van Hove filling all the van Hove points lie on one Fermi surface sheet so that the predominant contribution to the susceptibilities comes from a single band at low energies. Each band is only populated by electrons of one helicity.

I consider the limit when the electron-electron interactions are much weaker than the Rashba coupling. This is because in the limit of weak electron-electron interaction scattering will primarily be intra-band. This allows for the retention of only the band which the van Hove points lie upon. When electron-electron interactions are stronger than or of the same order to the Rashba interaction, inter-band scattering between the two helicity bands will occur and the patch approximation made will no longer be valid.

I construct the patch scheme following [Yao2015, Nandkishore2012, Huang2016] which is a applicable near the two van Hove fillings of the Rashba-Hubbard model. In the limit of weak coupling a one-loop renormalisation group analysis can be applied to find the leading instability of the system.

The form of the electronic dispersion and enhanced divergences of the susceptibilities at a van Hove singularity introduce additional complications in a rigorous renormalisa-

tion group treatment of the problem [Ghamari2015, Kapustin2018]. Both momentum and energy cutoffs are required to keep the Wilsonian effective theory local. Further, the effective theory is intrinsically non-local at exactly the Lifshitz transition quantum critical point. Within the Wilsonian scheme, the interaction in the zero momentum particle-particle channel grows as the square of the logarithm of the energy in agreement with the naive divergence of susceptibilities [Ghamari2015]. In order to implement the Parquet renormalisation group scheme to examine the competition of phases, a simplification of the analysis is required to obtain results as the renormalisation group scheme is not formalised for multiple van Hove points. A singular energy cutoff replaces the two separate cutoffs of the rigorous scheme. The interactions remain marginal at tree level and therefore a one-loop renormalisation group analysis is believed to provide a qualitative description of the low energy phases of the relevant system close to a van Hove singularity [Schulz1987, Lederer1987, Furukawa1998a, Nandkishore2012, Yao2015].

Firstly I consider a non-interacting square lattice tight-binding model with Rashba spin-orbit coupling,

$$\begin{aligned} H_0 = &- t \sum_{\langle i,j\rangle,s} c^\dagger_{is} c_{js} - t' \sum_{\langle\langle i,j\rangle\rangle,s} c^\dagger_{is} c_{js} - \mu \sum_{i,s} c^\dagger_{is} c_{is} \\ &+ i\upsilon \sum_{\langle i,j\rangle,s,s'} \left[(\boldsymbol{\sigma} \times \mathbf{a}_{ij}) \cdot \hat{\mathbf{z}}\right]_{ss'} c^\dagger_{is} c_{js'}. \end{aligned} \tag{5.8}$$

$\langle i,j\rangle$ and $\langle\langle i,j\rangle\rangle$ denote nearest-neighbour and next-nearest-neighbour hopping with hopping strengths t and t' respectively. The spin orientations are denoted $s, s' \in \{\uparrow, \downarrow\}$. The Rashba spin-orbit coupling υ is strong and included on the level of the lattice and not as a perturbation. $\mathbf{a}_{ij}$ denotes the unit vectors between nearest-neighbour sites.

Introducing interactions the Hubbard interaction term is

$$V_{\text{int}} = \frac{U}{2} \sum_{s,s'} \sum_{k_1 k_2 k_3 k_4} \delta_{k_1+k_2-k_3-k_4} c^\dagger_{k_4 s} c^\dagger_{k_3 s'} c_{k_2 s'} c_{k_1 s}. \tag{5.9}$$

V_{int} describes a contact interaction which is repulsive for $U > 0$ and attractive for $U < 0$. The interacting Hamiltonian H is $H_0 + V_{\text{int}}$.

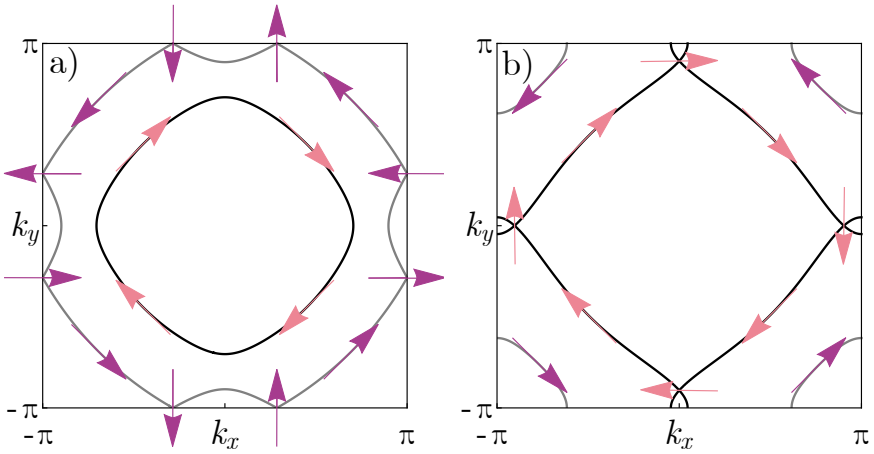

Figure 5.1: a) The two Fermi-surface sheets when the chemical potential is μ_-. b) The Fermi surface sheets for chemical potential μ_+. μ_- and μ_+ are the two chemical potentials for which the van Hove singularity occurs. μ_- is the chemical potential for which the van Hove points lie on the outer Fermi surface sheet and μ_+ is the chemical potential for which the van Hove points lie on the inner sheet. In both figures the arrows running around the Fermi surface sheets indicate the direction of the helicity eigenstates on that sheet of the Fermi surface. The parameters used in the figures are $t = 1$, $t' = 0.3$, and $\upsilon = 0.5$.

Again the spin-orbit coupling term breaks the spin degeneracy of the non-interacting bands and splits them into two bands with opposite helicities. The tight-binding bands are

$$\xi_k^{\pm} = \epsilon_k - \mu \pm 2\upsilon\sqrt{\sin^2 k_x + \sin^2 k_y} \tag{5.10}$$

with ϵ_k the next-nearest-neighbour Hubbard model dispersion

$$\epsilon_k = -2t(\cos k_x + \cos k_y) - 4t' \cos k_x \cos k_y. \tag{5.11}$$

The lattice spacing has been set to unity for simplicity. As $g_{\mathbf{k}}^z = 0$ the eigenvector of the helicity eigenstates takes the form

$$|\eta_{\pm}(\mathbf{k})\rangle = \frac{1}{\sqrt{2}} \begin{pmatrix} 1 \\ \pm e^{i\theta(\mathbf{k})} \end{pmatrix} \tag{5.12}$$

with the phase factor

$$e^{i\theta(\mathbf{k})} = \frac{\sin k_y - i \sin k_x}{\sqrt{\sin^2 k_x + \sin^2 k_y}}. \tag{5.13}$$

The spin orientations along the helicity bands are shown in Fig. 5.1. The corresponding operator mapping between the spin basis and the helicity basis is given by

$$c_{k\pm} = \frac{1}{\sqrt{2}}(c_{k\uparrow} \pm e^{-i\theta(\mathbf{k})} c_{k\downarrow}). \tag{5.14}$$

After the transformation between bases is performed the bare Hubbard interaction is [Wang2014]

$$\begin{aligned} V_{\text{int}} \quad = \quad & \frac{U}{16} \sum_{\alpha\beta\gamma\delta} \sum_{k_1 k_2 k_3 k_4} \delta_{k_1+k_2-k_3-k_4} (\alpha e^{-i\theta(\mathbf{k}_4)} - \beta e^{-i\theta(\mathbf{k}_3)}) \\ & \times (\delta e^{i\theta(\mathbf{k}_1)} - \gamma e^{i\theta(\mathbf{k}_2)}) c^\dagger_{k_4\alpha} c^\dagger_{k_3\beta} c_{k_2\gamma} c_{k_1\delta}. \end{aligned} \tag{5.15}$$

The interaction term has been written such that the antisymmetrisation is explicit.

The two possible van Hove fillings are located at the chemical potentials μ_+ and μ_-, given by

$$\mu_\pm = \pm 2 \left(-t + \frac{(t \pm 2t')^2}{\sqrt{(t \pm 2t')^2 + v^2}} + v \sqrt{1 - \frac{(t \pm 2t')^2}{(t \pm 2t')^2 + v^2}} \right). \tag{5.16}$$

For each of the van Hove fillings there are four van Hove points in the Brillouin zone, shown in Fig. 5.1. The filling μ_+ is similar to the van Hove scenario proposed by Yao and Yang [Yao2015]. They denote this singularity a type-II van Hove singularity as the van Hove saddle points are located away from the Brillouin zone edge and unlike previously investigated (type-I) models where the van Hove points lie on the Umklapp surface at the zone edge [Schulz1987, Lederer1987, Furukawa1998a]. I shall refer to the μ_+ case as the Yao-Yang scenario. In the μ_- case the type-I van Hove point splits into two along the Brillouin zone edge and the points move away from the Umklapp surface. I shall denote this case the edge van Hove scenario. The van Hove points lie at $\mathbf{K}_{1,2} = (\mp\Upsilon^+, 0)$, $\mathbf{K}_{3,4} = (0, \mp\Upsilon^+)$ for filling μ_+ and $\mathbf{K}_{1,2} = (\mp\Upsilon^-, \pi)$, $\mathbf{K}_{3,4} = (-\pi, \mp\Upsilon^-)$ for filling μ_-,

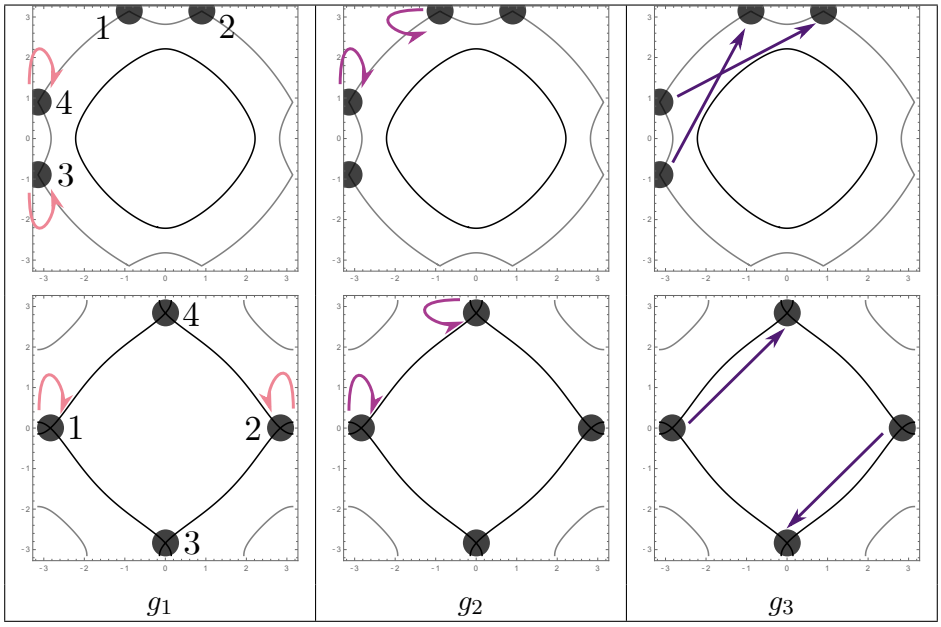

Figure 5.2: Possible interactions allowed for spinless fermions between the four patches. Fermi surfaces are at chemical potential μ_- in the top row and μ_+ in the bottom row. The g_1 and g_2 couplings are density-density interactions between patches with zero and non-zero total momenta respectively. g_3 is an exchange interaction that involves all the pairs of patches with zero total momentum between them.

where

$$\Upsilon^{\pm} = \arccos\left(\mp\frac{t \pm 2t'}{\sqrt{(t \pm 2t')^2 + v^2}}\right). \tag{5.17}$$

In the low energy limit the imaginary time Lagrangian of spinless fermions that applies close to the two van Hove fillings is

$$\begin{aligned}\mathcal{L}_{\pm} = &\sum_{a=1}^{4} \psi_a^{\dagger}(\partial_\tau - \xi_a^{\pm}(-i\partial_x, -i\partial_y))\psi_a - \frac{g_1}{2}\psi_a^{\dagger}\psi_{\bar{a}}^{\dagger}\psi_{\bar{a}}\psi_a \\ &- \sum_{a=1}^{2}\sum_{b=3}^{4} g_2\psi_a^{\dagger}\psi_b^{\dagger}\psi_b\psi_a - \left[ig_3\psi_4^{\dagger}\psi_3^{\dagger}\psi_2\psi_1 + \text{H.c.}\right].\end{aligned} \tag{5.18}$$

Only states around the van Hove points are retained within the theory due to their enhanced contribution to the low energy physics. The patch scheme reduces the full Fermi surface down to four regions with only three possible interactions due to the spinless nature of the patches. The possible interactions for the two fillings are depicted

in Fig. 5.2. The patches are numbered in the same way as the Fermi surface patches on the left hand of Fig. 5.2; $\bar{a}$ denotes the patch with opposite momentum to patch a. The couplings g_i are marginal at tree level, allowing for the application of a one-loop renormalisation group analysis to the weakly coupled problem. Density-density interactions on the same patch have a momentum prefactor and are therefore irrelevant and discarded from the effective field theory.

For the edge van Hove scenario there are four inequivalent scattering vectors between patches. However, if four separate g_2 processes are included in the effective Lagrangian then the couplings diverge equally under the renormalisation group and are indistinguishable during the flow. Therefore I include only one g_2 coupling, identical for all scattering vectors.

The dispersions at the van Hove points are

$$\xi^{\pm}_{1,2}(\mathbf{k}) = -\frac{\delta k_x^2}{2m_x^{\pm}} + \frac{\delta k_y^2}{2m_y^{\pm}}, \quad \xi^{\pm}_{3,4}(\mathbf{k}) = -\frac{\delta k_y^2}{2m_x^{\pm}} + \frac{\delta k_x^2}{2m_y^{\pm}}; \tag{5.19}$$

$$m_x^{\pm} = \pm\frac{1}{\sqrt{(t \pm 2t')^2 + \upsilon^2}}, \tag{5.20}$$

$$m_y^{\pm} = \pm\frac{\sqrt{(t \pm 2t')^2 + \upsilon^2}}{t^2 \pm 2tt' + \upsilon^2 + t\sqrt{(t \pm 2t')^2 + \upsilon^2}}, \tag{5.21}$$

with δk_x and δk_y denoting the momentum relative to the van Hove saddle point value.

At van Hove filling, the density of states becomes logarithmic $\rho(\omega) \approx 2\nu_0^{\pm} \ln(W/\omega)$ with W an ultraviolet energy cutoff of the order of the bandwidth and ω the energy relative to the van Hove singularity playing the role of an infrared cutoff. The density of states constant ν_0 is defined $\nu_0^{\pm} = \sqrt{m_x^{\pm} m_y^{\pm}}/4\pi^2$ for filling $\mu_{\pm}$. The particle-particle and particle-hole susceptibilities with logarithmic and double logarithmic divergence are required to determine the possible Fermi surface instabilities. The susceptibilities

are [Yao2015]

$$\Pi_0^{\mathrm{pp}}(\omega) \approx \nu_0^{\pm} \ln^2\left(\frac{W}{\omega}\right), \qquad \Pi_0^{\mathrm{ph}}(\omega) \approx 2\nu_0^{\pm} \ln\left(\frac{W}{\omega}\right),$$
$$\Pi_{\mathbf{q}_1}^{\mathrm{ph}}(\omega \approx 2\gamma\nu_0^{\pm} \ln\left(\frac{W}{\omega}\right), \qquad \Pi_{\mathbf{q}_2}^{\mathrm{ph}}(\omega) \approx 2\beta^{\pm}\nu_0^{\pm} \ln\left(\frac{W}{\omega}\right),$$
$$\Pi_{\mathbf{q}_2}^{\mathrm{pp}}(\omega) \approx 2\alpha^{\pm}\nu_0^{\pm} \ln\left(\frac{W}{\omega}\right); \tag{5.22}$$

$$\alpha^{\pm} = \frac{1+\kappa^{\pm}}{2\sqrt{\kappa^{\pm}}}, \qquad \beta^{\pm} = \frac{2\sqrt{\kappa^{\pm}}}{1+\kappa^{\pm}} \ln\left|\frac{\kappa^{\pm}+1}{\kappa^{\pm}-1}\right|. \tag{5.23}$$

The vectors $\mathbf{q}_1 = 2\mathbf{K}_1$ and $\mathbf{q}_2 = \mathbf{K}_3 - \mathbf{K}_1$. The $\pm$ signs of susceptibilities have been suppressed to avoid confusion. The ratio $\kappa^{\pm} = m_y^{\pm}/m_x^{\pm}$ causes the logarithm in $\beta^{\pm}$ to diverge as $\kappa \to 1$. κ can be tuned to control the Fermi surface nesting with $\kappa = 1$ the case of perfect nesting. γ is an additional nesting parameter that has been introduced artificially to suppress or enhance $\mathbf{q}_1$ scattering processes relative to the zero-momentum particle-hole processes [Nandkishore2012].

5.3 Results

The renormalisation group analysis is performed using $y = \ln^2(W/\omega)$ as a flow parameter [Shankar1994, Lehur2009]. The flow equations for the dimensionless couplings $g_i \to \nu_0^{\pm} g_i$ are

$$\begin{aligned}
\dot{g}_1 &= -g_1^2 - 2g_3^2 - 2g_2^2 d_1 + g_1^2 d_\gamma; \\
\dot{g}_2 &= -2g_1 g_2 d_1 + (g_2^2 + g_3^2) d_\beta - g_2^2 d_\alpha; \\
\dot{g}_3 &= -2g_1 g_3 + 4g_2 g_3 d_\beta.
\end{aligned} \tag{5.24}$$

The y-dependence of the g_i has been suppressed and $\dot{g}_i$ is used to denote the derivative dg_i/dy for brevity. The $d_x(y)$ parameters are defined as $d_1(y) = d\Pi_0^{\mathrm{ph}}(y)/d\Pi_0^{\mathrm{pp}}(y)$, $d_\gamma(y) = d\Pi_{\mathbf{q}_1}^{\mathrm{ph}}(y)/d\Pi_0^{\mathrm{pp}}(y)$, $d_\beta(y) = d\Pi_{\mathbf{q}_2}^{\mathrm{ph}}(y)/d\Pi_0^{\mathrm{pp}}(y)$, $d_\alpha(y) = d\Pi_{\mathbf{q}_2}^{\mathrm{pp}}(y)/d\Pi_0^{\mathrm{pp}}(y)$. The

functions $d_x(y)$ with $x \in \{1, \alpha, \beta, \gamma\}$ have the asymptotic forms $d_x(y) \to 1$ as $y \to 0$ and $d_x(y) \to x/\sqrt{y}$ as $y \to \infty$.

The system of differential equations can be solved numerically using an approximate function for $d_x(y)$. The approximate function is defined $d_x(y) = x/\sqrt{x^2 + y}$ and interpolates between the small-y and large-y asymptotic forms [Nandkishore2012, Yao2015]. The couplings g_i are assigned the initial values $g_i(y = 0) = \nu_0^{\pm} U$ at the beginning of the renormalisation group flow.

However a more elucidating solution can be obtained by making the simplification $d \approx d\Pi^{\mathrm{ph}}_{\mathbf{q}_2}(y)/d\Pi^{\mathrm{pp}}_0(y)$, approximating the function as a constant nesting parameter with constraints $0 \leqslant d \leqslant 1$. This accounts for the enhanced divergence of the $\mathbf{q}_2$ particle-hole bubble at perfect nesting. The simplified forms of the equations are

$$\begin{aligned} \dot{g}_1 &= -g_1^2 - 2g_3^2; \\ \dot{g}_2 &= d(g_2^2 + g_3^2); \\ \dot{g}_3 &= -2g_1 g_3 + 4d g_2 g_3. \end{aligned} \tag{5.25}$$

Contributions with single logarithmic divergences have been discarded from the above equations.

For $d = 0$ the differential equations can be solved analytically. At the critical value $y_c = (1+\sqrt{2})/\nu_0 U$ the couplings diverge to strong coupling. When solving the differential equations for $d \neq 0$ this value is set as the maximum possible value of y. If the phase transition does not occur before $y_c = (1 + \sqrt{2})/\nu_0 U$ then no phase transition is said to occur. The solution to the renormalisation group equations for $d = 1$ is shown in Fig. 5.3. g_3 cannot change sign and retains the sign of $g_3(0)$ due to the β-function vanishing as the coupling goes to zero. g_1 decreases under the renormalisation group and will eventually become negative, leading to superconductivity.

It is important to note that the couplings g_i flow to strong coupling as $y \to y_c$, therefore the one-loop renormalisation group performed cannot provide a quantitative estimate of the phase transition and only provides a qualitative picture of the phase

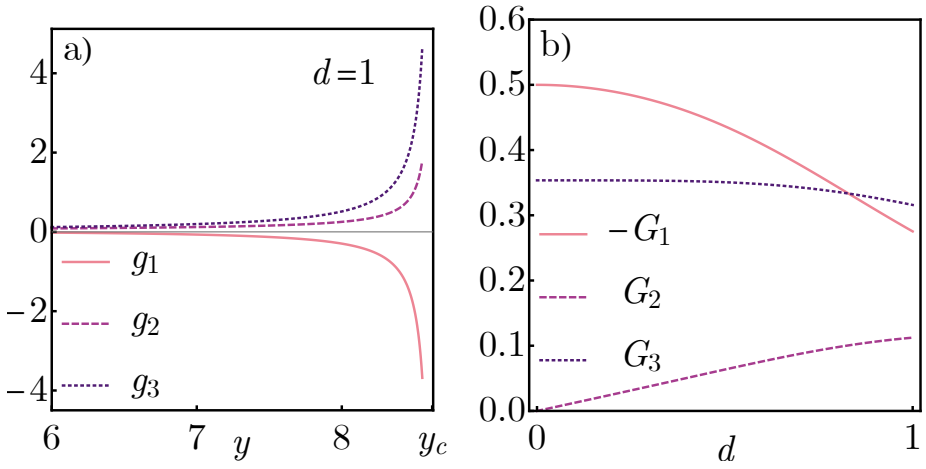

Figure 5.3: a) shows a numerical solution of the flow equations g_i at μ_+ van Hove filling with the nesting parameter $d = 1$. The initial values of the couplings are $g_i(0) = 0.04$. b) shows the exponent values in (5.26) for $0 \leqslant d \leqslant 1$.

diagram.

Due to the divergence of the couplings it is useful to introduce the asymptotic form

$$g_i \approx \frac{G_i}{y_c - y} \tag{5.26}$$

to describe the divergence of the couplings in the vicinity of $y \to y_c$ [Furukawa1998a].

To calculate the possible Fermi surface instabilities, infinitesimal test vertices are introduced in the particle-particle and particle-hole channels that allow for several types of order: superconductivity, $\mathbf{q}_1$ and $\mathbf{q}_2$ density waves, and Fulde-Ferrell-Larkin-Ovchinnikov (FFLO) superconductivity with finite momentum Cooper pairs. The test vertices added to the Lagrangian are

$$\delta\mathcal{L} = \sum_{a=1}^{4}[\Delta_{a\bar{a}}\psi_a^\dagger\psi_{\bar{a}}^\dagger + \phi_{a\bar{a}}\psi_a^\dagger\psi_{\bar{a}}] + \sum_{a=1}^{2}\sum_{b=3}^{4}[\phi_{ab}\psi_a^\dagger\psi_b + \Delta_{ab}\psi_a^\dagger\psi_b^\dagger + (a \leftrightarrow b)] \tag{5.27}$$

Spatially uniform ($\mathbf{q} = 0$) charge and magnetic orderings are suppressed due to the irrelevance of the intra-patch density-density interaction.

Calculating the flow of the vertices in the superconducting channel

$$\frac{d}{dy}\begin{pmatrix}\Delta_{12}\\ \Delta_{21}\\ \Delta_{34}\\ \Delta_{43}\end{pmatrix} = \begin{pmatrix}-g_1 & g_1 & 2ig_3 & -2ig_3\\ g_1 & -g_1 & -2ig_3 & 2ig_3\\ -2ig_3 & 2ig_3 & -g_1 & g_1\\ 2ig_3 & -2ig_3 & g_1 & -g_1\end{pmatrix}\begin{pmatrix}\Delta_{12}\\ \Delta_{21}\\ \Delta_{34}\\ \Delta_{43}\end{pmatrix}. \tag{5.28}$$

The two possible nonzero eigenvalues of the matrix are $\lambda_1 = -2(g_1 - 2g_3)$ and $\lambda_2 = -2(g_1 + 2g_3)$ with corresponding eigenvectors

$$\mathbf{v}_1 = \frac{1}{2}\begin{pmatrix}-i\\ i\\ -1\\ 1\end{pmatrix}, \qquad \mathbf{v}_2 = \frac{1}{2}\begin{pmatrix}i\\ -i\\ -1\\ 1\end{pmatrix}. \tag{5.29}$$

The superconductivity is chiral or anti-chiral depending on the sign of g_3 in the helicity basis. Similar analysis can be performed in the FFLO and the $\mathbf{q}_1$ and $\mathbf{q}_2$ density wave channels to find all the possible ordered phases that are allowed to develop in the model. The order parameters obey $\dot{\Delta}_j = \varepsilon_j \Delta_j$. The susceptibilities for each ordered phase obey the asymptotic form close to the phase transition $\Pi_j(y) \sim (y_c - y)^{\alpha_j}$ [Furukawa1998a].

The exponents for superconductivity and $\mathbf{q}_2$ density wave orders are given by $\alpha_{\mathrm{SC}_1} = 2(G_1 - 2G_3)$, $\alpha_{\mathrm{SC}_2} = 2(G_1 + 2G_3)$, $\alpha^{\mathbf{q}_2}_{\mathrm{DW}\pm} = -d(G_2 \pm 2G_3)$. The FFLO superconductivity and $\mathbf{q}_1$ density wave order are suppressed and the $\mathbf{q}_2$ density wave order is also suppressed away from perfect nesting. The exponents for FFLO and $\mathbf{q}_1$ density wave order are $\alpha_{\mathrm{FFLO}} = 2d_\alpha(y_c)G_2$, $\alpha^{\mathbf{q}_1}_{\mathrm{DW}} = -d_\gamma(y_c)G_1$.

As the interactions g_i flow to strong coupling it is useful to utilise the monotonically increasing interaction g_2 as a flow parameter [Nandkishore2012]. Redefining the couplings $g_1 = x_1 g_2$ and $g_3 = x_3 g_2$ allows for ratios of the divergent couplings to be plotted such that a picture of the fixed points of the problem can be obtained. The flow

equations expressed in terms of the coupling ratios are

$$\begin{aligned}\frac{dx_1}{d\ln g_2} &= -x_1 - \frac{x_1^2 + 2x_3^2}{d(1+x_3^2)},\\ \frac{dx_3}{d\ln g_2} &= -x_3 - \frac{2x_3(x_1-2d)}{d(1+x_3^2)}.\end{aligned} \tag{5.30}$$

The fixed points of these equations describe four trajectories of the renormalisation group flows. For the metallic fixed point g_2 does not flow. The density wave phase exists for $g_3 \to 0$. For the density wave trajectory $g_1 \to 0$ and only g_2 diverges. For the superconducting trajectories all of the couplings are divergent with the exact ratios a function of the nesting parameter. As $d \to 0$, the density wave and metal trajectories merge together and only the metallic phase is left. The flow diagram is plotted in Fig. 5.4a for the nesting parameter $d = 1$.

To understand the final form-factor of the superconducting order parameter, it must be analysed in the original laboratory $\{\uparrow,\downarrow\}$ spin basis. Although the order parameter is discrete I shall describe the superconducting forms in analogy with the continuum angular momentum channels. The even-parity components of the order parameter are the isotropic s-wave channel $\Delta_s = \Delta(1,1,1,1)^{\mathrm{T}}$ and nodal d-wave $\Delta_d = \Delta(1,1,-1,-1)^{\mathrm{T}}$. The four-component vectors give the phase of the superconducting order parameter at each of the four van Hove points, $(\mathbf{K}_1, \mathbf{K}_2, \mathbf{K}_3, \mathbf{K}_4)$. The odd-parity components of the order parameter correspond to chiral p-wave $\Delta_{p_x+ip_y} = \Delta(-i,i,-1,1)$, and anti-chiral p-wave $\Delta_{p_x-ip_y} = \Delta(i,-i,-1,1)$ in the Yao-Yang van Hove scenario. However the odd-parity sector can represent higher order angular momentum channels for the edge van Hove scenario. The continuum order parameter for systems with broken inversion symmetry is written as $\mathbf{\Delta}(\mathbf{k}) = (\Psi_s(\mathbf{k}) + \mathbf{d}(\mathbf{k})\cdot\boldsymbol{\sigma})i\sigma_y$ and allows for a mixing of even- and odd-parity components of the superconducting order parameter. In the Yao-Yang scenario the singlet component of the superconductivity $\Psi_s(\mathbf{k})$ corresponds to an s-wave form for α_{SC_1} and a d-wave form for α_{SC_2}. The triplet component is helical and forms with chiral $p_x + ip_y$ superconductivity for one spin polarisation and anti-chiral $p_x - ip_y$ superconductivity for the other, with $\mathbf{d}(\mathbf{k}) = (\sin k_x, \sin k_y, 0)^{\mathrm{T}}$.

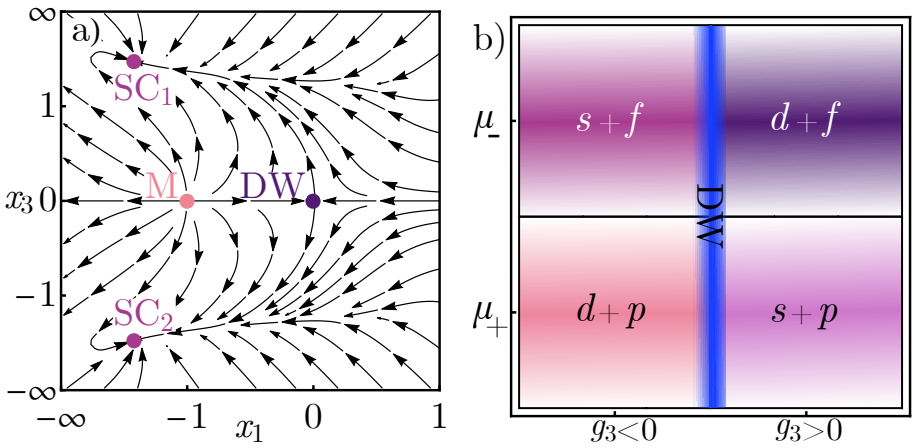

Figure 5.4: Utilising the simplified differential equations (5.25), a) shows the flows of the couplings with the nesting parameter $d = 1$, projected onto the x_1x_3-plane, where $x_1 = g_1/g_2$ and $x_3 = g_3/g_2$ are ratios between couplings. The fixed points in the diagram correspond to flow trajectories in the full space of couplings along which the ratios x_1 and x_3 become fixed. To include all points out to infinity, the axes has been rescaled $x \to x/(1 + |x|)$. M denotes the metallic trajectory, DW the $\mathbf{q}_2$ density wave trajectory, and SC_1 and SC_2 the superconducting trajectories. b) shows a schematic phase diagram near the two van Hove fillings with the chemical potentials μ_- and μ_+ respectively. Negative values of g_3 have been included in the phase diagram. However in the model (5.8) all the interactions are initially repulsive as there is only Colulomb repulsion included in the bare model. For a more complicated microscopic model it is possible for g_3 to be negative. The sign of g_3 determines whether the singlet component of the superconductivity is s-wave or d-wave. Density-wave order dominates when g_3 is close to zero.

In the edge van Hove scenario the form factor cannot in general be described by low order angular momentum harmonics. If the van Hove points lie at $(\pm\pi/2, \pi)$, $(-\pi, \pm\pi/2)$ along the Brillouin zone edge, α_{SC_1} corresponds to a superposition of singlet d-wave superconductivity with form factor

$$\Psi_s(\mathbf{k}) = \cos 2k_x - \cos 2k_y \tag{5.31}$$

and triplet f-wave superconductivity with the form factor

$$\mathbf{d}(\mathbf{k}) = (\cos k_x - \cos k_y)(\sin k_x, \sin k_y, 0)^{\mathrm{T}}. \tag{5.32}$$

The singlet component of α_{SC_2} is s-wave instead of d-wave. For van Hove points lying at different positions along the Brillouin zone edge the form factor requires higher harmonics, up to infinite order as the van Hove points approach the $(0, \pi)$ limit.

There also exists a narrow window of density wave order for $g_3 \to 0$ with the fixed point depicted in Fig. 5.4a. The competition between superconductivity and density-waves has been seen to arise in other spin-orbit split systems theoretically such as oxide interfaces [Scheurer2015]. A schematic phase diagram for the model is shown in Fig. 5.4b.

5.4 Summary and discussion

The above analysis shows that mixed-parity superconductivity arises naturally in systems with symmetry-dependent spin-orbit coupling. The direction of the triplet $\mathbf{d}(\mathbf{k})$ vector is determined by the local spin quantisation axis. The triplet component of the superconducting order parameter forms a helical state. This state can be thought of in analogy to the quantum spin Hall insulator [Qi2009]. The helical superconductivity preserves time-reversal symmetry. The mixed-parity superconducting state is topologically non-trivial, i.e. can display Majorana zero modes at vortex core, if the triplet component is greater than the singlet component [Sato2009, Lu2010]. The case I have presented, with both components are equal, lies on the boundary between the topologically trivial and non-trivial phases. The result suggests that the superconductor could perhaps be tuned to a topological state with a magnetic field or via the enhancement of the non-dominant band, and therefore could be utilised for device applications or for topological quantum computing.

It has been shown using similar methods to those above that topological superconductivity can develop in hexagonal lattice systems [Qin2019]. The complex structure of g_3 on the hexagonal lattice is the reason for this. The analysis additionally performs the calculation for a general Berry phase in the system. The engineering of this Berry phase may provide a fertile ground for the development of topological superconductivity.

Chapter 6

Non-Fermi liquid fixed points and anomalous Landau damping in a quantum critical metal

6.1 Introduction

In this chapter I shall present a functional renormalisation group calculation attempting to describe some of the properties of a quantum critical metal with N_b bosonic flavours in two spatial dimensions.

In the case of Ising-nematic order in two spatial dimensions the field theoretic renormalisation group predicts overdamped $z = 3$ dynamics of the order parameter fluctuations with a fermionic self-energy of the form $\omega^{2/3}$ [Altshuler1994, Nayak1994, Polchinski1994, Lee2008]. However, within the field-theoretic treatment it was discovered that high-loop diagrams contribute to the physics even in the limit of large fermion flavours so that a $1/N_f$ theory cannot be formulated [Lee2009]. Additionally, singular corrections arise in the fermion and boson self-energies putting the $z = 3$, $\omega^{2/3}$ theory into dispute [Metlitski2010a, Holder2015]. Quantum Monte Carlo studies have suggested the theory is governed by $z = 2$ critical dynamics [Schattner2016]. Later quantum Monte

Carlo studies suggest that the $z = 2$ regime is in fact an intermediate regime and the theory crosses over to $z = 3$ dynamics in the infrared [Lederer2017, Berg2019]. $z = 2$ dynamics have also been found in theories with many boson flavours [Fitzpatrick2014].

Wilsonian approaches to fermion-boson quantum criticality have not obtained results close to that of field theoretic renormalisation group methods. Wilsonian effective field theories cannot develop non-local or non-analytic corrections. Therefore how the field theory is renormalised to $z = 3$ boson dynamics, which appears as a non-analytic contribution in the conventional approach, remains unclear. Previous Wilsonian analysis starting with local propagators found the infrared fixed point to be of the Wilson-Fisher type with no change in the $z = 1$ bosonic dynamics and a fermionic self energy of the form $\omega^{3/4}$ [Fitzpatrick2013]. This is in disagreement with the field theoretic approach [Altshuler1994, Nayak1994, Polchinski1994, Lee2008] and quantum Monte Carlo studies [Schattner2016].

The effective field theory I present below describes a Pomeranchuk instability, breaking the rotational symmetry of a circular Fermi-surface. In general the fermion-boson coupling $g(k, q)$ has a momentum dependence set by the angular momentum channel l of the Pomeranchuk or density wave instability. In the scaling scheme utilised the momentum dependent contributions of $g(k, q)$ becomes irrelevant at low energies so the results obtained for the $l = 0$ instability $g(k, q) \approx g$ are applicable for all of the Pomeranchuk instability channels [Fitzpatrick2013]. The functional renormalisation group scheme I present is based on that of Maier and Strack [Maier2016], who performed a similar analysis for a spin-density-wave instability in a strange metal model of the cuprates.

6.2 Model and methods

I consider a circular Fermi surface and retain the entire Fermi surface [Polchinski1992]. This removes any additional constraints on scaling imposed in patch-scheme studies where different components of the momentum scale differently [Lee2009, Metlitski2010a]. A schematic of the Fermi surface and scaling approach is depicted in Fig. 6.1. I linearise

the dispersion close to the Fermi surface: $\xi_{\mathbf{k}} \approx \mathcal{A}_x \ell$ with $\mathbf{k} = \hat{\mathbf{n}}(k_F + \ell)$, where ℓ is a perpendicular displacement in the direction $\hat{\mathbf{n}}$ from the Fermi surface to $\mathbf{k}$. ℓ scales towards the Fermi surface under the RG. The Fermi momentum k_F is fixed and does not scale. Momenta parallel to the Fermi surface are parametrised by angles as is the convention in Fermi liquid theory.

The linearisation procedure is valid for $|\ell| < k_{\mathrm{UV}}$, where k_{UV} is the ultraviolet momentum scale above which the Fermi-liquid effective field theory breaks down [Kopietz1997]. The parameters k_{UV} and k_F can be determined at an intermediate point in the renormalisation group flow from experiment or from the underlying microscopic model. However because of this the low-energy theory is k_{UV}- and k_F-dependent and the infrared fixed-point is dependent on the non-universal quantity $N = k_F/k_{\mathrm{UV}}$. The non-universality arises due to UV/IR mixing in schemes with both bosonic and fermionic degrees of freedom [Fitzpatrick2015a]. The presence of the bosonic degrees of freedom means that factors of k_F can no longer be eliminated by rescaling parameters of the theory as they can in a purely fermionic approach [Shankar1991,Shankar1994]. The choice of a frequency cutoff also affects how this non-universality arises, with the non-universality in the frequency cutoff scheme dependent on the dimensionless ratio N. Momentum-cutoff schemes have also found a dependence of the low-energy parameters on k_F [Mandal2015]. The non-universality also appears in the RG of Shankar [Shankar1994] except with k_{UV} as the flow parameter. This allows for a $1/N$ expansion in the low-energy limit as k_{UV} is lowered. Thus in the Shankar scheme large classes of diagrams are suppressed.

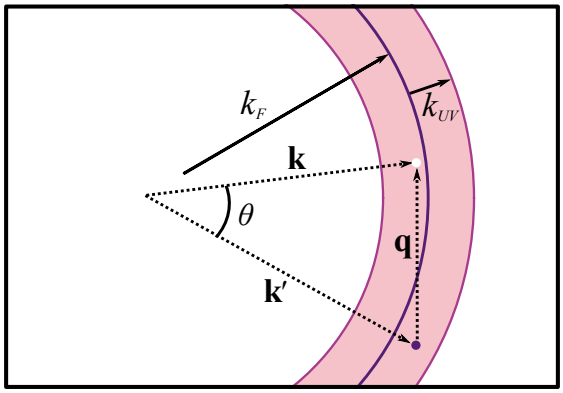

Figure 6.1: Schematic of a section of a circular Fermi surface showing the relevant high-energy scales in the quantum criticality problem: The Fermi momentum k_F, and the ultraviolet momentum cutoff $k_{\rm UV}$ that sets the upper limit of validity of the starting Fermi-liquid theory. The fixed-point results are dependent on these ultraviolet scales via the dimensionless ratio, $N \equiv k_F/k_{\rm UV}$. Additionally the figure shows particle-hole annihilation by a boson with momentum $\mathbf{q} = \mathbf{k} - \mathbf{k}'$.

The effective action for the quantum critical metal is $\Gamma_\Lambda = \Gamma_f + \Gamma_b + \Gamma_g + \Gamma_\lambda$, where

$$\Gamma_f = \sum_{\mu=\uparrow\downarrow} \int_k \overline{\psi}_{k,\mu} \left[i\, \mathcal{A}_\tau\, \omega - \mathcal{A}_x\, \ell \right] \psi_{k,\mu}, \tag{6.1}$$

$$\Gamma_b = \frac{1}{2} \sum_a \int_q \phi^a_q \left[\mathcal{B}_\tau\, \Omega^2 + \mathcal{B}_x\, q^2 + \tilde{\delta} \right] \phi^a_{-q}, \tag{6.2}$$

$$\Gamma_g = \sum_{a,\mu} \int_{k,q} \tilde{g}(k,q) \phi^a_q \overline{\psi}_{k+q,\mu} \psi_{k,\mu}, \tag{6.3}$$

$$\Gamma_\lambda = \tilde{\lambda} \sum_{a,b} \int_{q_1,q_2,q_3} \phi^a_{q_1+q_3} \phi^a_{q_2-q_3} \phi^b_{q_1} \phi^b_{q_2}. \tag{6.4}$$

The effective average action Γ is parametrised by seven renormalisation constants which depend on the running scale Λ. The four fermionic and N_b bosonic fields are coupled by a local Yukawa interaction. The bosonic self-interactions are truncated to quartic order. The mass term $\tilde{\delta}$ and bosonic potential term $\tilde{\lambda}$ are often set to zero at at the beginning of the flow in theories of quantum criticality; however, they are required in a Wilsonian approach.

Considering the renormalisation constants, the parameters $\mathcal{A}_\tau$ and $\mathcal{A}_x$ independently

renormalise the frequency and momentum dependence of the fermion propagator. The parameters can also be thought of in a more common Fermi liquid form with quasiparticle weight $Z = 1/\mathcal{A}_\tau$ and Fermi velocity $v = \mathcal{A}_x/\mathcal{A}_\tau$.

The bosonic propagator is parametrised by three renormalisation constants $\mathcal{B}_\tau$, $\mathcal{B}_x$ and $\tilde{\delta}$. The order parameter of the theory is an N_b-component, $O(N_b)$ symmetric scalar field with bosonic velocity $c^2 = \mathcal{B}_x/\mathcal{B}_\tau$. The order parameter describes collective excitations in the symmetric phase. Initially no fermionic modes have been integrated out, in a Wilsonian scheme or otherwise, so the propagator is fully local and the dynamical exponent is $z = 1$. The propagators correctly describe the physics in the high-energy limit of the theory. The frequency and momentum terms are again renormalised independently. The dimensional mass $\tilde{\delta}$ vanishes as $\Lambda \to 0$ and criticality is approached.

Any additional four-point fermion vertices or higher generated in the flow are neglected. Because of this, pairing instabilities are ignored that may set in close to the critical point. Thus the effective field theory is a minimal model for the electron-boson system that assumes that superconducting fluctuations set in at energies lower than the non-Fermi liquid phase [Torroba2014, Fitzpatrick2015b].

Imposing the momenta and frequency scaling such that they scale in the same way, $[\omega] = [\Omega] = [\ell] = [|\mathbf{q}|] = 1$, the fields and boson mass scaling dimensions in terms of Λ are

$$[\psi_{k,\mu}] = -\frac{3}{2}, \qquad [\phi_q^a] = -\frac{5}{2}, \qquad [\tilde{\delta}] = 2. \tag{6.5}$$

For large momentum transfers parallel to the Fermi surface the Yukawa coupling is irrelevant [Polchinski1992, Fitzpatrick2013]. For small momentum transfers with $\hat{\mathbf{n}} \approx \hat{\mathbf{n}}'$ the full momentum dependence of the Yukawa coupling can be expanded as $\tilde{g}(k,q) = \tilde{g} + \tilde{a}_1\ell + \tilde{a}_2|\mathbf{q}| + \ldots$. All terms retaining a momentum dependence in the expansion can be ignored as they are irrelevant. Only the constant part g is relevant.

$$[\tilde{g}] = \frac{1}{2}, \qquad [\tilde{a}_1] = -\frac{1}{2}, \qquad [\tilde{a}_2] = -\frac{1}{2}. \tag{6.6}$$

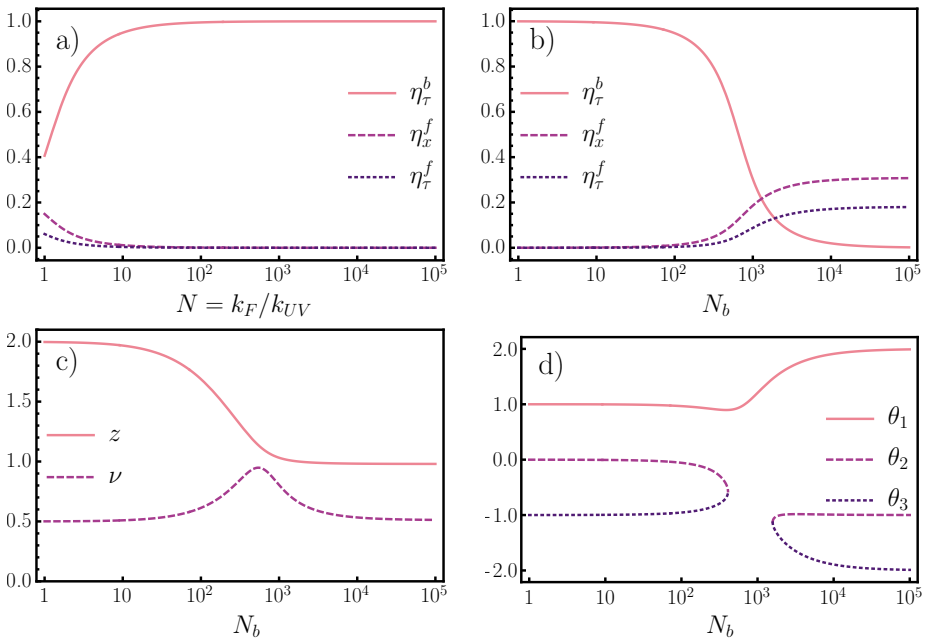

Figure 6.2: a) The anomalous dimensions η_τ^b, η_x^f, and η_τ^f as functions of $N \equiv k_F/k_{\rm UV}$ for the case $N_b = 1$. b) The anomalous dimensions as functions of N_b for $N = 10^3$. This shows the crossover from weak to strong non-Fermi-liquid behaviour at $N_b \sim N$. c) The dynamical exponent z and the critical exponent ν as functions of N_b for $N = 10^3$. The boson dynamics cross over from $z = 2$ to $z = 1$ at $N_b \sim N$. d) The eigenvalues of the stability matrix as functions of N_b for $N = 10^3$.

The scaling dimension of the bosonic quartic interaction is $[\tilde{\lambda}] = 1$.

The renormalisation group method employed is the effective average action formulation of the functional renormalisation group [Wetterich1993] introduced in Chapter 3. This interpretation of Wilsonian renormalisation iteratively integrates over infrared degrees of freedom, including them into the effective average action until the long-wavelength quantum effective action is reached. The governing renormalisation group flow equation, reproduced here from equation (3.32), is a functional differential equation for the effective average action Γ_Λ;

$$\partial_\Lambda \Gamma_\Lambda = \frac{1}{2} \mathrm{STr} \left(\Gamma_\Lambda^{(2)} + R_\Lambda \right)^{-1} \partial_\Lambda R_\Lambda. \tag{6.7}$$

The derivative ∂_Λ is with respect to the running infrared scale Λ. I shall employ this

convention instead of using the flow parameter $y = \log(\Lambda_{\mathrm{UV}}/\Lambda)$ used in the other thesis chapters as the calculation is simpler. The supertrace is defined as $\mathrm{STr}\, A = \mathrm{Tr}\, A_b - \mathrm{Tr}\, A_f$, with A_b and A_f the bosonic and fermionic sectors of the matrix A. The trace Tr denotes a sum over field degrees of freedom and integration over frequencies and momenta. The Hessian $\Gamma_\Lambda^{(2)} = \frac{\overrightarrow{\delta}}{\delta\overline{\chi}}\Gamma_\Lambda\frac{\overleftarrow{\delta}}{\delta\chi}$ is a matrix of functional derivatives with respect to superfields χ and $\overline{\chi}$ composed of the fermionic and bosonic degrees of freedom.

The ansatz for the effective action can be inserted into the expanded flow equation (3.35) presented in Chapter 3 and flow equations can obtained in terms of the system's Green's functions by matching coefficients.

The choice of the regulator function R_Λ is the most important aspect of the analysis I present. In a Wilsonian scheme the low-energy behaviour of the bosonic modes is governed by a single point in momentum space, but the low energy behaviour of the fermionic degrees of freedom is governed by gapless excitations along the entirety of the Fermi surface. For a circular Fermi surface this is a manifold with codimension one. The discrepancies in scaling are thus difficult to address in a momentum-based renormalisation group scheme.

Further, in non-relativistic functional renormalisation group schemes, momentum cutoffs have been found to suppress fermionic soft modes [Honerkamp2001, Husemann2009]. The soft modes are essential for the physics of Landau-damping of order parameter fluctuations. In field theoretic renormalisation group schemes, when calculating diagrams, the integration is performed over momenta and frequencies at all energy scales and thus contributions from soft fermionic modes contribute to the bosonic self energy bubble at all scales. In a Wilsonian scheme, shells of momenta or frequencies are integrated out, beginning with the high energy degrees of freedom. Therefore low energy fermionic modes lie below the renormalisation group scale for the majority of the flow. The question then is how not to artificially suppress soft fermionic modes and further to capture their effects earlier in the flow.

Therefore I employ a frequency cutoff scheme, following Maier and Strack [Maier2016], which better captures soft-mode excitations as they become

singular towards $\mathbf{q} = \mathbf{0}$; momenta are not constrained to a narrow region of states being integrated out of the theory.

The fermion regulator function I employ is

$$R_f = \left[i\,\mathcal{A}_\tau\,\omega - \mathcal{A}_x\,\ell \right] \left[\chi^{-1}(\omega, \Lambda) - 1 \right], \tag{6.8}$$

with

$$\chi(\omega, \Lambda) = \frac{\omega^2}{\omega^2 + \Lambda^2}. \tag{6.9}$$

In this scheme both bosonic and fermionic frequencies scale towards zero. This reduces the complexity of the scheme as scaling to the Fermi surface manifold is avoided. The bosonic regulator function employed is $R_b = \mathcal{B}_\tau\,\Lambda^2$. This is not an optimised form of bosonic regulator but allows for the evaluation of integrals in the chosen scheme.

The fermionic propagator is

$$G_f(\omega, \mathbf{k}) = \frac{\chi(\omega, \Lambda)}{i\,\mathcal{A}_\tau\,\omega - \mathcal{A}_x\,\ell}. \tag{6.10}$$

The fermionic single scale propagator is

$$S_f(\omega, \mathbf{k}) = \partial_\Lambda^{\mathrm{R}}\, G_f(\omega, \mathbf{k}) = \chi'(\omega, \Lambda) \frac{i(2 - \eta_\tau^f)\,\mathcal{A}_\tau\,\omega - (2 - \eta_x^f)\,\mathcal{A}_x\,\ell}{2(i\,\mathcal{A}_\tau\,\omega - \mathcal{A}_x\,\ell)^2}. \tag{6.11}$$

The regulator derivative is defined $\partial_\Lambda^{\mathrm{R}} = \sum_{i=f,b} \partial_\Lambda\, R_i \frac{\partial}{\partial R_i}$. The prime denotes a scale derivative acting only on $\chi(\omega, \Lambda) = \omega^2/(\omega^2 + \Lambda^2)$.

The bosonic propagator is

$$G_b(\Omega, \mathbf{q}) = \frac{-1}{\mathcal{B}_\tau(\Omega^2 + \Lambda^2) + \mathcal{B}_x\,\mathbf{q}^2 + \tilde{\delta}}. \tag{6.12}$$

The bosonic single scale propagator is

$$S_b(\Omega, \mathbf{q}) = \partial_\Lambda^{\mathrm{R}}\, G_b(\Omega, \mathbf{q}) = \frac{\Lambda\,\mathcal{B}_\tau(2 - \eta_\tau^b)}{(\mathcal{B}_\tau(\Omega^2 + \Lambda^2) + \mathcal{B}_x\,\mathbf{q}^2 + \tilde{\delta})^2}. \tag{6.13}$$

For the fermionic momenta: ℓ scales towards the Fermi surface under the renormalisation group, k_F and the angle θ do not scale [Polchinski1992]. The measure employed to compute the fermionic type integrals is [Shankar1994]

$$\int_k = k_F \int_{-\infty}^{\infty} \frac{d\omega}{2\pi} \int_{-\pi}^{\pi} \frac{d\theta}{2\pi} \int_{-k_{\rm UV}}^{k_{\rm UV}} \frac{d\ell}{2\pi} = \frac{k_F \, \mathcal{A}_\tau \, \Lambda^2}{\mathcal{A}_x} \int_{-\infty}^{\infty} \frac{da}{2\pi} \int_{-\pi}^{\pi} \frac{d\theta}{2\pi} \int_{-Y}^{Y} \frac{db}{2\pi}. \tag{6.14}$$

The frequency and momenta have been rescaled $a = \omega/\Lambda$, $b = \mathcal{A}_x \, \ell / \, \mathcal{A}_\tau \, \Lambda$. Y is defined $Y = \mathcal{A}_x \, k_{\rm UV} / \, \mathcal{A}_\tau \, \Lambda$.

For integrals over purely bosonic frequencies and momenta, the isotropic Fermi surface does not set a direction for the boson. Therefore both q_x and q_y must scale under the renormalisation group flow. The measure for bosonic integrals is

$$\int_q = \int_{-\infty}^{\infty} \frac{d\Omega}{2\pi} \int_{-\infty}^{\infty} \frac{dq_x}{2\pi} \int_{-\infty}^{\infty} \frac{dq_y}{2\pi} = \frac{{\mathcal{A}_\tau}^2 \, \Lambda^3}{{\mathcal{A}_x}^2} \int_{-\infty}^{\infty} \frac{da}{2\pi} \int_{-\infty}^{\infty} \frac{db_x}{2\pi} \int_{-\infty}^{\infty} \frac{db_y}{2\pi}. \tag{6.15}$$

The frequency and momenta are rescaled as $a = \Omega/\Lambda$, $b_x = \mathcal{A}_x \, q_x / \, \mathcal{A}_\tau \, \Lambda$, $b_y = \mathcal{A}_x \, q_y / \, \mathcal{A}_\tau \, \Lambda$. Formally the bosonic momenta are constrained such that the absolute momentum of the boson is constrained to $2k_F$ to remain in the particle-hole continuum. However, the rescaled integral limits become $-\infty$ to ∞ only in the infrared limit of interest as $Y \to \infty$.

6.3 Renormalisation group flow equations

The flow equations for the bosonic self-energy, mass, and interactions arise from diagrams with purely bosonic and fermionic lines. The flow of the boson self energy from which the flows of $\mathcal{B}_\tau$, $\mathcal{B}_x$, and $\tilde{\delta}$ can be generated is given by

$$\partial_\Lambda \, \Sigma_b(\Omega, \mathbf{q}) = -4(2 + N_b) \tilde{\lambda} \, \partial_\Lambda^{\rm R} \int_q G_b(\Omega, \mathbf{q}) + 2\tilde{g}^2 \, \partial_\Lambda^{\rm R} \int_k G_f(\omega + \Omega, \mathbf{k} + \mathbf{q}) G_f(\omega, \mathbf{k}) \tag{6.16}$$

with the flow of the boson mass

$$\partial_\Lambda \, \tilde{\delta} = \partial_\Lambda \, \Sigma_b(0, 0). \tag{6.17}$$

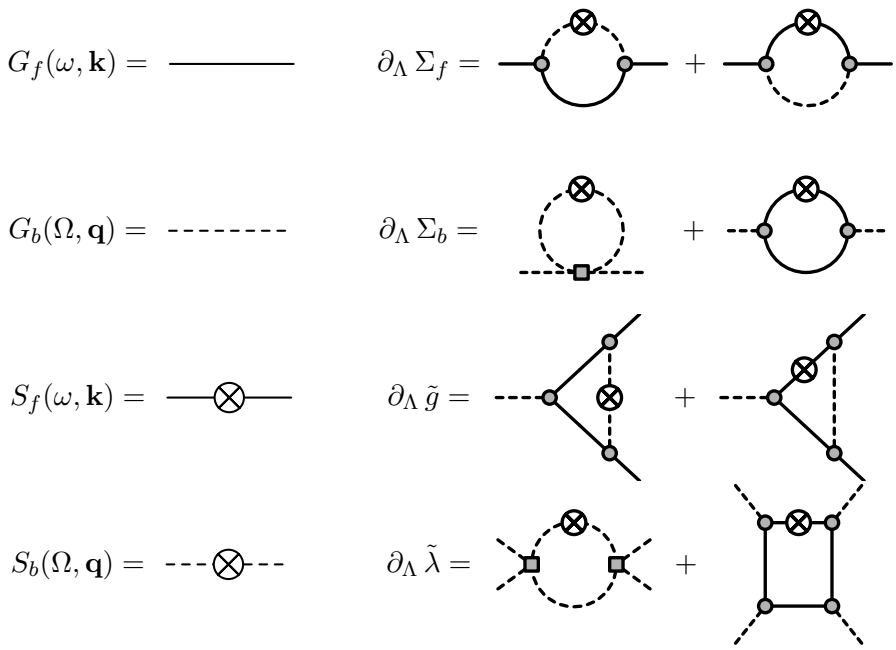

Figure 6.3: Diagrams that contribute to the functional renormalisation group flow equations for the problem of the quantum critical metal. Left: Diagrammatic depiction of the Green's functions and single scale propagators for problem. The scale derivative of the Green's function is denoted with a crossed circle. Right: Diagrammatic contributions to the seven renormalisation parameters in the effective action ansatz of the model. Square vertices denote the bosonic self interaction vertex. The circular vertices denote the Yukawa interaction between fermions and bosons.

$$\partial_\Lambda \tilde{\delta} = -4(2 + N_b)\tilde{\lambda}\, \partial_\Lambda^{\mathrm{R}} \int_q G_b(\Omega, \mathbf{q}) + 2\tilde{g}^2\, \partial_\Lambda^{\mathrm{R}} \int_k G_f^2(\omega, \mathbf{k}). \tag{6.18}$$

The flow of the boson self interaction is given by

$$\partial_\Lambda \tilde{\lambda} = -4(8 + N_b)\tilde{\lambda}^2\, \partial_\Lambda^{\mathrm{R}} \int_q G_b^2(\Omega, \mathbf{q}) + \frac{\tilde{g}^4}{2}\, \partial_\Lambda^{\mathrm{R}} \int_k G_f^4(\omega, \mathbf{k}). \tag{6.19}$$

The fermion self energy and Yukawa vertex are given by diagrams with mixed internal lines. The flow of the fermion self energy from which the flows of $\mathcal{A}_\tau$ and $\mathcal{A}_x$ can be generated is given by

$$\partial_\Lambda \Sigma_f(\omega, \mathbf{k}) = -N_b \tilde{g}^2\, \partial_\Lambda^{\mathrm{R}} \int_q G_f(\omega + \Omega, \mathbf{k} + \mathbf{q}) G_b(\Omega, \mathbf{q}). \tag{6.20}$$

The flow of the Yukawa vertex is given by

$$\partial_\Lambda \tilde{g} = -N_b \tilde{g}^3 \, \partial_\Lambda^{\mathrm{R}} \int_k G_f^2(\omega, \mathbf{k}) G_b(\omega, \mathbf{k}). \tag{6.21}$$

The flows of the renormalisation factors in the propagators are found by taking frequency and momentum derivatives

$$\partial_\Lambda \mathcal{A}_\tau = -\frac{\partial}{i\partial\omega} \, \partial_\Lambda \, \Sigma_f(\omega, \mathbf{k})\Big|_{\omega,\ell=0} \tag{6.22}$$

$$\partial_\Lambda \mathcal{A}_x = \frac{\partial}{\partial\ell} \, \partial_\Lambda \, \Sigma_f(\omega, \mathbf{k})\Big|_{\omega,\ell=0} \tag{6.23}$$

$$\partial_\Lambda \mathcal{B}_\tau = \frac{1}{2} \frac{\partial^2}{\partial\Omega^2} \, \partial_\Lambda \, \Sigma_b(\Omega, \mathbf{q})\Big|_{\Omega,\mathbf{q}=0} \tag{6.24}$$

$$\partial_\Lambda \mathcal{B}_x = \frac{1}{2} \frac{\partial^2}{\partial|\mathbf{q}|^2} \, \partial_\Lambda \, \Sigma_b(\Omega, \mathbf{q})\Big|_{\Omega,\mathbf{q}=0} \tag{6.25}$$

For diagrams with mixed internal lines the momentum transfers $\mathbf{q}$ and $\mathbf{k} - \mathbf{k}'$ are indistinguishable in the bosonic propagators. The expanded momentum transfer is

$$(\mathbf{k} - \mathbf{k}')^2 = (\ell - \ell')^2 + 2k_F^2(1 - \cos\theta) + [2k_F(\ell + \ell') + 2\ell\ell'](1 - \cos\theta). \tag{6.26}$$

This suppresses the contribution to the flow equations for all values of θ other than $1 - \cos\theta$ of the order $\mathcal{O}(1/k_F^2)$. Therefore the term in square brackets can be discarded as it is of order $\mathcal{O}(1/k_F)$ [Fitzpatrick2013].

To compute the fixed points of the problem the beta functions for the dimensionless parameters

$$\delta = \frac{\tilde{\delta}}{\mathcal{B}_\tau \, \Lambda^2}, \qquad \lambda = \frac{\tilde{\lambda}}{2\pi \, \mathcal{B}_x \mathcal{B}_\tau \, \Lambda}, \qquad g^2 = \frac{N\tilde{g}^2}{8\pi \, \mathcal{A}_x{}^2 \, \mathcal{B}_\tau \, \Lambda}, \tag{6.27}$$

are required. Additional rescalings by constant factors have been included to simplify the final beta function expressions.

The beta functions and anomalous dimensions can be calculated analytically in the

infrared limit and for ratio $c^2/v^2 = \mathcal{B}_x \mathcal{A}_\tau{}^2 \,/\, \mathcal{B}_\tau \mathcal{A}_x{}^2 \to 0$. Taking this limit is consistent with the overdamped boson dynamics seen before in theoretical studies [Altshuler1994, Nayak1994, Polchinski1994, Lee2008, Metlitski2010a]. c^2/v^2 is dependent on the scale Λ with the power $[c^2/v^2] = \eta_\tau^b + 2\,\eta_x^f - \eta_x^b - 2\,\eta_\tau^f$. Figs. 6.2(a) and 6.2(b) show that the vanishing of this ratio in the IR is self-consistent for $1 \leqslant N \leqslant 10^5$ and $1 \leqslant N_b \leqslant 10^5$. Details of how the integrals are performed is presented in the chapter appendices (6.B-6.C).

6.4 Results

The dimensionless beta functions $\Lambda\,\partial_\Lambda\,\lambda_i = \beta_i$, $i \in \{\delta, \lambda, g\}$ are given by

$$\beta_\delta = (-2 + \eta_\tau^b)\delta - (2 + N_b)(2 - \eta_\tau^b)\frac{\lambda}{\sqrt{1+\delta}} + 12g^2, \tag{6.28}$$

$$\beta_\lambda = (-1 + \eta_\tau^b)\lambda + (8 + N_b)(2 - \eta_\tau^b)\frac{\lambda^2}{2(1+\delta)^{3/2}}, \tag{6.29}$$

$$\beta_{g^2} = \left(-1 + \eta_\tau^b + 2\,\eta_x^f - 2\eta_g\right) g^2, \tag{6.30}$$

with

$$\eta_g = -\frac{N_b g^2}{N}\frac{\left(3\sqrt{1+\delta} + 3 - \eta_\tau^b\right)}{\left(\sqrt{1+\delta}+1\right)^3}. \tag{6.31}$$

The boson anomalous dimensions, defined as $\eta_\tau^b = -\Lambda\,\partial_\Lambda \ln \mathcal{B}_\tau$, $\eta_x^b = -\Lambda\,\partial_\Lambda \ln \mathcal{B}_x$, are

$$\eta_\tau^b = g^2, \qquad\qquad \eta_x^b = 0. \tag{6.32}$$

In the fermionic sector, the momentum anomalous dimension $\eta_x^f = -\Lambda\,\partial_\Lambda \ln \mathcal{A}_x$ is

$$\eta_x^f = \frac{N_b g^2}{N}\frac{\left(2\sqrt{1+\delta} + 2 - \eta_\tau^b\right)}{\sqrt{1+\delta}\left(\sqrt{1+\delta}+1\right)^2}. \tag{6.33}$$

The frequency anomalous dimension $\eta_\tau^f = -\Lambda\,\partial_\Lambda \ln \mathcal{A}_\tau$ is

$$\eta_\tau^f = \frac{N_b g^2}{N} \frac{\left(2\left(\sqrt{\delta+1}+1\right)+\left(\sqrt{\delta+1}-1\right)\eta_\tau^b\right)}{\sqrt{\delta+1}\left(\sqrt{\delta+1}+1\right)^3}. \tag{6.34}$$

The LPA' approximation has been implemented and feedback of fermion anomalous dimensions η_x^f and η_τ^f has been ignored within the beta functions and anomalous dimensions (6.28-6.34). This is required to obtain a solution to the anomalous dimensions and allows for the analytic expressions plotted in Fig. 6.2. The fermionic anomalous dimensions remain small even in the large N_b limit so the approximation should only make small quantitative changes to the anomalous dimensions. $\eta_x^b = 0$ for all N and N_b. The anomalous dimensions η_τ^b, η_x^f and η_τ^f are plotted in Fig. 6.2(a) for $N_b = 1$, $1 \leqslant N \leqslant 10^5$ and in Fig. 6.2(b) for $N = 10^3$, $1 \leqslant N_b \leqslant 10^5$.

The critical exponents can be calculated from Eqs. (6.28)-(6.30) using the stability matrix $\mathcal{M}_{ij} \equiv \partial\beta_i/\partial\lambda_j|_{\lambda=\lambda_*}$. The eigenvalues θ_i of $-\mathcal{M}_{ij}$ characterise the scaling laws at the fixed point. Positive eigenvalues correspond to relevant renormalisation group directions. Using a frequency scale as a flow parameter the largest eigenvalue θ_1 gives the exponent $\theta_1 = 1/\nu z$ for the correlation time τ instead of the usual $1/\nu$ expected when using a momentum scale Λ_k as a flow parameter. Because of this the mapping between frequency and momentum stability matrices is non-trivial for $z \neq 1$. The critical exponent γ is calculated for the susceptibility $\chi = 1/\tilde{\delta}$. The critical exponent η is equal to η_x^b.

The quantum critical point in the Wilsonian model presented is different to that found in field theoretic studies, a modification of the Wilson-Fisher fixed point. At the quantum critical point the bosonic self-interaction remains finite. This leads to the fixed point solution for the mass

$$\delta_* = 2\frac{2+N_b-g_*^2(50+7N_b)}{3g_*^2(4+N_b)-4(5+N_b)}. \tag{6.35}$$

For $N_b = 1$ and in the $N \to \infty$ limit at the fixed point, the interactions and anomalous

dimensions approach:

$$\delta_* \to 12, \qquad g_*^2 \to 1, \qquad \eta_\tau^b \to 1, \qquad \eta_x^b = 0, \qquad \eta_x^f \to 0, \qquad \eta_\tau^f \to 0. \tag{6.36}$$

The largest eigenvalue of the stability matrix, corresponding to the scaling of the mass term, approaches $\theta_1 \to 1$ such that $\nu z \to 1$. This leads to the critical exponents

$$z = \frac{2 - \eta_x^b}{2 - \eta_\tau^b} \to 2, \qquad \nu \to \frac{1}{2}, \qquad \gamma \to 1, \qquad \eta = 0. \tag{6.37}$$

The static exponents are mean-field-like, while the dynamical exponent is modified from the form in the ultraviolet.

In the $N/N_b \to 0$ limit the effect of fermionic fluctuations is decreased. In this limit $\eta_\tau^b \to 0$ and the system becomes non-Fermi liquid

$$\eta_x^f \to \frac{1}{17}(3\sqrt{2} + 1), \qquad \eta_\tau^f \to \frac{1}{17}(5\sqrt{2} - 4). \tag{6.38}$$

The bosonic dynamics approach $z \to 1$ and the fixed point values of δ and λ approach those predicted for a Wilson-Fisher fixed point, decoupled from the fermions. The crossover between the two regimes is shown in Fig. 6.2(c).

The eigenvalue θ_2 corresponding to the bosonic interaction term is irrelevant. It becomes exactly marginal in the $N/N_b \to \infty$ limit when the interacting fixed point collides with an unstable multicritical point with $\lambda_* = 0$. As N_b becomes large the eigenvalues approach those of a Wilson-Fisher fixed point, but still altered slightly due to the presence of the fermionic fluctuations. The eigenvalues are plotted as functions of N_b in Fig. 6.2(d), for a fixed value of N.

6.5 Summary and discussion

I have presented a functional renormalisation group calculation for a quantum critical metal close to a Pomeranchuk instability. The results are parametrised by the two param-

eters: N, the ratio between the Fermi liquid ultraviolet scale and the Fermi momentum, and N_b, the number of boson flavours. The resultant infrared fixed point solution is dependent on the non-universal ratio N/N_b.

In the limit $N/N_b \to \infty$, the system has $z = 2$ boson dynamics and the electrons retain Fermi-liquid-like behaviour. As N/N_b is reduced, the dynamical exponent decreases and the behaviour of the electrons becomes non-Fermi-liquid. For $N/N_b \to 0$, the boson dynamics are not Landau damped with $z = 1$, and the fermion self-energy takes the non-Fermi liquid form $\omega^{1-\eta_\tau^f} \approx \omega^{0.819}$. The anomalous dimension of the functional renormalisation group scheme is smaller than the perturbative results obtained by Fitzpatrick *et al.* [Fitzpatrick2013] due to the increased effect of particle-hole fluctuations in the employed renormalisation group scheme.

The soft frequency regulators capture the feedback of soft particle-hole excitations on the boson. The hard cut-off Wilsonian theory does not capture these effects [Fitzpatrick2013]. The fermions renormalise the bosonic sector more strongly in the functional renormalisation group calculation so that the dynamical exponent departs from $z = 1$ and the non-Fermi liquid effects are weakened. Increasing the number of boson flavours, fermionic fluctuations are suppressed and the theory behaves similarly to the hard cut-off theory.

Although the $z = 2$ dynamics of the boson predicted in this thesis are in agreement with preliminary quantum Monte Carlo studies [Schattner2016], more recent quantum Monte Carlo studies [Lederer2017, Berg2019] that can probe deeper into the infrared have extrapolated behaviour closer to $z = 3$ dynamics in agreement with field theoretic renormalisation group studies [Metlitski2010a, Holder2015]. The enhanced contribution to of the particle-hole fluctuations due to the choice of soft regulator causes a departure from $z = 1$ boson dynamics missed in previous hard cutoff Wilsonian schemes [Fitzpatrick2013] but does not reach the $z = 3$ regime of the field theoretic renormalisation group. Further work is required to investigate whether the $z = 2$ regime is the final regime of the Wilsonian flow or an intermediate regime to $z = 3$ dynamics, as terms of the form $|\omega|/|\mathbf{q}|$ cannot be generated in Wilsonian schemes. These terms are found by

integrating out deep infrared modes in the field theoretic renormalisation group. How similar physics would arise in a Wilsonian scheme is still an open question and may require a further optimised soft regulator scheme if deep infrared modes are being missed, or alterations to the Wilsonian effective theory to emulate the $|\omega|/|\mathbf{q}|$ physics in an analytic way.

6.A Flow equations for renormalisation parameters $\mathcal{B}_\tau$, $\mathcal{B}_{\boldsymbol{x}}$, $\mathcal{A}_\tau$, and $\mathcal{A}_{\boldsymbol{x}}$

The flow of the bosonic frequency is given by

$$\begin{aligned}\partial_\Lambda \mathcal{B}_\tau = &-2(2+N_b)\tilde{\lambda}\,\partial_\Lambda^{\mathrm{R}} \frac{\partial^2}{\partial\Omega'^2}\int_q G_b(\Omega+\Omega',\mathbf{q})\Big|_{\Omega'\to 0} \\ &+ \tilde{g}^2\,\partial_\Lambda^{\mathrm{R}} \frac{\partial^2}{\partial\Omega'^2}\int_k G_f(\omega,\mathbf{k})G_f(\omega-\Omega',\mathbf{k})\Big|_{\Omega'\to 0}.\end{aligned} \tag{6.39}$$

The flow of the bosonic momentum is given by

$$\begin{aligned}\partial_\Lambda \mathcal{B}_x = &-2(2+N_b)\tilde{\lambda}\,\partial_\Lambda^{\mathrm{R}} \frac{\partial^2}{\partial|\mathbf{q}'|^2}\int_q G_b(\Omega,\mathbf{q}+\mathbf{q}')\Big|_{\Omega'\to 0} \\ &+ \tilde{g}^2\,\partial_\Lambda^{\mathrm{R}} \frac{\partial^2}{\partial|\mathbf{q}'|^2}\int_k G_f(\omega,\mathbf{k})G_f(\omega,\mathbf{k}-\mathbf{q}')\Big|_{\mathbf{q}'\to 0}.\end{aligned} \tag{6.40}$$

The flow of the fermion frequency term is given by

$$\partial_\Lambda \mathcal{A}_\tau = N_b\tilde{g}^2\,\partial_\Lambda^{\mathrm{R}} \frac{\partial}{i\partial\omega'}\int_k G_f(\omega,\mathbf{k})G_b(\omega-\omega',\mathbf{k})\Big|_{\omega'\to 0}. \tag{6.41}$$

The flow of the fermion momentum term is given by

$$\partial_\Lambda \mathcal{A}_x = -\,N_b\tilde{g}^2\,\partial_\Lambda^{\mathrm{R}} \frac{\partial}{\partial\ell'}\int_k G_f(\omega,\mathbf{k})G_b(\omega,\mathbf{k}-\mathbf{k}')\Big|_{\mathbf{k}'\to k_F}. \tag{6.42}$$

6.B Flow equations with pure fermionic and bosonic contributions

The bosonic contribution to the flow of the boson mass (6.18) is given by

$$\tilde{\lambda}\,\partial_\Lambda^{\mathrm{R}}\int_q G_b(\Omega,\mathbf{q}) = \tilde{\lambda}\int_{-\infty}^{\infty}\frac{d\Omega}{2\pi}\int_{-\infty}^{\infty}\frac{d^2\mathbf{q}}{(2\pi)^2}\frac{\Lambda\,\mathcal{B}_\tau(2-\eta_\tau^b)}{(\mathcal{B}_\tau(\Omega^2+\Lambda^2)+\mathcal{B}_x\,\mathbf{q}^2+\tilde{\delta})^2}. \tag{6.43}$$

Rescaling to a dimensionless form the integral becomes

$$\tilde{\lambda}\,\partial_\Lambda^{\mathrm{R}}\int_q G_b(\Omega,\mathbf{q}) = 2\frac{\tilde{\lambda}\,{\mathcal{A}_\tau}^2}{\mathcal{B}_\tau\,{\mathcal{A}_x}^2}\int_{-\infty}^{\infty}\frac{da}{2\pi}\int_0^{\infty}\frac{dbb}{2\pi}\frac{(2-\eta_\tau^b)}{(1+a^2+\frac{c^2}{v^2}b^2+\delta)^2}. \tag{6.44}$$

$c^2 = \mathcal{B}_x/\mathcal{B}_\tau$ and $v^2 = {\mathcal{A}_x}^2/{\mathcal{A}_\tau}^2$. Performing the a integration and making the substitution $u = \frac{c^2}{v^2}b^2$

$$\begin{aligned}-4(2+N_b)\tilde{\lambda}\,\partial_\Lambda^{\mathrm{R}}\int_q G_b(\Omega,\mathbf{q}) &= -2(2+N_b)\frac{\tilde{\lambda}}{\mathcal{B}_x}\int_0^{\infty}\frac{du}{2\pi}\frac{(2-\eta_\tau^b)}{(1+u+\delta)^{3/2}}\\ &= -(2+N_b)\frac{\tilde{\lambda}}{2\pi\,\mathcal{B}_x}\frac{(2-\eta_\tau^b)}{\sqrt{1+\delta}}.\end{aligned} \tag{6.45}$$

All other integrals containing only bosonic propagators can be calculated in the same fashion. Therefore higher order bosonic interactions such as sextic or higher order vertices can be included into the calculation using these integrals.

The fermionic contribution to the flow of the boson mass is given by

$$\begin{aligned}2\tilde{g}^2\,\partial_\Lambda^{\mathrm{R}}\int_k G_f^2(\omega,\mathbf{k}) =& 4\tilde{g}^2 k_F\int_{-\infty}^{\infty}\frac{d\omega}{2\pi}\int_{-\pi}^{\pi}\frac{d\theta}{2\pi}\int_{-k_{\mathrm{UV}}}^{k_{\mathrm{UV}}}\frac{d\ell}{2\pi}\times\\ &\times\chi'(\omega,\Lambda)\chi(\omega,\Lambda)\frac{i(2-\eta_\tau^f)\,\mathcal{A}_\tau\,\omega-(2-\eta_x^f)\,\mathcal{A}_x\,\ell}{2(i\,\mathcal{A}_\tau\,\omega-\mathcal{A}_x\,\ell)^3}.\end{aligned} \tag{6.46}$$

Performing the integral over θ and rescaling to a dimensionless form the integral becomes

$$2\tilde{g}^2\,\partial_\Lambda^{\mathrm{R}}\int_k G_f^2(\omega,\mathbf{k}) = \frac{4\tilde{g}^2 k_F}{\mathcal{A}_x\,\mathcal{A}_\tau\,\Lambda}\int_{-\infty}^{\infty}\frac{da}{2\pi}\int_{-Y}^{Y}\frac{db}{2\pi}\frac{-2a^4}{(a^2+1)^3}\frac{i(2-\eta_\tau^f)a-(2-\eta_x^f)b}{2(ia-b)^3}. \tag{6.47}$$

Now performing the integrals over a and b the result is

$$2\tilde{g}^2\,\partial_\Lambda^{\mathrm{R}}\int_k G_f^2(\omega,\mathbf{k}) = \frac{\tilde{g}^2 k_F}{4\pi\,\mathcal{A}_x\,\mathcal{A}_\tau\,\Lambda}\left(\frac{(2-\eta_\tau^f)Y(1+4Y)}{(1+Y)^4}+\frac{3(2-\eta_x^f)Y^3}{(1+Y)^4}\right). \tag{6.48}$$

Naively the integral above vanishes in the infrared limit $Y\to\infty$. However considering the dimensionless parameter $N = k_F/k_{\mathrm{UV}}$ an additional factor of Y is required to obtain the correct power of Λ:

$$\begin{aligned}2\tilde{g}^2\,\partial_\Lambda^{\mathrm{R}}\int_k G_f^2(\omega,\mathbf{k}) &= \frac{\tilde{g}^2 N}{4\pi\,{\mathcal{A}_x}^2}\left(\frac{(2-\eta_\tau^f)Y^2(1+4Y)}{(1+Y)^4}+\frac{3(2-\eta_x^f)Y^4}{(1+Y)^4}\right)\\ &\overset{Y\to\infty}{=} \frac{3\tilde{g}^2 N}{4\pi\,{\mathcal{A}_x}^2}(2-\eta_x^f).\end{aligned} \tag{6.49}$$

The flow of the dimensional mass (6.18) is then

$$\partial_\Lambda\,\tilde{\delta} = -(2+N_b)\frac{\tilde{\lambda}}{2\pi\,\mathcal{B}_x}\frac{(2-\eta_\tau^b)}{\sqrt{1+\delta}}+\frac{3\tilde{g}^2 N}{4\pi\,{\mathcal{A}_x}^2}(2-\eta_x^f) \tag{6.50}$$

Rescaling the parameters to the dimensionless forms (6.27), and neglecting η_x^f on the right-hand side, gives the mass beta function (6.28).

Considering the flow of the bosonic self interaction (6.19) the fermionic contribution is of order $\mathcal{O}(Y^{-2})$ and vanishes in the infrared. Calculating the bosonic contribution the dimensional flow equation is

$$\partial_\Lambda\,\tilde{\lambda} = (8+N_b)\frac{\tilde{\lambda}^2}{4\pi\,\mathcal{B}_x\,\mathcal{B}_\tau\,\Lambda^2}\frac{(2-\eta_\tau^b)}{(1+\delta)^{3/2}} \tag{6.51}$$

leading to the dimensionless beta function (6.29).

Considering the fermionic contributions to flow equations (6.39) and (6.40), the contribution to (6.40) vanishes due to the momentum derivatives that cause the integral to be of order $\mathcal{O}(Y^{-2})$. Additionally, the bosonic contributions to the flow equations (6.39) and (6.40) both vanish. This leads to the anomalous dimension $\eta_x^b = 0$ throughout the flow. The surviving fermionic contribution of $\mathcal{O}(Y^0)$ to (6.39) leads to the anomalous

dimension $\eta_\tau^b = g^2(1-\eta_x^f/2)$ in the $Y\to\infty$ limit.

6.C Flow equations with mixed bosonic and fermionic lines

Considering the flow of the Yukawa vertex where ℓ' has been set to zero in (6.26):

$$\begin{aligned}\partial_\Lambda\,\tilde{g} = -N_b\tilde{g}^3 k_F \int_{-\infty}^{\infty}\frac{d\omega}{2\pi}\int_{-\pi}^{\pi}\frac{d\theta}{2\pi}\int_{-k_{\rm UV}}^{k_{\rm UV}}\frac{d\ell}{2\pi}\times\\ \times\left[\frac{\chi^2(\omega,\Lambda)}{(i\,\mathcal{A}_\tau\,\omega-\mathcal{A}_x\,\ell)^2}\frac{\Lambda\,\mathcal{B}_\tau(2-\eta_\tau^b)}{(\mathcal{B}_\tau(\Omega^2+\Lambda^2)+\mathcal{B}_x(\ell^2+2k_F^2(1-\cos\theta))+\tilde{\delta})^2}\right.\\ \left.-\frac{\chi'(\omega,\Lambda)\chi(\omega,\Lambda)}{(i\,\mathcal{A}_\tau\,\omega-\mathcal{A}_x\,\ell)^2}\frac{(2-\eta_\tau^f)}{(\mathcal{B}_\tau(\Omega^2+\Lambda^2)+\mathcal{B}_x(\ell^2+2k_F^2(1-\cos\theta))+\tilde{\delta})}\right]\end{aligned}\tag{6.52}$$

and rescaling ω and ℓ the flow equation becomes

$$\begin{aligned}\partial_\Lambda\,\tilde{g} = -\frac{N_b\tilde{g}^3 NY}{{\mathcal{A}_x}^2\,\mathcal{B}_\tau\,\Lambda^2}\int_{-\infty}^{\infty}\frac{da}{2\pi}\int_{-\pi}^{\pi}\frac{d\theta}{2\pi}\int_{-Y}^{Y}\frac{db}{2\pi}\times\\ \times\left[\frac{2a^4}{(a^2+1)^3}\frac{1}{(b-ia)^2}\frac{(2-\eta_\tau^f)}{(1+a^2+\frac{c^2}{v^2}(b^2+2N^2Y^2(1-\cos\theta))+\delta)}\right.\\ \left.+\frac{2a^4}{(a^2+1)^2}\frac{1}{(b-ia)^2}\frac{(2-\eta_\tau^b)}{(1+a^2+\frac{c^2}{v^2}(b^2+2N^2Y^2(1-\cos\theta))+\delta)^2}\right].\end{aligned}\tag{6.53}$$

For large N the $1-\cos\theta$ term contributes only when θ is small. Taking the first term in the Taylor expansion for $1-\cos\theta\approx\theta^2/2$ and approximating the angular integral limits $\pm 1/N$ the parallel momenta are constrained such that the scaling of the Yukawa coupling keeps the constant relevant term. Rescaling $b'=\theta NY$ the integral becomes

$$\begin{aligned}\partial_\Lambda\,\tilde{g} = -\frac{N_b\tilde{g}^3}{{\mathcal{A}_x}^2\,\mathcal{B}_\tau\,\Lambda^2}\int_{-\infty}^{\infty}\frac{da}{2\pi}\int_{-Y}^{Y}\frac{db'}{2\pi}\int_{-Y}^{Y}\frac{db}{2\pi}\times\\ \times\left[\frac{2a^4}{(a^2+1)^3}\frac{1}{(b-ia)^2}\frac{(2-\eta_\tau^f)}{(1+a^2+\frac{c^2}{v^2}(b^2+b'^2)+\delta)}\right.\\ \left.+\frac{2a^4}{(a^2+1)^2}\frac{1}{(b-ia)^2}\frac{(2-\eta_\tau^b)}{(1+a^2+\frac{c^2}{v^2}(b^2+b'^2)+\delta)^2}\right].\end{aligned}\tag{6.54}$$

The limit $Y \to \infty$ can then be taken prior to performing the integrals. In the infrared this integral is indistinguishable from an integral over bosonic momenta $\mathbf{q}$ with the measure (6.15).

To compute the above integral it is simpler to consider the general integral

$$\int_{-\infty}^{\infty} \frac{da}{2\pi} \int_{-\infty}^{\infty} \frac{db'}{2\pi} \int_{-\infty}^{\infty} \frac{db}{2\pi} \frac{a^2}{(\beta a^2+\gamma)} \frac{1}{(b-ia)^2} \frac{1}{(1+a^2+z^2(b^2+b'^2)+\delta)} \tag{6.55}$$

with $z^2 = c^2/v^2$. Computing the b' and b integrals

$$\int_{-\infty}^{\infty} \frac{da}{2\pi} \frac{a^2}{(\beta a^2+\gamma)} \left(\frac{z|a|}{4(1+(1-z^2)a^2+\delta)^{3/2}} - \frac{1}{2\pi(1+(1-z^2)a^2+\delta)} \right)$$
$$- \int_{-\infty}^{\infty} \frac{da}{2\pi} \frac{a^2}{(\beta a^2+\gamma)} \frac{za \arctan\left(\frac{za}{\sqrt{1+(1-z^2)a^2+\delta}} \right)}{2\pi(1+(1-z^2)a^2+\delta)^{3/2}}. \tag{6.56}$$

To evaluate the integral containing the arctangent overestimate the integral with the leading order term in the expansion $\arctan(x) \approx x$. For the flow equations (6.21-6.42) the only surviving contribution when taking the necessary β, γ or δ derivatives in the $z \to 0$ limit corresponding to the overdamping of the boson is

$$\int_{-\infty}^{\infty} \frac{da}{2\pi} \frac{a^2}{(\beta a^2+\gamma)} \frac{-1}{2\pi(1+(1-z^2)a^2+\delta)} = -\frac{1}{4\pi} \frac{1}{\beta\sqrt{1-z^2}\sqrt{1+\delta}+\sqrt{\beta\gamma}(1-z^2)}. \tag{6.57}$$

Taking $z \to 0$ and defining the function $F(\beta,\gamma,\delta)$ all the flow equations with mixed internal lines can be computed from

$$F(\beta,\gamma,\delta) = -\frac{1}{4\pi} \frac{1}{\beta\sqrt{1+\delta}+\sqrt{\beta\gamma}}. \tag{6.58}$$

The flow equation (6.21) becomes

$$\partial_\Lambda \tilde{g} = -\frac{N_b \tilde{g}^3}{{\mathcal{A}_x}^2 \mathcal{B}_\tau \Lambda^2} \left[(2-\eta_\tau^f) \frac{\partial}{\partial\beta}\frac{\partial}{\partial\gamma} + (2-\eta_\tau^b) \frac{\partial}{\partial\beta}\frac{\partial}{\partial\delta} \right] F(\beta,\gamma,\delta)\Big|_{\beta,\gamma\to 1}. \tag{6.59}$$

The flow equation (6.42) becomes

$$\partial_\Lambda \mathcal{A}_x = \frac{N_b \tilde{g}^2}{\mathcal{A}_x \mathcal{B}_\tau \Lambda^2} \left[(2+\eta_x^f) \frac{\partial}{\partial \gamma} + (2-\eta_\tau^b) \frac{\partial^2}{\partial \delta^2} \right] F(\beta,\gamma,\delta) \Big|_{\beta,\gamma\to 1}. \tag{6.60}$$

The flow equation (6.41) becomes

$$\partial_\Lambda \mathcal{A}_\tau = \frac{N_b \tilde{g}^2 \mathcal{A}_\tau}{{\mathcal{A}_x}^2 \mathcal{B}_\tau \Lambda^2} \left[2(2-\eta_\tau^f) \frac{\partial}{\partial \beta} \frac{\partial}{\partial \delta} + 2(2-\eta_\tau^b) \frac{\partial}{\partial \gamma} \frac{\partial}{\partial \delta} + (2-\eta_\tau^b) \frac{\partial^2}{\partial \delta^2} \right] F(\beta,\gamma,\delta) \Big|_{\beta,\gamma\to 1}. \tag{6.61}$$

Utilizing the definitions of the anomalous dimensions within the main discussion, rescaling $\tilde{g}$, and neglecting the fermionic anomalous dimensions on the right-hand sides of (6.59–6.61) leads to the anomalous dimensions (6.31), (6.33) and (6.34) respectively.

Chapter 7

Thesis discussion

This thesis has primarily investigated phase transitions of itinerant electron systems in two spatial dimensions. Firstly, I examined the interplay of superconductivity and density waves in the phase diagrams of the monolayer transition metal dichalcogenide vanadium diselenide and close to the Lifshitz transition in a square lattice system with Rashba spin orbit coupling. Secondly, I investigated the feedback of order parameter fluctuations on the Fermi liquid from which they came and the subsequent formation of a non-Fermi liquid state.

In chapter 4, "Charge density wave formation in the transition metal dichalcogenides", I showed that charge density wave formation can occur in vanadium diselenide when the Fermi surface is sufficiently nested, even by a purely electronic mechanism. This is important in addressing whether the density wave transition is due to a structural transition in the material, or the susceptibility for electron ordering is such that the density wave forms and drives the structural transition. The density wave phase only forms in the model when components of the bare interaction become attractive at strong Heisenberg exchange interaction. The attractive role of phonons in electron-electron interactions would only enhance this effect so that the true mechanism is most likely an interplay of phononic and electronic interactions.

In chapter 5, "Mixed-parity superconductivity near Lifshitz transitions in strongly spin-orbit-coupled metals", I investigated the unconventional superconductivity formed

in lattice systems with Rashba spin-orbit coupling close to a van Hove singularity in the band structure. The results showed that the formation of mixed-parity superconductivity arose naturally from particle-particle and particle-hole interactions.

In both chapters 4 and 5 I demonstrated the importance of retaining both particle-hole and particle-particle fluctuations when constructing the phase diagrams of materials, the formation of unconventional superconductivity driven by contributions from the particle-hole channel.

Ideally this would also be possible when considering the feedback of the order parameter on the Fermi liquid and the formation of the non-Fermi liquid phase. The theory I investigated in chapter 6, "Non-Fermi liquid fixed points and anomalous Landau damping in a quantum critical metal", considers the case where superconducting fluctuations set in at an energy scale lower than the non-Fermi liquid is formed and therefore we can tentatively disregard them. This is not ideal, but is a necessary first approximation for the employment of a functional renormalisation group scheme with a soft frequency cutoff to better capture the role of particle-hole fluctuations suppressed in previous Wilsonian schemes. The results I obtained suggested the Landau damping of the Pomeranchuk instability order parameter to a dynamical exponent of $z = 2$ and the formation of a weak non-Fermi liquid for a small number of boson flavours and a $z = 1$ order parameter and a non-Fermi liquid for a large number of boson flavours. Due to the infancy of Wilsonian approaches to quantum criticality it remains to be seen how these results tie in to the wider picture of the theory of the quantum critical metal.

Bibliography

[Abanov2004] A. Abanov and A. Chubukov, Phys. Rev. Lett. **93**, 255702 (2004).

[Altshuler1994] B. L. Altshuler, L. B. Ioffe, and A. J. Millis, Phys. Rev. B **50**, 14048 (1994).

[Altshuler1995] B. L. Altshuler, L. B. Ioffe, and A. J. Millis, Phys. Rev. B **52**, 5563 (1995).

[Anderson1972] P. W. Anderson, Science **177**, 393 (1972).

[Anderson2002] P. W. Anderson, Physica B **318**, 28 (2002).

[Armitage2010] N. P. Armitage, P. Fournier, and R. L. Greene, Rev. Mod. Phys. **82**, 2421 (2010).

[Bardeen1957] J. Bardeen, L. N. Cooper, and J. R. Schrieffer Phys. Rev. **106**, 162 (1957).

[Bauer2004] E. Bauer, G. Hilscher, H. Michor, Ch. Paul, E. W. Scheidt, A. Gribanov, Yu. Seropegin, H. Noël, M. Sigrist, and P. Rogl, Phys. Rev. Lett. **92**, 027003 (2004).

[Bauer2012] E. Bauer and M. Sigrist, *Non-Centrosymmetric Superconductors* (Springer-Verlag Berlin Heidelberg, 2012).

[Bednorz1986] J. G. Bednorz and K. A. Mueller, Z. Phys. B. **64**, 189 (1986).

[Belitz1997] D. Belitz, T. R. Kirkpatrick, and T. Vojta, Phys. Rev. B **55**, 9452 (1997).

[Berg2019] E. Berg, S. Lederer, Y. Schattner, and S. Trebst, Annu. Rev. Condens. Matter Phys. **10**, 63 (2019).

[Berger1995] E. Berger, P. Valášek, and W. von der Linden, Phys. Rev. B **52**, 4806 (1995).

[Bonilla2018] M. Bonilla, S. Kolekar, Y. Ma, H. C. Diaz, V. Kalappattil, R. Das, T. Eggers, H. R. Gutierrez, M.-H. Phan, and M. Batzill, Nat. Nanotech. **13**, 289 (2018).

[Cao2018] Y. Cao, V. Fatemi, S. Fang, K. Watanabe, T. Taniguchi, E. Kaxiras, and P. Jarillo-Herrero, Nature **556**, 43 (2018).

[Chen2015] X. Chen, Y. Yao, H. Yao, F. Yang, and J. Ni, Phys. Rev. B **92**, 174503 (2015).

[Chen2016] C.-W. Chen, J. Choe, and E. Morosan, Rep. Prog. Phys. **79**, 084505 (2016).

[Chen2018] P. Chen, W. W. Pai, Y.-H. Chan, V. Madhavan, M. Y. Chou, S.-K. Mo, A.-V. Fedorov, and T.-C. Chiang, Phys. Rev. Lett. **121**, 196402 (2018).

[Das2015] S. Das, J. A. Robinson, M. Dubey, H. Terrones, and M. Terrones, Annu. Rev. Mater. Res. **45**, 1 (2015).

[Delamotte2012] B. Dellamote, in *Renormalization Group and Effective Field Theory Approaches to Many-Body Systems* pp 49-132 (Springer-Verlag Berlin Heidelberg, 2012).

[DellAnna2006] L. Dell'Anna and W. Metzner, Phys. Rev. B **73**, 045127 (2006).

[Duvjir2018] G. Duvjir, B. K. Choi, I. Jang, S. Ulstrup, S. Kang, T. T. Ly, S. Kim, Y. H. Choi, C. Jozwiak, A. Bostwick, E. Totenberg, J.-G. Park, R. Sankar, K.-S. Kim, J. Kim, and Y. J. Chang, Nano Lett. **18**, 5432 (2018)

[Efremov2019] D. V. Efremov, A. Shtyk, A. W. Rost, C. Chamon, A. P. Mackenzie, and J. J. Betouras, Phys. Rev. Lett. **123**, 207202 (2019).

[Esters2017] M. Esters, R. G. Hennig, and D. C. Johnson, Phys. Rev. B **96**, 235147 (2017).

[Feng2018] J. Feng, D. Biswas, A. Rajan, M. D. Watson, F. Mazzola, O. J. Clark, K. Underwood, I. Marković, M. McLaren, A. Hunter, D. M. Burn, L. B. Duffy, S. Barua, G. Balakrishnan, F. Bertran, P. Le Fèvre, T. K. Kim, G. van der Laan, T. Hesjedal, P. Wahl, and P. D. C. King, Nano Lett. **18**, 4493 (2018).

[Fernandes2014] R. M. Fernandes, A. V. Chubukov, and J. Schmalian, Nat. Phys. **10**, 97 (2014).

[Fitzpatrick2013] A. L. Fitzpatrick, S. Kachru, J. Kaplan, and S. Raghu, Phys. Rev. B **88**, 125116 (2013).

[Fitzpatrick2014] A. L. Fitzpatrick, S. Kachru, J. Kaplan, and S. Raghu, Phys. Rev. B **89**, 165114 (2014).

[Fitzpatrick2015a] A. L. Fitzpatrick, G. Torroba, and H. Wang, Phys. Rev. B **91**, 195135 (2015).

[Fitzpatrick2015b] A. L. Fitzpatrick, S. Kachru, J. Kaplan, S. Raghu, G. Torroba, and H. Wang, Phys. Rev. B **92**, 045118 (2015).

[Fradkin2010] E. Fradkin, S. A. Kivelson, M. J. Lawler, J. P. Eisenstein, and A. P. Mackenzie, Annu. Rev. Condens. Matter Phys. **1**, 153 (2010).

[Fulde1964] P. Fulde and R. A. Ferrell, Phys. Rev. **135**, A550 (1964).

[Fumega2019] A. O. Fumega, M. Gobbi, P. Dreher, W. Wan, C. González-Orellana, M. Peña-Díaz, C. Rogero, J. Herrero-Martín, P. Gargiani, M. Ilin, M. M.

Ugeda, V. Pardo, and S. Blanco-Canosa, J. Phys. Chem. C **123**, 27802 (2019).

[Furukawa1998a] N. Furukawa, T. M. Rice, and M. Salmhofer, Phys. Rev. Lett. **81**, 3195 (1998).

[Furukawa1998b] N. Furukawa and T. M. Rice, J. Phys.: Condens. Matter, **10**, L381 (1998).

[Gegenwart2008] P. Gegenwart, Q. Si, and F. Steglich, Nat. Phys. **4**, 186 (2008).

[Geim2013] A. K. Geim and I. V. Grigorieva, Nature **499**, 419 (2013).

[Gell-Mann1954] M. Gell-Mann and F. Low, Phys. Rev. **95**, 1300 (1954).

[Gies2002] H. Gies and C. Wetterich, Phys. Rev. D **65**, 065001 (2002).

[Ghadimi2019] R. Ghadimi, M. Kargarian, and S. A. Jafari, Phys. Rev. B **99**, 115122 (2019).

[Ghamari2015] S. Ghamari, S.-S. Lee, and C. Kallin, Phys. Rev. B **92**, 085112 (2015).

[Gorkov2001] L. P. Gor'kov and E. I. Rashba, Phys. Rev. Lett. **87**, 037004 (2001).

[Greco2018] A. Greco and A. P. Schnyder, Phys. Rev. Lett. **120**, 177002 (2018).

[Green2018] A. G. Green, G. Conduit, and F. Krüger, Annu. Rev. Condens. Matter Phys. **9**, 59 (2018).

[Gruner1994] G. Gruner, *Density Waves in Solids*, Frontiers In Physics **89**, (1994).

[Hajiyev2013] P. Hajiyev, C. Cong, C. Qiu, and T. Yu, Sci. Rep. **3**, 2593 (2013).

[Halbinger2019] J. Halbinger, D. Pimenov, and M. Punk, Phys. Rev. B **99**, 195102 (2019).

[Hertz1976] J. A. Hertz, Phys. Rev. B **14**, 1165 (1976).

[Holder2015] T. Holder and W. Metzner, Phys. Rev. B **92**, 041112 (2015).

[Honerkamp2001] C. Honerkamp and M. Salmhofer, Phys. Rev. B **64**, 184516 (2001).

[Hosoi2016] S. Hosoi, K. Matsuura, K. Ishida, H. Wang, Y. Mizukami, T.Watashige, S. Kasahara, Y. Matsuda, and T. Shibauchi, Proc. Natl. Acad. Sci. U.S.A. **113**, 8139 (2016).

[Huang2016] J.-Q. Huang, C.-H. Hsu, H. Lin, D.-X. Yao, and W.-F. Tsai, Phys. Rev. B **93**, 155108 (2016).

[Husemann2009] C. Husemann and M. Salmhofer, Phys. Rev. B **79**, 195125 (2009).

[Isobe2019] H. Isobe and L. Fu, Phys. Rev. Research **1**, 033206 (2019).

[Jang2019] I. Jang, G. Duvjir, B. K. Choi, J. Kim, Y. J. Chang, and K.-S. Kim, Phys. Rev. B **99**, 014106 (2019).

[Johannes2008] M. D. Johannes and I. I. Mazin, Phys. Rev. B **77**, 165135 (2008).

[Kamihara2008] Y. Kamihara, T. Watanabe, M. Hirano, and H. Hosono, J. Am. Chem. Soc. **130**, 3296 (2008).

[Kapustin2018] A. Kapustin, T. McKinney, and I. Z. Rothstein, Phys. Rev. B **98**, 035122 (2018).

[Kohn1965] W. Kohn and J. M. Luttinger Phys. Rev. Lett. **15**, 524 (1965).

[Kopietz1997] P. Kopietz, *Bosonization of Interacting Fermions in Arbitrary Dimensions* (Springer-Verlag, Heidelberg, 1997).

[Kuo2016] H.-H. Kuo, J.-H. Chu, S. A. Kivelson, and I. R. Fisher, Science **352**, 958 (2016).

[Larkin1965] A. I. Larkin and Y. N. Ovchinnikov, Sov. Phys. JETP **20**, 762 (1965).

[Landau1937] L. D. Landau, Zh. Eksp. Teor. Fiz. **7**, 19 (1937).

[Landau1957] L. D. Landau, Sov. Phys. JETP **3**, 920 (1957).

[Lederer1987] P. Lederer, G. Montambaux, and D. Poilblanc, J. Phys. (Paris) **48**, 1613 (1987).

[Lederer2017] S. Lederer, Y. Schattner, E. Berg, and S. A. Kivelson, Proc. Natl. Acad. Sci. USA **114**, 4905 (2017).

[Lee2008] S.-S. Lee, Phys. Rev. B **78**, 085129 (2008).

[Lee2009] S.-S. Lee, Phys. Rev. B **80**, 165102 (2009).

[Lehur2009] K. Le Hur and T. M. Rice, Ann. Phys. **324**, 1452 (2009).

[Lifshitz1960] I. M. Lifshitz, Sov. Phys. JETP **11**, 1130 (1960).

[Litim2000] D. F. Litim, Phys. Lett. B **486**, 92 (2000).

[Litim2001] D. F. Litim, Phys. Rev. D **64**, 105007 (2001).

[Lu2010] C.-K. Lu and S. Yip, Phys. Rev. B **82**, 104501 (2010).

[Lu2018] X. Lu and D. Sénéchal, Phys. Rev. B **98**, 245118 (2018).

[Maier2016] S. A. Maier and P. Strack, Phys. Rev. B **93**, 165114 (2016).

[Maiti2013] S. Maiti and A. V. Chubukov, AIP Conf. Proc. **1150**, 3 (2013).

[Mandal2015] I. Mandal and S.-S. Lee, Phys. Rev. B **92**, 035141 (2015).

[Manzeli2017] S. Manzeli, D. Ovchinnikov, D. Pasquier, O. V. Yazyev, and A.Kis, Nat. Rev. Mater. **2**, 17033 (2017).

[Maslov2010] D. L. Maslov and A. V. Chubukov, Phys. Rev. B **81**, 045110 (2010).

[Mcmillan1975] W. L. McMillan, Phys. Rev. B **12**, 1187 (1975).

[Mermin1966] N. D. Mermin and H. Wagner, Phys. Rev. Lett. **17**, 1133 (1966).

[Metlitski2010a] M. A. Metlitski and S. Sachdev, Phys. Rev. B **82**, 075127 (2010).

[Metlitski2010b] M. A. Metlitski and S. Sachdev, Phys. Rev. B **82**, 075128, (2010).

[Metzner2003] W. Metzner, D. Rohe, and S. Andergassen, Phys. Rev. Lett. **91**, 066402 (2003).

[Metzner2012] W. Metzner, M. Salmhofer, C. Honerkamp, V. Meden, and K. Schönhammer, Rev. Mod. Phys. **84**, 299 (2012).

[Millis1993] A. J. Millis, Phys. Rev. B **48**, 7183 (1993).

[Morel1962] P. Morel and P. W. Anderson, Phys. Rev. **125**, 1263 (1962).

[Nandkishore2012] R. Nandkishore, L. S. Levitov, and A. V. Chubukov, Nat. Phys. **8**, 158 (2012).

[Nayak1994] C. Nayak and F. Wilczek, Nucl. Phys. B **417**, 359 (1994).

[Nishiyama2007] M. Nishiyama, Y. Inada, and G.-Q. Zheng, Phys. Rev. Lett. **98**, 047002 (2007).

[Novoselov2004] K. S. Novoselov, A. K. Geim, S. V. Morozov, D. Jiang, Y. Zhang, S. V. Dubonos, I. V. Grigorieva, and A. A. Firsov, Science **306**, 666 (2004).

[Pawlowski2017] J. M. Pawlowski, M. M. Scherer, R. Schmidt, and S. J.Wetzel, Ann. Phys. (Amsterdam) **384**, 165 (2017).

[Polchinski1984] J. Polchinski, Nucl. Phys. B **231**, 269 (1984).

[Polchinski1992] J. Polchinski, arXiv:hep-th/9210046.

[Polchinski1994] J. Polchinski, Nucl. Phys. B **422**, 617 (1994).

[Pomeranchuk1959] I. J. Pomeranchuk, Sov. Phys. JETP **8**, 361 (1959).

[Qi2009] X.-L. Qi, T. L. Hughes, S. Raghu, and S.-C. Zhang, Phys. Rev. Lett. **102**, 187001 (2009).

[Qin2019] W. Qin, L. Li, and Z. Zhang, Nat. Phys. **15**, 796 (2019).

[Rice1975] T. M. Rice and G. K. Scott, Phys. Rev. Lett. **35**, 120 (1975).

[Ridgway2015] S. P. Ridgway and C. A. Hooley, Phys. Rev. Lett. **114**, 226404 (2015).

[Rossnagel2011] K. Rossnagel, J. Phys.: Condens. Matter, **23**, 213001 (2011).

[Rost2011] A. Rost, S. Grigera, J. Bruin, R. Perry, D. Tian, S. Raghu, S. A. Kivelson, and A. Mackenzie, Proc. Natl. Acad. Sci. U.S.A. **108**, 16549 (2011).

[Sachdev2010] S. Sachdev, Physica C **470**, S4 (2010).

[Salmhofer2007] M. Salmhofer, Ann. Phys. (Berlin) **16**, 171 (2007).

[Samokhin2004] K. V. Samokhin, E. S. Zijlstra, and S. K. Bose, Phys. Rev. B **69**, 094514 (2004).

[Das Sarma2015] S. Das Sarma, M. Freedman, and C. Nayak, npj Quantum Inf. **1**, 15001 (2015).

[Sato2009] M. Sato and S. Fujimoto, Phys. Rev. B **79**, 094504 (2009).

[Sato2017] M. Sato and Y. Ando, Rep. Prog. Phys. **80**, 076501 (2017).

[Scalapino1995] D. Scalapino, Physics Reports **250**, 329 (1995).

[Schattner2016] Y. Schattner, S. Lederer, S. A. Kivelson, and E. Berg, Phys. Rev. X **6**, 031028 (2016).

[Scheurer2015] M. S. Scheurer and J. Schmalian, Nat. Commun. **6**, 6005 (2015).

[Schulz1987] H. J. Schulz, Europhys. Lett. **4**, 609 (1987).

[Shankar1991] R. Shankar, Physica A **177**, 530 (1991).

[Shankar1994] R. Shankar, Rev. Mod. Phys. **66**, 129 (1994).

[Shibauchi2013] T. Shibauchi, A. Carrington, and Y. Matsuda, Annu. Rev. Condens. Matter Phys. **5**, 113 (2013).

[Shigeta2013] K. Shigeta, S. Onari, and Y. Tanaka, J. Phys. Soc. Jpn. **82**, 014702 (2013).

[Shtyk2017] A. Shtyk, G. Goldstein, and C. Chamon, Phys. Rev. B **95**, 035137 (2017).

[Sigrist1991] M. Sigrist and K. Ueda, Rev. Mod. Phys. **63**, 239 (1991).

[Sigrist2005] M. Sigrist, AIP Conf. Proc. **789**, 165 (2005).

[Sigrist2009] M. Sigrist, AIP Conf. Proc. **1162**, 55 (2009).

[Smidman2017] M. Smidman, M. B. Salamon, H. Q. Yuan, and D. F. Agterberg, Rep. Prog. Phys. **80**, 036501 (2017).

[Stueckelberg1953] E. C. G. Stueckelberg and A. Petermann, Helv. Phys. Acta **26**, 499 (1953).

[Sugawara2019] K. Sugawara, Y. Nakata, K. Fujii, K. Nakayama, S. Souma, T. Takahashi, and T. Sato, Phys. Rev. B **99**, 241404(R) (2019).

[Sur2015] S. Sur and S.-S. Lee, Phys. Rev. B **91**, 125136 (2015).

[Sur2016] S. Sur and S.-S. Lee, Phys. Rev. B **94**, 195135 (2016).

[Sykora2018] J. Sýkora, T. Holder, and W. Metzner, Phys. Rev. B **97**, 155159 (2018).

[Takasan2017] K. Takasan, A. Daido, N. Kawakami, and Y. Yanase, Phys. Rev. **B** 95, 134508 (2017).

[Thier2011] S. C. Thier and W. Metzner, Phys. Rev. B **84**, 155133 (2011).

[Torroba2014] G. Torroba and H. Wang, Phys. Rev. B **90**, 165144 (2014).

[Tsuei2000] C. C. Tsuei and J. R. Kirtley, Rev. Mod. Phys. **72**, 969 9 (2000).

[Trott2018] M. J. Trott and C. A. Hooley, Phys. Rev. B **98**, 201113(R) (2018).

[Trott2020a] M. J. Trott and C. A. Hooley, Phys. Rev. Research **2**, 013106 (2020).

[Trott2020b] M. J. Trott and C. A. Hooley, arXiv:2004.06665.

[Umemoto2018] Y. Umemoto, K. Sugawara, Y. Nakata, T. Takahashi, and T. Sato, Nano Res. **12**, 165 (2018).

[Valla2006] T. Valla, A. V. Federov, J. Lee, J. C. Davis, and G. D. Gu, Science **314**, 1914 (2006).

[van Loon2018] E. G. C. P. van Loon, M. Rösner, G. Schönhoff, M. I. Katsnelson, and T. O. Wehling, npj Quant. Mater. **3**, 32 (2018).

[Volovik2017] G. E. Volovik, Low Temp. Phys. **43**, 47 (2017).

[Wang2014] L. Wang and O. Vafek, Physica C **497**, 6 (2014).

[Wetterich1993] C. Wetterich, Phys. Lett. B **301**, 90 (1993).

[Whitsitt2014] S. Whitsitt and S. Sachdev, Phys. Rev. B **90**, 104505 (2014).

[Wilson1974] K. G. Wilson and J. B. Kogut, Phys. Rep. **12**, 75 (1974).

[Yang2014] J. Yang, W. Wang, Y. Liu, H. Du, W. Ning, G. Zheng, C. Jin, Y. Han, N. Wang, Z. Yang, M. Tian, and Y. Zhang, Appl. Phys. Lett. **105**, 063109 (2014).

[Yao2015] H. Yao and F. Yang, Phys, Rev. B **92**, 035132 (2015).

[Yokoyama2007] T. Yokoyama, S. Onari, and Y. Tanaka, Phys. Rev. B **75**, 172511 (2007).

[Yoshida2016] T. Yoshida and Y. Yanase, Phys. Rev. B **93**, 054504 (2016).

[Yuan2019] N. F. Q. Yuan, H. Isobe, and L. Fu, Nat Commun. **10**, 5769 (2019).

[Zhang2017] D. Zhang, J. Ha, H. Baek, Y.-H. Chan, F. D. Natterer, A. F.Myers, J. D. Schumacher, W. G. Cullen, A. V. Davydov, Y.Kuk, M. Y. Chou, N. B. Zhitenev, and J. A. Stroscio, Phys. Rev. Mater. **1**, 024005 (2017).